

DETERMINATION OF THE ENERGY SPECTRA
OF CLINICAL X-RAY BEAMS USING
DOSE-DEPTH DATA SETS

By

RAJESH PANTHI

Master of Science (M.Sc.) in Physics
Tribhuvan University
Kathmandu, NEPAL
2009

Master of Science (M.Sc.) in Medical Physics
Oklahoma State University
Stillwater, OK, USA
2017

Submitted to the Faculty of the
Graduate College of the
Oklahoma State University
in partial fulfillment of
the requirements for
the Degree of
DOCTOR OF PHILOSOPHY
May, 2018

DETERMINATION OF THE ENERGY SPECTRA
OF CLINICAL X-RAY BEAMS USING
DOSE-DEPTH DATA SETS

Dissertation Approved:

Dr. Eric R. Benton

Dissertation Adviser

Dr. Jacques H. H. Perk

Dr. Eduardo G. Yukihiro

Dr. Mario F. Borunda

Dr. Daqing Piao

ACKNOWLEDGEMENTS

I would like to express the deepest appreciation to my academic adviser, Associate Professor Dr. Eric Benton of the Department of Physics at Oklahoma State University, for his vigorous guidance and help in the completion of this work. He provided me all the academic resources, an excellent lab environment, financial assistantship, and all the lab equipment and materials that I needed for this project. I am grateful for many skills and knowledge that I gained from his classes and personal discussions with him. I also appreciate him for the endless English corrections throughout the preparation of this document, which taught me a lot and helped improve my writing.

I would like to thank Dr. Art Lucas of the Department of Physics at Oklahoma State University for guiding me with his wonderful experience on the Radiation Physics. Every single conversation with him has always been inspirational and very informative to me. This work would never be possible without the help of Dr. Jacques H. H. Perk, especially with the theoretical portion and the computer code. I have learned many skills from the courses that I took with him and countless personal discussions. I also want to thank Dr. Eduardo G. Yukihiro for your brilliant comments and suggestions. My sincere thank extends to the members of my thesis committee: Dr. Mario Borunda and Dr. Daqing Piao of the Oklahoma State University for generously offering their valuable time and support throughout the preparation and

review of this document. I will forever be thankful to my former research adviser, Dr. Jerimy Polf, for all the skills and experience I gained while working with him.

I would like to thank my colleagues Mr. Jonathan Monson and Mr. Oliver Hanson, for helping me with the experimental work of this project respectively at Saint Francis Heart Hospital and Oklahoma Cancer Specialists and Research Institute (OCSRI), Tulsa, OK. I am very much thankful for my lab-mate, Oliver Causey, for all the informative discussions, warm humor, and a source of support when things would get a bit discouraging. To all my former and current lab-mates: Rafiqul Islam, Nathan Lindy, Robert Honeyman, Joseph Ross, Meysam Tavakoli, Bryan Hayes, Paul Inman, and Aaron Braly, thanks guys for always being there for me.

Finally, I am deeply thankful to my family: parents, siblings, wife, and son for their spiritual support and inspiration throughout my life.

Name: RAJESH PANTHI

Date of Degree: MAY, 2018

Title of Study: DETERMINATION OF THE ENERGY SPECTRA OF CLINICAL
X-RAY BEAMS USING DOSE-DEPTH DATA SETS

Major Field: PHYSICS

Abstract:

A method to determine the energy spectra of clinical x-ray beams based on dose-depth datasets measured in the absorber of known composition and thicknesses was developed, implemented by a computer and tested. An iterative perturbation method, originally proposed by Waggner, was implemented with some modification. The energy spectrum estimated by the iterative perturbation method often contains unrealistic spectral features, i.e. peaks and valleys, the number of which being proportional to the number of energy bins considered in the calculation. A method of smoothing the estimated energy spectra of x-ray beams, by means of polynomials of lowest possible degrees to eliminate the nonphysical features in the spectrum, was developed. The estimated energy spectra of x-ray beams after smoothing with polynomials were found to meet all the physical criteria of spectral shapes of therapeutic x-ray beams. Additionally, the use of polynomial fit was found to yield the energy spectrum of an intense x-ray beam in terms of a single continuous function containing only a few parameters. The energy spectra of therapeutic x-ray beams with nominal energies of 6, 10, and 18 MVp, produced by Elekta's Versa-HD linear accelerator (linac), were estimated. Additionally, the energy spectra of filter-free x-ray beams with nominal energies of 6 MVp and 10 MVp produced by the same linac were also estimated. Two sets of dose-depth data were measured in each x-ray beam, one with aluminum and the other with copper absorbers of varying thicknesses. Measurements were obtained from an experimental setup designed to minimize the secondary x-rays that reach the detector by means of two collimators of appropriate dimensions. The dose-depth datasets measured with aluminum were used to estimate the energy spectra of x-ray beams whereas the datasets measured with copper were used to validate the estimated spectra. The estimated spectra were found to produce dose-depth datasets that matched corresponding measured dose-depth datasets within 0.1 to 2.5%.

TABLE OF CONTENTS

1. Introduction	1
2. Production of x-rays	9
2.1. Characteristic x-rays	10
2.2. Bremsstrahlung x-rays	11
3. Interaction of x-rays with matter	13
3.1. Photoelectric effect	14
3.2. Incoherent or Compton scattering	15
3.3. Pair production	17
3.4. Total absorption cross section (μ)	18
4. Energy spectrum of an x-ray beam	21
4.1. Energy spectrum of bremsstrahlung x-rays	21
4.1.1 Thin target spectrum	21
4.1.2 Thick target spectrum	23
4.2. Determination of the energy spectrum of an x-ray beam	27
4.2.1 Direct measurement of the energy spectrum of x-rays	28
4.2.2 Theoretical calculation of the energy spectrum	28
4.2.3 Method of using dose-depth data	29
4.2.3.1 Inverse Laplace Transform	32
4.2.3.2 Direct inversion of Matrix	36

4.2.3.3	Iterative perturbation method	37
5.	Algorithm for estimating x-ray energy spectra	39
5.1.	Description of algorithm	39
6.	Smoothing x-ray energy spectra	55
6.1.	Implementation of a polynomial fit for smoothing x-ray energy spectrum	60
7.	Description of Equipment and Methods	65
7.1.	Equipment	65
7.1.1	Linear Accelerator	65
7.1.2	Detectors	66
7.1.3	Electrometer	67
7.1.4	Absorber material	68
7.1.4.1	Amount of absorber material for measuring attenuation datasets	70
7.1.5	Collimators	71
7.2.	Experimental setup	74
7.3.	Measurement of dose-depth datasets	77
7.3.1	Aluminum absorbers	77
7.3.2	Copper absorbers	80
7.4.	Validity of the estimated spectrum	81
8.	Results and Discussion	83
8.1.	Energy spectrum of a 6 MVp x-ray beam	83
8.1.1	Validation of the estimated spectrum of 6 MVp x-ray beam . . .	86
8.2.	Energy spectrum of a 10 MVp x-ray beam	88
8.2.1	Validation of the estimated spectrum of 10 MVp x-ray beam . . .	91
8.3.	Energy spectrum of a 6 MVp filter-free x-ray beam	92

8.3.1 Validation of the estimated spectrum of 6 MVp FFF x-ray beam	95
8.4. Energy spectrum of a 10 MVp filter-free x-ray beam	96
8.4.1 Validation of the estimated spectrum of 10 MVp filter-free x-ray beam	99
8.5. Energy spectrum of a 18 MVp x-ray beam	100
8.5.1 Validation of the estimated spectrum of 18 MVp x-ray beam . . .	103
8.6. Sensitivity analysis of the spectrum estimating algorithm	104
8.6.1 Choice of the minimum photon energy	104
9. Conclusion	110

LIST OF TABLES

4.1	Analytical functions $g(x)$, used by various authors to represent measured dose-depth datasets and their inverse Laplace transforms. In the tabulated expressions, A , B , d , a_1 , a_2 , a_3 , b_1 , b_2 , b_3 , ν , A_k , and C_k ($k = 1, 2, \dots, N$) are the constants to be determined by fitting measured dose-depth datasets with $g(x)$; μ_0 is the mass attenuation coefficient on absorber for x-rays with maximum energy in an x-ray beam; E_k denote the energies of characteristic x-rays produced by electron target; and $I_{\nu-1/2}(\frac{(A-B)}{2}(\mu - \mu_0))$ is a modified Bessel function.	35
6.1	Coefficients of polynomials, A_r , $r = 0, 1, \dots, 4$, used to fit the spectra showing in Figure 6.3.	63
7.1	Calculation of the first, second and third value layers for the photons with energies equal to an estimated average energy of three different therapeutic x-ray beams.	71
7.2	Dose-depth dataset measured in 6 MVp beam using aluminum absorbers of various thicknesses.	78
7.3	Dose-depth datasets measured in 6 MVp FFF, 10 MVp, 10 MVp FFF, and 18 MVp x-ray beams with aluminum absorbers of various thicknesses.	79
7.4	Dose-depth datasets measured with copper absorbers in five different beams from Elekta Versa-HD linac using copper absorbers.	80

8.1	Total number of iterations performed before the spectrum stopped improving significantly and total percent difference between the measured dose-depth datasets and the dose-depth datasets calculated with energy spectra having different minimum photon energy.	107
8.2	Coefficients, A_r , of the polynomials $I(E) = \sum_{r=0}^q A_r E^r$ that were used to fit the spectra having different minimum photon energies shown in Figure 8.28, where, q denotes the degree of the polynomial.	107

LIST OF FIGURES

2.1	Schematic diagram that shows an emission of characteristic x-rays. An incident electron strikes with one of the inner shell electrons (1). The atomic electron gets completely ejected out and creates an electronic vacancy in the shell (2). The vacancy created by the removal of an inner-shell electron is fulfilled by a transition of electron from one of the outer shells (3). During the transition of electron, a photon called characteristic x-ray is emitted whose energy is equal to the difference between the higher and lower states.	11
2.2	Schematic diagram that shows an emission of bremsstrahlung x-rays. .	12
3.1	Diagram illustrating the emission of characteristic x-rays as a result of the photoelectric process.	14
3.2	Mass absorption coefficients corresponding to the photoelectric process as a function of photon's energy on tungsten and aluminum.	15
3.3	Diagram illustrating the Compton scattering of an x-ray photon by a free electron.	16
3.4	Mass absorption coefficients corresponding to the Compton scattering process as a function of photon energy.	17
3.5	Mass absorption coefficients corresponding to the pair production in nuclear field as a function of photon's energy on tungsten and aluminum.	18
3.6	Mass attenuation coefficient for various interaction between photons and tungsten. Data is taken from NIST database [44]	19

3.7	Relative importance of three major interactions between the photons and absorbers as a function of photon energy and atomic number of the absorber. [46]	20
4.1	Relative intensity in each photon energy interval produced when a beam of monoenergetic electrons of energy $T = h\nu_{max}$ incident on a thin target. [43]	22
4.2	Relative number of photons in each photon energy interval produced when a beam of monoenergetic electrons of energy $T = h\nu_{max}$ incident on a thin target. This is the distribution of the data in Figure 4.1 converted into a number distribution. [2, 43]	23
4.3	Relative intensity in each photon energy interval produced by different monoenergetic beams of electrons with energies E_1, E_2, E_3, \dots are incident on thin targets. [2]	24
4.4	Relative intensity in each photon energy interval produced by a thick target shown as a superposition of thin target spectra. [2, 43]	25
4.5	Diagram of an ideal shape of a 100 kV x-ray spectrum showing the effects of attenuation through the medium before reaching the detector. [1]	26
5.1	Interpolation of the measured dose-depth dataset using a polynomial of degree 3. The measured dose-depth dataset containing 19 data points has been interpolated to get 50 data points for equally spaced thicknesses of $\Delta x = 0.53$ cm.	41
5.2	Block diagram illustrating the main steps for use in estimating the energy spectrum of an x-ray beam using a measured dose-depth dataset. The calculation inside the box labeled as “Box 1” is shown in Figure 5.5.	42

5.3	A guess spectrum containing 50 energy bins ($S^g(50)$) defined for use in estimating the energy spectrum of a 6 MVp x-ray beam. The minimum and the maximum photon energy are 0.1 MeV and 6 MeV respectively. The peak of the spectrum is at approximately 2.0 MeV.	45
5.4	Illustration of the effect of an iterative perturbation applied to a number, 10, according to equation (5.6).	47
5.5	Block diagram showing the calculation in one iterative cycle shown in Box 1 of the block diagram in Figure 5.2.	48
5.6	6 MVp X-ray energy spectrum obtained at the end of 38 th iteration. A comparison between the measured and calculated dose-depth datasets is shown on the right.	53
5.7	Plot showing the total percent difference between the calculated and the measured dose-depth datasets as a function of the number of iterations performed. In this example, the percent difference was found to stop decreasing beyond 38th iteration.	53
6.1	The energy spectrum (left) of a 6 MVp x-ray beam estimated using the dose-depth dataset measured using aluminum absorbers. On the right is a comparison between the dose-depth dataset calculated using the estimated spectrum and the measured dose-depth dataset.	56
6.2	Energy spectra of a 6 MVp x-ray beam obtained at the end of the first four iterations. The dose-depth dataset calculated using each of the spectra on the left is compared with the measured dose-depth dataset and shown in the right side.	58
6.3	The energy spectrum of a 6 MVp x-ray beam obtained at the end of the first 5, 10, 15, 20, 25, 30, 35, and 37 iterations.	59

6.4	The energy spectrum of a 6 MVp x-ray beam (dashed line), estimated by using the iterative perturbation method, is smoothed by fitting the spectrum with a polynomial of degree 4. The energy spectrum represented by the fitted polynomial (solid line) is compared with the guess spectrum (dotted line). The area under each curve is made to be 1.	62
6.5	A comparison between all the spectra shown in Figure 6.3 after smoothing, by fitting a polynomial of 4 th degree in each spectrum. The guess spectrum used in the calculation is also shown in the graph. Each spectrum is normalized in such a way that the area under the curve is 1.	63
7.1	PTW TN31014 ionization chamber.	66
7.2	Photo of a SuperMAX electrometer.	67
7.3	Total mass attenuation coefficient with coherent scattering as a function of photon's energy for water, carbon, aluminum, copper, and lead. [47]	69
7.4	Two numerical solutions	72
7.5	A schematic diagram showing a setup for use in measuring attenuation datasets in therapeutic x-ray beams.	73
7.6	Schematic diagram showing the position of the beam's axis in the primary collimator's aperture. The axis of the beam has been denoted by a \times sign.	74
7.7	Position of the second ionization chamber on the beam's axis and behind the secondary collimator. The buildup cap was taken off while positioning and was put back throughout the measurements.	75
7.8	Diagram showing the position of the PTW TN-31014 (SN-000958) ionization chamber in front of absorber with respect to the beam's axis. The buildup cap was taken off while positioning and was put back throughout the measurements.	76

7.9	Experimental setup for measuring attenuation data in Versa HD linear accelerator.	76
8.1	Plot of a guess energy-spectrum (left) containing 19 energy bins with photon energy ranging from 0.1 MeV to 6 MeV and a plot of the dose-depth data (right) measured with aluminum in a 6 MVp x-ray beam. .	84
8.2	A plot of an improved energy spectrum (left) obtained by performing 25 iterations on the guess spectrum shown in Figure 8.1. The right in the right side is a comparison between the dose-depth data calculated using the improved spectrum and corresponding the measured dose-depth data with aluminum absorbers.	84
8.3	An estimated energy spectrum of a 6 MVp x-ray beam produced by Elekta's Versa-HD linac. The guess spectrum used in the calculation is shown dotted line.	85
8.4	A comparison of the dose-depth dataset, calculated for aluminum absorbers using the estimated energy spectrum (Figure 8.3) of a 6 MVp x-ray beam, and the measured dose-depth dataset from Table 7.4. . . .	86
8.5	A comparison of the dose-depth dataset, calculated for copper absorbers using the estimated energy spectrum (Figure 8.3) of a 6 MVp x-ray beam, and the measured dose-depth dataset from Table 7.4.	87
8.6	Plot of a guess energy-spectrum (left) containing 19 energy bins with photon energy ranging from 0.1 MeV to 10 MeV and a plot of the dose-depth data (right) measured with aluminum absorbers in a 10 MVp x-ray beam.	88
8.7	A plot of the energy spectrum (left) obtained by improving the guess spectrum shown in Figure 8.1. On the right is a comparison between the measured dose-depth data and the dose-depth data calculated using the improved spectrum.	89

8.8	An estimated energy spectrum of a 10 MVp x-ray beam produced by Elekta Versa-HD linac. The guess spectrum used in the calculation is shown dotted line.	89
8.9	A comparison between the dose-depth dataset, calculated for aluminum absorbers using the estimated energy spectrum (Figure 8.3) of a 10 MVp x-ray beam, and the measured dose-depth dataset.	91
8.10	A comparison between the dose-depth dataset, calculated for copper absorbers using the estimated energy spectrum (Figure 8.3) of a 10 MVp x-ray beam, and the measured dose-depth dataset.	92
8.11	Plot of a guess energy-spectrum (left) containing 19 energy bins with photon energy ranging from 0.01 MeV to 6 MeV and a plot of the dose-depth data (right) measured with aluminum absorbers in a 6 MVp x-ray beam in the absence of flattening filter.	93
8.12	A plot of the energy spectrum (left) obtained by improving the guess spectrum shown in Figure 8.1. On the right is a comparison between the measured dose-depth data and the dose-depth data calculated using the improved spectrum.	94
8.13	An estimated energy spectrum of a 6 MVp FFF x-ray beam produced by Elekta Versa-HD linac. The guess spectrum used in the calculation is shown dotted line.	94
8.14	A comparison between the dose-depth dataset, calculated for aluminum absorbers using the estimated energy spectrum (Figure 8.3) of a 10 MVp x-ray beam, and the measured dose-depth dataset.	95
8.15	A comparison between the dose-depth dataset, calculated for aluminum absorbers using the estimated energy spectrum (Figure 8.3) of a 10 MVp x-ray beam, and the measured dose-depth dataset.	96

8.16	Plot of a guess energy-spectrum (left) containing 19 energy bins with photon energy ranging from 0.01 MeV to 10 MeV and a plot of the dose-depth data (right) measured with aluminum absorbers in a 10 MVp filter free x-ray beam.	97
8.17	A plot of the energy spectrum (left) obtained by improving the guess spectrum shown in Figure 8.1. On the right is a comparison between the measured dose-depth data and the dose-depth data calculated using the improved spectrum.	98
8.18	An estimated energy spectrum of a 10 MVp FFF x-ray beam produced by Elekta Versa-HD linac. The guess spectrum used in the calculation is shown dotted line.	98
8.19	A comparison between the dose-depth dataset, calculated for aluminum absorbers using the estimated energy spectrum (Figure 8.3) of a 10 MVp filter-free x-ray beam, and the measured dose-depth dataset.	99
8.20	A comparison between the dose-depth dataset, calculated for copper absorbers using the estimated energy spectrum (Figure 8.3) of a 10 MVp filter-free x-ray beam, and the measured dose-depth dataset. . . .	100
8.21	Plot of a guess energy-spectrum (left) containing 19 energy bins with photon energy ranging from 0.1 MeV to 18 MeV and a plot of the dose-depth data (right) measured with aluminum absorbers in a 18 MVp x-ray beam.	101
8.22	A plot of the energy spectrum (left) obtained by improving the guess spectrum shown in Figure 8.21. On the right is a comparison between the measured dose-depth data and the dose-depth data calculated using the improved spectrum.	101

8.23	An estimated energy spectrum of a 18 MVp x-ray beam produced by Elekta Versa-HD linac. The guess spectrum used in the calculation is shown dotted line.	102
8.24	A comparison between the dose-depth dataset, calculated for aluminum absorbers using the estimated energy spectrum (Figure 8.3) of a 18 MVp x-ray beam, and the measured dose-depth dataset.	103
8.25	A comparison between the dose-depth dataset, calculated for copper absorbers using the estimated energy spectrum (Figure 8.3) of a 10 MVp filter-free x-ray beam, and the measured dose-depth dataset. . . .	104
8.26	Guess spectra with different values of minimum photon energy (E_{min}). Each guess spectrum was defined by a modified log normal distribution given in equation (5.3).	105
8.27	The total percent difference (d) between calculated and measured dose-depth datasets plotted as a function of the number of iterations performed. Different curves represent the calculation performed by considering different values of the minimum photon energy (E_{min}) in the spectrum.	106
8.28	Energy spectra of a 6 MVp x-ray beam obtained by iteratively improving the corresponding guess spectra shown in Figure 8.26.	108
8.29	Energy spectra of a 6 MVp x-ray beam, estimated by considering different values of the minimum photon energy of the beam.	109

Chapter 1

Introduction

Knowledge of the energy spectrum of an x-ray beam is very important both in medical imaging and radiotherapy using x-rays. The most effective way to determine the energy spectrum of an intense x-ray beam is to estimate it from measured dose-depth datasets. However, the current methods of estimating the x-ray energy spectra from the measured dose-depth datasets are inadequate as the calculated spectra often contain unrealistic peaks and valleys, introduced by discretization of the relation between a dose-depth dataset and x-ray energy spectrum. In this project, an iterative perturbation method was used to estimate the energy spectra of x-ray beams from the measured dose-depth dataset. A polynomial of degree as small as possible was found to smooth the unrealistic energy spectrum of an x-ray beam, obtained by iterative perturbation method or any other existing method so that the estimated energy spectra become more realistic than the spectra obtained from existing methods.

An x-ray beam was known to be heterogeneous in terms of energy from its discovery. The heterogeneity in the energy of an x-ray beam along with the different densities and compositions of tissues in a patient body is the essential feature required to use x-rays to diagnose an injury or illness. All the x-ray photons with different energies get attenuated by different amounts while passing through the patient body so that it is possible to produce a shadow image, enabling us to visualize the internal structures of a patient. [\[1,2\]](#)

There are three main modalities of the medical imaging using x-rays: (i) radiography, (ii) fluoroscopy and (iii) computed tomography (CT). Each of these modalities is based on the same basic principle: when a beam of x-rays passes through a body, a fraction of the x-rays is differentially absorbed or scattered by the internal structures of the body and the remaining portion is transmitted through the body. The result is a pattern of the intensity which is dependent on the thickness and composition of the organs in the body. All the diagnostic x-ray beams have nominal energies somewhere between 25 kVp to about 150 kVp. [3,4]

Besides diagnosis, x-rays are widely used in radiation therapy. Radiation therapy uses high energy ionizing radiation, such as x-rays, gamma rays, electrons, protons, and heavy ions to kill cancer cells and shrink tumors. Radiotherapy is based on the principle that when the tumor is irradiated with an appropriate beam of ionizing radiation with sufficient energy, the radiation either damages the single-strand/double-strand DNA of the tumor cells directly or creates ionized molecules (free radicals) within the cells that can in turn damage the DNA. After damage to the DNA, cancer cells either stop dividing or die. The dead cancer cells are eliminated by the body's natural processes. The goal of radiation therapy is to provide a lethal dose to the tumor while sparing surrounding healthy tissues. Therapeutic x-ray beams are produced by electron linear accelerators (linacs) and have nominal energy ranging from 1 MVp to 25 MVp. [2-4]

Although the heterogeneity of an x-ray beam helps to acquire a variety of diagnostic images of patients, it introduces a problem in the radiotherapy using x-rays. Due to the heterogeneous nature of x-ray beams in terms of energy, the dose delivered to a tumor target by a beam of x-rays cannot be localized. While treating a deep-seated tumor, the low energy photons present in the beam produce a dose buildup in front of the tumor. The distribution of patient dose in various tissues can be optimized

by means of several factors such as the use of multiple beams, beam filtration, beam collimation, the beam's nominal energy, etc. But for this purpose, we must have an accurate knowledge of the energy spectrum of a beam of x-rays. [4]

An x-ray beam penetrates through patient's body while acquiring diagnostic images and performing radiotherapy using x-rays, the interaction of x-rays with tissues has special interest in medical physics. In a very crude way, the term "quality" is frequently used to represent physical quantities that directly affect the penetrating ability of an x-ray beam. The term "quality" represents quantities such as the minimum photon energy, maximum photon energy, mean or effective energy, amount of tissue dose as a function of depth, ratio of higher energy x-rays to lower energy x-rays, etc. Ideally, the "quality" of an x-ray beam can be represented only by the energy spectrum of the x-ray beam.

One way to express the "quality" of the beam is the half value layer (HVL). The HVL is the thickness of a material that is required to reduce the initial intensity of a beam by 50% [4]. With the knowledge of HVL of a beam of a known material such as Aluminum, Copper, etc., one can determine the effective energy. Using the HVL we can also approximate the spectrum in terms of a single peak at the energy corresponding to the mass attenuation coefficient determined by the HVL. Using the second HVL we can add another peak but this method does not provide an actual spectrum [5]. The ratio of the first HVL to the second HVL, called the homogeneity coefficient, has also been used as one way to express the quality of the beam [6, 7]. The tube potential, with which the electrons get accelerated from anode to cathode in an x-ray tube, has also been used as a parameter to describe the quality of an x-ray beam. However, none of these approaches provide much detailed information about an x-ray beam.

The energy spectrum of an x-ray beam not only describes the "quality"

of the beam, but is also useful in various other aspects of medical physics. With the energy spectrum of a beam of x-rays, one can design the radiation treatment plan and do dose calculations more accurately. This helps to improve the hardware and/or software system of radiation therapy to deliver lethal dose to the tumor cells and to reduce the absorbed dose to healthy cells. The x-ray spectrum is also useful for predicting image quality in mammography [8], evaluating detector performance [9, 10], correction of beam hardening artifacts [11] and dual energy computed tomography [12].

However, determining the energy spectrum of an x-ray beam has always been challenging for a number of reasons including the extremely high flux of x-ray photons in such beams, inadequate information about the internal structure of x-ray machines, etc. Historically, there are three main methods of determining the energy spectra of x-ray beams: (1) direct measurement, (2) theoretical calculation, and (3) deconvolution of measured dose-depth datasets.

The direct measurement of the energy spectrum of x-rays is possible by using scintillation spectroscopy technique only when the x-ray flux is very small. An extremely high x-ray flux during each short pulse of radiation output causes signal pile-up and saturation-induced dead times in the detector. Similarly, the thickness of the detector required to measure the energy of high energy photons (up to 20 MeV) needs to be large enough to capture all the ionization induced by an x-ray photon. This makes a detector very costly and requires sophisticated calibration. Some measurements of the energy spectra of x-ray beams using specialized detectors such as High-purity Germanium (HPGe) detector [8] and NaI(Tl) scintillation detector system [13, 14], coupled to pulse pile-up rejector/restorer, have been reported in the literature. Such measurements have to be carried out first by scattering the primary x-ray beam and then collimating a small part of the scattered beam towards a detector surrounded by massive shielding. The measured spectra of scattered x-ray beams need to be corrected

by considering the geometrical set-up where Compton interactions are the dominant contributors to scatter requiring a tedious calculation [15]. The direct measurement of the energy spectrum of an x-ray beam is therefore impractical to carry out on regular basis.

The theoretical calculation of x-ray spectra often using Monte Carlo simulation is a very old and powerful approach. This approach is based on a computer simulation of the direct transport of electrons into an electron target to generate x-rays and then transports the generated x-rays through various filters to determine x-ray energy spectra. Theoretically calculated energy spectra of various diagnostic and therapeutic x-ray beams have been reported using different Monte Carlo codes such as EGSnrc [16, 17], MCNP [18–20], ITS [21]. An accurate Monte Carlo simulation of an energy spectrum of an x-ray beam, requires a detailed information about the geometry of the x-ray machine. Due to their proprietary nature, it is often impossible to get detailed information about the internal components of clinical x-ray machines. Even if the required information for one machine is obtained, it is often very time consuming and difficult to reproduce the calculation involved in Monte Carlo simulation for other machines as each x-ray machine has its unique geometry.

The method of determining the energy spectra of x-ray beams using the measured dose-depth datasets is the most popular among the existing methods for practical reasons. This method, originally proposed by Silberstein [22, 23], mathematically relates a measured dose-depth dataset to the energy spectrum of the x-ray beam, in terms of an integral equation or a system of discrete linear equations. Several works have been reported in the literature, each of which made every effort to solve these equations to determine the energy spectra of x-ray beams as accurately as possible by using different mathematical methods such as (i) inverse Laplace transform [22–33], (ii) direct matrix inversion [34–36], (iii) iterative perturbation methods [12, 37–40], neural

network [41], and analytical modeling [42]. Each of these methods including their pros and cons are discussed in Chapter 4.2. Each of the most popular methods, including their pros and cons, are discussed in Chapter 4.2.3.

The accuracy of the energy spectrum of an x-ray beam determined by using a measured dose-depth dataset highly depends on the dose-depth dataset itself. Any small error, introduced through dose-depth dataset, may result in a different spectral shape. A dose-depth dataset for use in estimating the energy spectrum of an x-ray beam must be measured only with the primary x-ray beam as this method does not include secondary x-rays while formulating the problem. But the secondary x-rays produced by various components inside the gantry of an electron linear accelerator (linac), absorber, and air always contaminate the primary x-ray beam. An appropriate geometry in a treatment room was set up for the measurement of dose-depth datasets. Two special collimators were built and characterized to minimize the secondary x-rays that reach the detector while measuring dose-depth datasets. The composite material, physical dimension, and their optimal positions for measuring dose-depth datasets are presented in Chapter 7.1.5.

In this project, the iterative perturbation method originally proposed by Waggener [37] was used. This method starts with an initial x-ray energy spectrum which is then iteratively improved until the calculated dose-depth dataset based on the increasingly modified spectrum agrees with the measured dose-depth dataset. Additional parameters including minimum and maximum x-ray energy, estimated peak energy, and the mass attenuation coefficients on absorber material are also required in the calculation. However, unlike the Monte Carlo simulations, this method does not require detailed information regarding the internal structure or geometry of the x-ray machine. The measurement of the dose-depth datasets required in the calculation can be carried out in a relatively simple way to a high degree of accuracy. A complete de-

scription of an algorithm based on the iterative perturbation method to estimate the energy spectrum of an x-ray beam using a measured dose-depth dataset is presented in Chapter 5.

An iterative perturbation method is only a brute force method in which an initial “guess” spectrum is mathematically corrected until it can reproduce a dose-depth dataset that matches to the measured dose-depth dataset within a predetermined limit. Since a beam of therapeutic x-rays primarily contains only bremsstrahlung x-rays, the energy spectrum of the beam should always be a continuous function of x-ray energy. However, the energy spectrum of an x-ray beam obtained by an iterative perturbation method almost always contains peaks and valleys the number of which is proportional to the number of energy bins considered in the calculation. Such peaks and valleys cannot be expected based on the geometry of the x-ray machine. Additionally, the shape of the energy spectrum obtained by iterative perturbation method is highly dependent on some other factors such as: (i) the choice of the minimum photon energy and (ii) the shape of an initial guess energy-spectrum. Therefore, the spectral shape of an x-ray beam, estimated from a measured dose-depth dataset based on an iterative method, is not stable.

In this project, a method of smoothing the energy spectra of x-ray beams, obtained from an iterative perturbation method, was proposed. This method uses a polynomial of lowest possible degree to fit an energy spectrum containing unrealistic peaks and valleys. An energy spectrum after smoothing with a polynomial does not increase the difference between the dose-depth dataset, calculated using the spectrum before smoothing, and the measured dose-depth dataset. It rather meets all the physical requirements and represents the x-ray spectrum with infinite resolution in terms of energy by a single continuous function. A representation of an energy spectrum with a polynomial is fairly easy to implement and it resolves the problem of spectral shape

dependency on the number of energy bins. The use of a polynomial fit to an energy spectrum makes the estimated spectrum even closer to the correct energy spectrum than the one obtained by a plain implementation of iterative perturbation method.

Chapter 2

Production of x-rays

X-rays are produced by an interaction of fast moving electrons with a material composed of high atomic number (Z) element(s). Most of the time the incident electrons encounter a number of collisions with target atoms in which the electrons get scattered and ionization is produced. Some of such collisions causes the atomic electrons in the target be knocked out of the atoms. If a knocked-out electron has enough energy, it can produce a track of its own. Such electrons are called delta rays. An incident electron can have several ionizational collisions and in each collision, it transfers a part of its kinetic energy to the atomic electrons of the target which will eventually appear as heat.

There are two types of interaction that an electron can have with matter which leads to the production of x-rays: (i) collision with one of the inner shell electrons and (ii) collision with atomic nuclei of the target atoms. Each of these interactions is explained briefly in the following sections. The interaction that leads to the production of x-rays is very rare in comparison to the ionizational collisions. As an example, at 100 kVp, the electrons lose about 99% of their energy in ionization (or heat) and only 1% of their energy converts into x-rays. At higher energies, the amount of energy lost by ionization is slightly less but still significantly large in comparison to the energy converted into x-rays. [2]

2.1 Characteristic x-rays

If an incident electron makes a direct hit on one of the inner shell electrons and the amount of energy transferred to the orbiting electron is more than its binding energy, the electron is completely ejected out of the atom leaving the atom positively ionized. The ejected electron may cause further ionization if it has enough energy. The vacancy left by the ejected electron in the ionized atom is fulfilled by a transition of an electron from one of the outer shells (such as L, M, and N shells) leading to the emission of an x-ray. However, not all the transitions from any outer shell to the inner shell are allowed by the quantum mechanical selection rules.

When a transition of electron from an outer shell to the inner shell takes place a photon, called characteristic x-ray, is emitted. The energy of a characteristic x-ray photon is equal to the difference between the corresponding energy levels:

$$h\nu = E_f - E_i,$$

where E_f and E_i are respectively the energy of the final and initial energy states of the transiting electron. Figure 2.1 shows a schematic diagram that illustrates the production of characteristic x-rays in four different steps labeled as “1”, “2”, “3” and “4”.

It is also possible that the excess energy during the process of downward transition in an excited or ionized atom is given to one of the outer electrons and this electron is then ejected from the atom. The electron emitted from such process is called Auger electron. The energy of an Auger electron is equal to the energy lost by the incident electron minus the binding energy of the electron that is ejected from the atom. The relative probability of the emission of characteristic x-ray to the emission

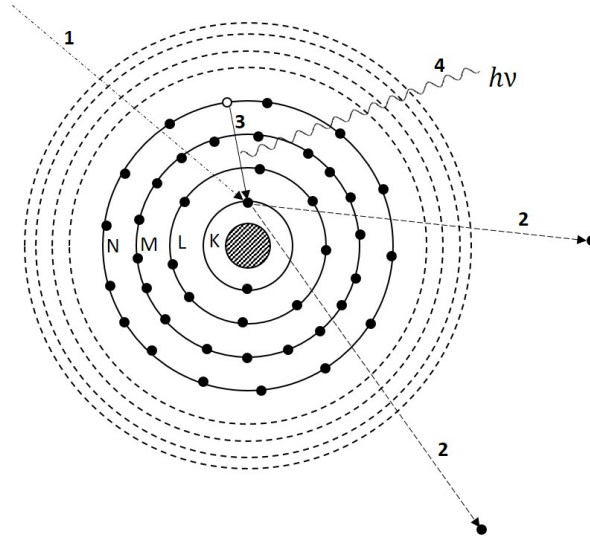


Figure 2.1: Schematic diagram that shows an emission of characteristic x-rays. An incident electron strikes with one of the inner shell electrons (1). The atomic electron gets completely ejected out and creates an electronic vacancy in the shell (2). The vacancy created by the removal of an inner-shell electron is fulfilled by a transition of electron from one of the outer shells (3). During the transition of electron, a photon called characteristic x-ray is emitted whose energy is equal to the difference between the higher and lower states.

of an Auger electron, called the fluorescent yield, increases with the increase of the atomic number of the target elements. [2]

2.2 Bremsstrahlung x-rays

When an electron passes nearby an atomic nucleus of a target, it may be deflected from its original direction by the action of Coulomb force and lose energy in the form of electromagnetic waves called bremsstrahlung x-rays. According to Maxwell's general theory of electromagnetic radiation, energy is propagated through space by electromagnetic fields. As the electron passes in the vicinity of a nucleus, it suffers a sudden deflection because of its associated electromagnetic field and gets deflected. As a result, a part or all of its energy is lost in the form of electromagnetic waves. Figure 2.2 illustrates the production of bremsstrahlung x-rays due to a deceleration of

an electron while passing near a nucleus.

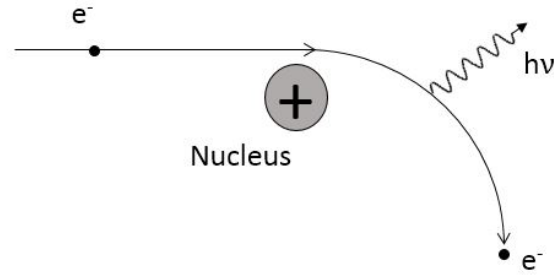


Figure 2.2: Schematic diagram that shows an emission of bremsstrahlung x-rays.

Sometimes, an electron can head straight towards an atomic nucleus of the target and gets completely stopped in a single collision thereby releasing all of its kinetic energy in the form of a single bremsstrahlung photon. This is a very unlikely interaction but occurs with a finite probability and it gives the upper limit of the photon's energy in an x-ray spectrum, i.e. $h\nu_{max} = T$. [\[43\]](#)

Unlike the characteristic x-rays, the energy of the bremsstrahlung x-rays is continuous and depends mainly on the atomic number of the target material and the initial energy of the incident electrons.

Chapter 3

Interaction of x-rays with matter

When a beam of x-rays passes through a material, the x-rays may interact with the material by one of the major three mechanisms: 1) incoherent or Compton scattering, 2) photoelectric effect, and 3) pair production. A less important process called coherent or Rayleigh scattering also takes place, but at only a negligibly small level. The type of interaction that a photon has mainly depends on its energy and the type of material through which it passes. A photon might also go through multiple processes before it is completely absorbed or scattered by the material. Since an x-ray beam is always polyenergetic, photons will undergo all types of interaction while passing through an absorber. [2]

Depending on the type of interaction that an x-ray photon undergoes with the material, the photon may either be scattered with or without losing its energy or may generate charged or uncharged secondary particles. When a photon interacts with the material by any process(es), it is no longer considered a primary photon. And photons generated as a result of an interaction are considered secondary photons. The dose-depth datasets for use in estimating accurately the energy spectrum of an x-ray beam should be measured only with the primary x-rays but the secondary x-rays always contaminate the primary x-ray beam. In the case of an electron accelerator, secondary x-rays are produced by an interaction between the primary x-rays with various components such as the electron target, flattening filter, backing plates, collimating jaws,

absorber, and air. The major three types of interaction that produces the secondary x-rays while measuring attenuation data sets are explained below.

3.1 Photoelectric effect

Figure 3.1 shows a diagram illustrating the production of characteristic x-rays as a result of the photoelectric effect. In this interaction, a photon of energy $h\nu$ collides with an atom and transfers all of its energy to one of the bound electrons on the K, L, M, or N shells, so that the electron is ejected out. A part of the incident photon's energy, equal to the binding energy of the shell from which the electron is ejected (E_s), is used to free the electron from its shell. The ejected electron, called a photoelectron, carries away the remaining energy ($h\nu - E_s$) in the form of its kinetic energy. The photoelectron travels only a relatively short distance and rapidly loses its energy. Therefore the energy of the incident photon is deposited in the matter close to the site of photoelectric interaction. The vacancy created by the ejected electron is filled up by a transition of one of the outer shell electrons thereby releasing a photon, called characteristic x-ray.

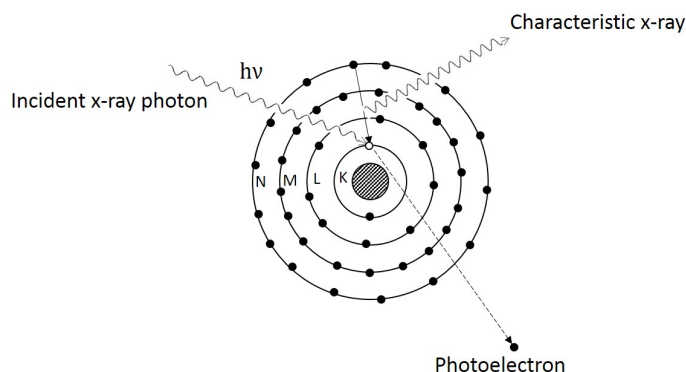


Figure 3.1: Diagram illustrating the emission of characteristic x-rays as a result of the photoelectric process.

The cross-section of the photoelectric process depends on the energy of the

incident photon and the atomic number of the material. Figure 3.2 shows a plot of the mass photoelectric coefficient as a function of photon energy for tungsten ($Z = 74$), representing high Z material, and aluminum ($Z = 13$), representing low Z material. The photoelectric process is most likely to occur if the energy of the incident photon is just greater than the binding energy of the electron. Energies just less than binding energy cannot eject the electron and therefore the cross section varies with energy in a complicated way with discontinuities at the energy corresponding to each shell or sub-shell. For low energy photons ($\lesssim 1$ MeV), the photoelectric cross section between the peaks varies with the photon energy approximately as $1/(\hbar\nu)^3$. The photoelectric cross section per atom depends upon approximately Z^4 for high Z materials and on $Z^{4.8}$ for low Z materials.

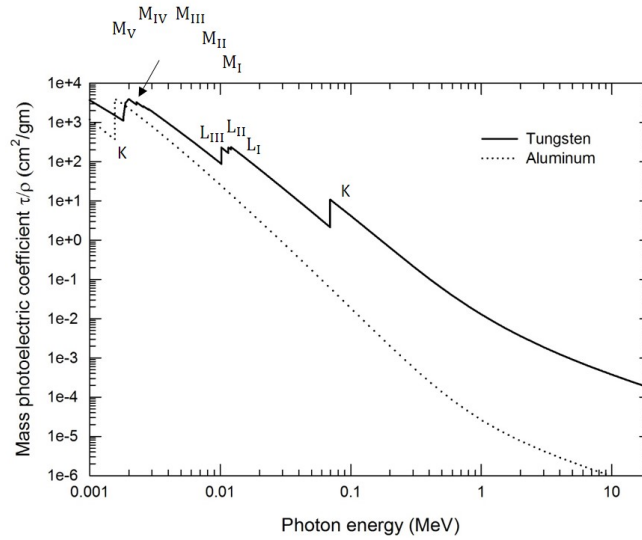


Figure 3.2: Mass absorption coefficients corresponding to the photoelectric process as a function of photon's energy on tungsten and aluminum.

3.2 Incoherent or Compton scattering

Compton scattering is a very common type of interaction that x-rays have with the medium through which they pass. In this process, an x-ray photon collides

with a nearly free electron and transfers some of its energy to the electron and the electron travels away at some angle θ off the direction of incident photon, as shown in Figure 3.3. The incident photon with reduced energy scatters off in a different direction, at a different angle ϕ . The amount of energy transferred to the electron in a Compton scattering depends on the energy of the photon and the angle at which the photon scatters relative to its incoming direction [2].

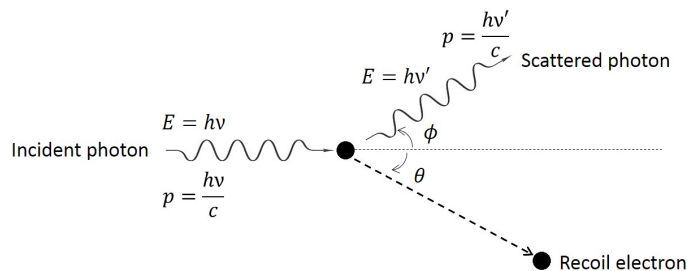


Figure 3.3: Diagram illustrating the Compton scattering of an x-ray photon by a free electron.

The cross section of the Compton scattering depends mainly on the energy of incident photon and is almost independent of atomic number of the medium because it essentially involves only free electrons [4]. The mass absorption cross-section corresponding to the Compton scattering as a function of photon energy in two different elements: tungsten and aluminum, are shown in Figure 3.4 [44].

The mathematical expression for the cross section of the Compton scattering was derived by J.J. Thomson using the classical theory of electromagnetic radiation. The Thomson's scattering cross section formula improved by using quantum theory of electromagnetic radiation is given by Klein-Nishina formula. According to the Klein-Nishina formula, the majority of the photons get scattered in forward direction, i.e. towards the original direction of the incident photon. And the photons that are scattered off at small angles lose only small fraction of their initial energy and those scattered off at greater angles lose more energy. [2, 45].

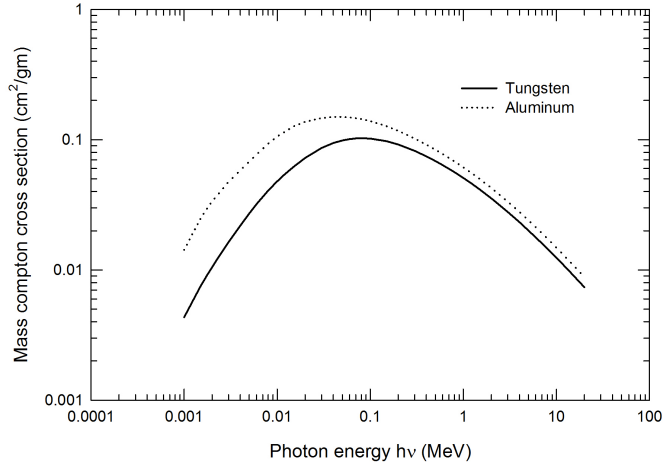


Figure 3.4: Mass absorption coefficients corresponding to the Compton scattering process as a function of photon energy.

3.3 Pair production

When a photon with energy greater than 1.02 MeV interacts strongly with the electromagnetic field of an atomic nucleus then an electron-positron pair is produced and the photon completely disappears. This process is called the pair production. Since the minimum energy that either an electron or positron possess is its rest mass energy, 0.511 MeV, the minimum energy a photon to have to cause pair production is 2×0.511 MeV. This is why 1.02 MeV is considered as a threshold energy for a photon to have pair production. If a photon has more than 1.02 MeV the excess energy after having pair production is shared by the electron and the positron as their kinetic energy [4].

The cross section of photons with energy greater than 1.02 MeV to have pair production increases with the increase of the atomic number of the medium as shown in Figure 3.5. Although for diagnostic (kilovolt) x-rays we observe no pair production, we will consider this effect in the calculations involved in megavolt x-rays in this project.

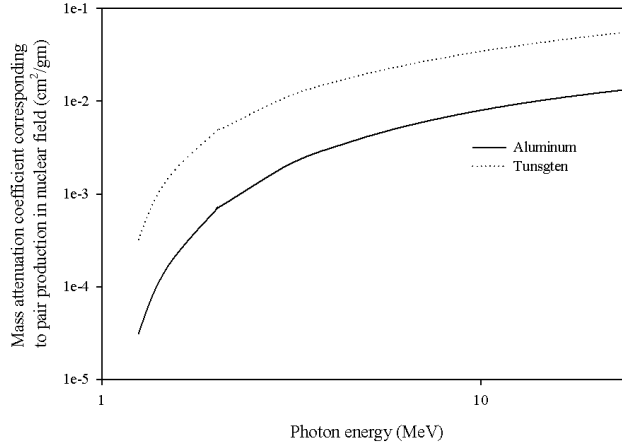


Figure 3.5: Mass absorption coefficients corresponding to the pair production in nuclear field as a function of photon's energy on tungsten and aluminum.

3.4 Total absorption cross section (μ)

The fraction of x-ray photons that interact per unit thickness of an absorber through which they pass is called the total absorption cross section (μ). In other words, μ is the probability that an x-ray photon interacts with a material. Since the relative probability of each type of interaction is proportional to the cross-section for that process, the probability of an interaction (μ) is the sum of the cross-sections: [2]

$$\mu = \tau + \sigma_{coh} + \sigma_{inc} + \kappa, \quad (3.1)$$

where τ is the photoelectric absorption coefficient, σ_{coh} is the coherent (Rayleigh) scattering coefficient, σ_{inc} is the incoherent (Compton) scattering coefficient and κ is the pair production coefficient (sum of the pair production coefficients in the electronic and the nuclear field). In low Z materials, σ_{coh} is usually negligible except at very low energies (< 10 keV).

Figure 3.6 shows plots of the total mass absorption coefficient and the mass

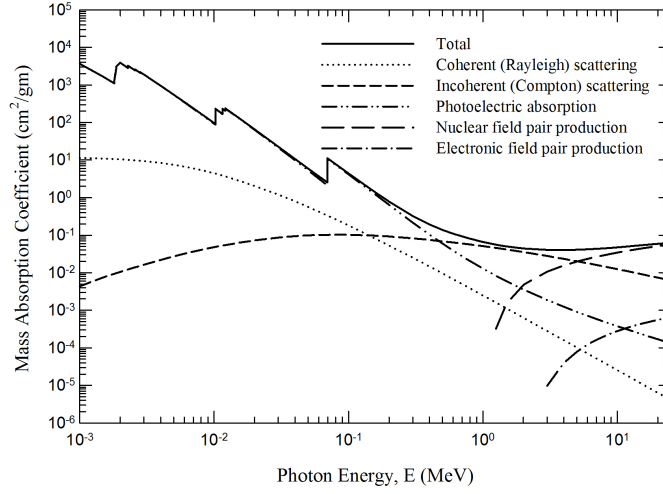


Figure 3.6: Mass attenuation coefficient for various interaction between photons and tungsten. Data is taken from NIST database [44]

absorption coefficient corresponding to four different interactions on tungsten ($Z = 74$) as a function of photon energy.

At low energies (< 0.1 MeV), the photoelectric effect dominates all other types of interaction. For the photons with energies from 0.1 MeV to 0.5 MeV the interaction is dominated by photoelectric absorption but in this region the photons also have Compton scattering. Both the photoelectric absorption and Compton scattering contribute to the total attenuation coefficient. The Compton scattering dominates all other types of interaction when the photons have energies between 0.5 MeV and 5.0 MeV. Above 5 MeV the pair production dominates all other interactions. And for the x-rays with energies from 1 keV to 25 MeV the mass coherent (Rayleigh) scattering coefficient is very small and contributes negligibly to the total attenuation coefficient.

Additionally, Figure 3.7 shows relative scales of the three major interaction between the photons and the absorbers of different Z . We can see that in the diagnostic radiography, the photoelectric absorption and the Compton scattering are very important (i.e. $\mu = \tau + \sigma_{inc}$). And in the radiation therapy with the unfiltered beams

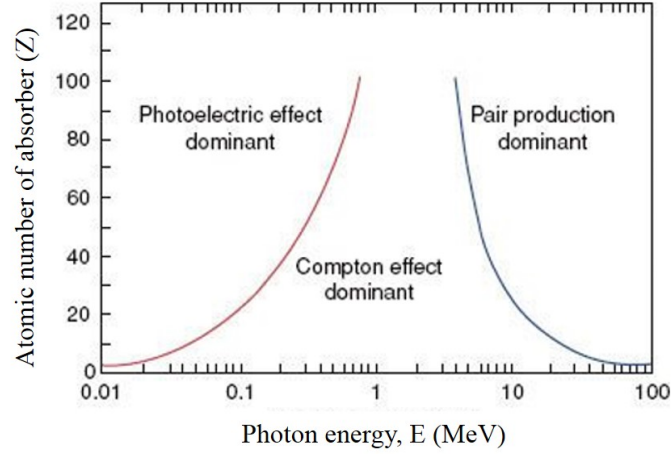


Figure 3.7: Relative importance of three major interactions between the photons and absorbers as a function of photon energy and atomic number of the absorber. [46]

of x-rays, all three interactions should be considered (i.e. $\mu = \tau + \sigma_{inc} + \kappa$). [46]

National Institute of Standards and Technology (NIST) provides a web program called XCOM which can generate the attenuation coefficients for all the elements, compounds and mixtures, at energies between 1 keV and 100 GeV. XCOM provides total attenuation coefficients and partial cross sections for the following processes: incoherent scattering, coherent scattering, photoelectric absorption, and pair production. The attenuation coefficients obtained from the XCOM program of NIST database are scientifically accepted benchmarks. [47]

Chapter 4

Energy spectrum of an x-ray beam

4.1 Energy spectrum of bremsstrahlung x-rays

There are several factors that determine the spectral shape of x-rays including accelerating voltage applied to accelerate the electrons, multiple bremsstrahlung interactions within the target and filtration in the beam [4]. Before discussing the actual shape of the spectrum, the theoretically expected shape of the spectrum from a thin target is discussed below.

4.1.1 Thin target spectrum

Ideally, a thin target refers to one in which a beam of electrons passes through in such a way that the electrons (i) do not lose a significant amount of energy by ionization, (ii) have no second radiative collisions, and (iii) do not undergo significant elastic scattering. It has been observed that the intensity of bremsstrahlung x-rays measured in a particular direction in each energy interval due to a beam of monoenergetic electrons of energy T incident on a thin target is constant from 0 to $h\nu_{max}$ (where $h\nu_{max} = T$) and cuts off abruptly at $h\nu_{max}$ as shown in Figure 4.1. In this figure, the intensity on the y-axis is proportional to the product, [(number of photons) \times (energy per photon)] and hence $N_1 E_1 = N_2 E_2 = \dots = \text{constant}$. Therefore the probability of

the emission of a photon with energy $h\nu_{max}/2$ is 2 times the probability of the emission of a photon with energy $h\nu_{max}$. Similarly, the probability of emitting a photon with energy $h\nu_{max}/5$ is 5 times the probability of emitting a photon with energy $h\nu_{max}$ and so on. [2]

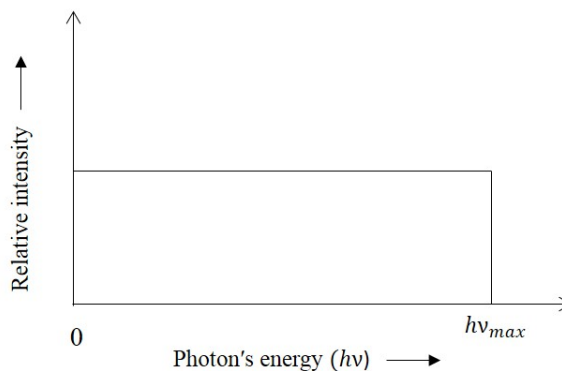


Figure 4.1: Relative intensity in each photon energy interval produced when a beam of monoenergetic electrons of energy $T = h\nu_{max}$ incident on a thin target. [43]

If we plot the number of photons per energy interval against energy we will obtain a curve as shown in Figure 4.2. Despite the different shape of the curves in Figure 4.1 and 4.2, each of them contains the same information. In Figure 4.2, the area under the curve gives the total energy radiated which is equal to the area under the curve in Figure 4.1 and is proportional to the maximum energy $h\nu_{max}$. Additionally, the area under the curve is also proportional to the atomic number of the target. Therefore, the energy of the bremsstrahlung photons radiated from a thin target is proportional to $E \cdot Z$. This agrees very well with the experimental result for electrons with energy up to 100 keV and agrees partially with the higher energy electrons.

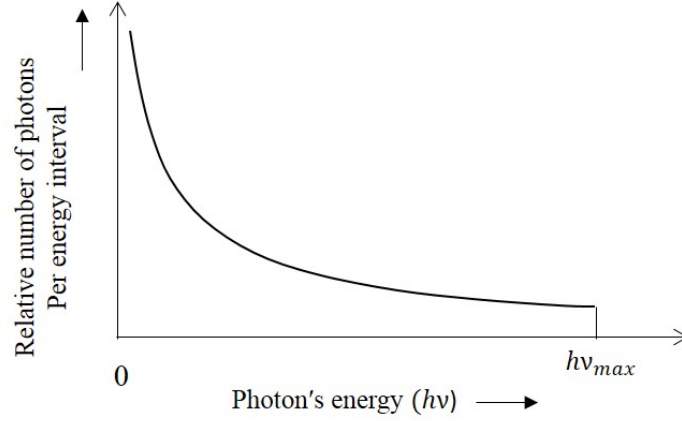


Figure 4.2: Relative number of photons in each photon energy interval produced when a beam of monoenergetic electrons of energy $T = h\nu_{max}$ incident on a thin target. This is the distribution of the data in Figure 4.1 converted into a number distribution. [2, 43]

For a beam of electrons with non-relativistic energy, the intensity of the bremsstrahlung photons in a particular energy interval and in a particular direction is proportional to $1/T$. This is an important feature which can be used to estimate the spectral shape of the bremsstrahlung photons from a thick target. The shape of the bremsstrahlung spectrum from a thin target is independent of the atomic number of the target (Z). Additionally, the experiments done with the thin targets show that the intensity of the bremsstrahlung photons from a thin target has an angular dependence on the energy of the incident electrons. For low energy electrons, the radiation intensity is maximum at right angles to the direction of the incident electrons. And the maximum of the radiation intensity moves forward with the increase of energy of incident electrons. [2, 48, 49]

4.1.2 Thick target spectrum

A thin target is an ideal case which is rarely met in practice. In a real situation, the target used to produce x-rays (in an x-ray tube or a linac) is thick

so that the incident electrons experience multiple elastic scattering, have multiple radiative collisions and lose a significant fraction of their energy by ionization. The spectral distribution of a thick target bremsstrahlung spectrum can be considered as the sum of the contributions from a number of thin-target cases of varying electron energies.

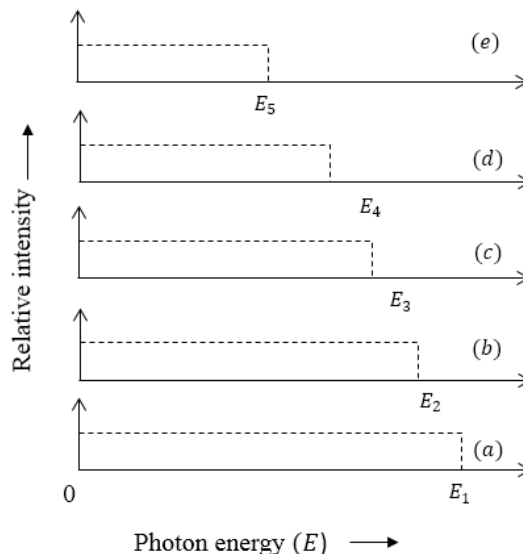


Figure 4.3: Relative intensity in each photon energy interval produced by different monoenergetic beams of electrons with energies E_1, E_2, E_3, \dots are incident on thin targets. [2]

When a beam of electrons with energy E_1 hits the surface of a thick-target, the electrons may produce x-rays from the top thin layer whose spectral distribution is as shown in Figure 4.3 (a). After passing through the first thin layer, the energy of electrons decreases to E_2 and the spectral distribution of x-rays produced from the second thin layer is as shown in Figure 4.3 (b). Similarly, when the electrons get into the third thin layer of the target the spectral distribution corresponding to the energy E_3 of the electrons looks like that shown in Figure 4.3(c). This process continues until the primary electrons finally stop in the thick-target. The total spectrum will then be the superposition of all the thin target spectra for energies E_1, E_2, E_3, \dots as illustrated

in Figure 4.4.

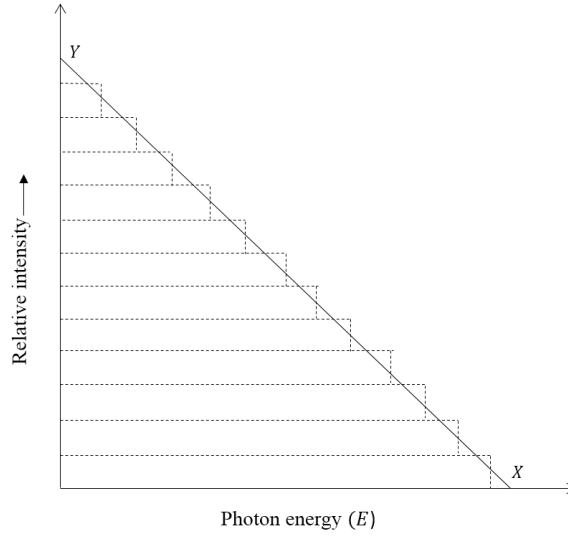


Figure 4.4: Relative intensity in each photon energy interval produced by a thick target shown as a superposition of thin target spectra. [2, 43]

The total spectrum shown in Figure 4.4 can be represented by a straight line XY whose equation is given by,

$$I(E) = CZ(E_{max} - E), \quad (4.1)$$

where $I(E)$ is the intensity of the photons with energy E , C is a constant, Z is the atomic number of the target and E_{max} is the maximum energy of the photons (given by $E_{max} = T$, the initial energy of the incident electrons).

The integration of equation 4.1 over all energies from 0 to E_{max} gives the total bremsstrahlung energy in MeV per electron:

$$I = kZE_{max}^2, \quad (4.2)$$

where k is a constant with dimension $1/\text{MeV}$ and E_{max} is in MeV.

The spectrum in Figure 4.4 represents the relative intensity [(number of

photons) \times (energy per photon)] of the photons in each photon energy interval from a thick target at a point very close to the surface of the target and assumes the contribution from each of its thin layers is not affected by any other factors. In this sense, this is still an ideal shape of the bremsstrahlung spectrum.

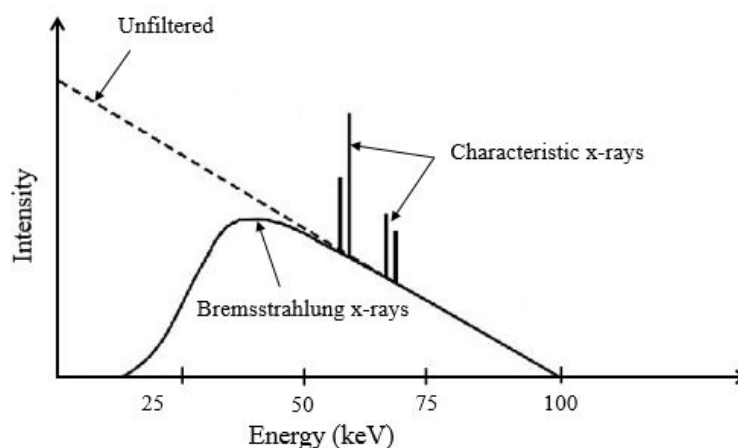


Figure 4.5: Diagram of an ideal shape of a 100 kV x-ray spectrum showing the effects of attenuation through the medium before reaching the detector. [1]

In reality, when a beam of monoenergetic electrons penetrates the surface of a thick-target, the electrons are attenuated in the target. The electrons can interact at any depth within the target and produce x-rays of various energies. The x-rays produced from the surface may have greater energy in comparison to the x-rays from a deeper part of the target since x-rays are produced by the electrons of full initial energy. The x-rays produced in a deeper region of the target are attenuated as they escape because of the much larger values of the attenuation coefficient (μ) at low energies (Figure 3.6). All the photons coming out of the target surface then have to pass through the window of the tube and any added filter or media between the tube and the point where these are actually used or detected. Since the inherent filtration cuts off the low-energy end of the spectrum, the shape of the spectrum changes from the one shown in Figure 4.4. If the energy of electrons is high enough, the final spectrum also includes characteristic x-rays produced in the target and possibly the detector and

any intermediate matter of appropriate energy.

Figure 4.5 shows the energy spectrum of a beam of x-rays from a typical 100 *kV* x-ray tube with a Tungsten target. The dotted line represents the relative intensity of photons from the unfiltered beam. The solid curve is the relative intensity after taking account the inherent filtration. The characteristic lines of appropriate energies for Tungsten are also shown in the diagram.

In megavoltage x-ray therapy, electrons are accelerated to comparatively much higher energies ($\sim 1 - 25$ MeV) before striking a target to produce therapeutic x-rays. X-rays produced by an interaction of electrons with kinetic energy E with a target have energy between 0 and E . However, the lower energy x-rays including the characteristic x-rays in the beam are often absorbed by inherent filtration that the x-ray beam encounters before exiting the linac head. This causes the minimum photon energy of a therapeutic x-ray beam to shift to an energy larger than 100 keV. A therapeutic x-ray beam therefore contains only the bremsstrahlung x-rays but not the characteristic x-rays produced by the target. The energy spectrum of a therapeutic x-ray beam is therefore a continuous function of energy and possess a single peak and no valleys.

4.2 Determination of the energy spectrum of an x-ray beam

Historically there are mainly three methods that have been used to determine the energy spectra of the clinical x-ray beams. These are (i) direct measurement using specialized detectors, (ii) theoretical calculation with and without the use of Monte Carlo simulation, and (iii) determination using measured dose-depth datasets.

4.2.1 Direct measurement of the energy spectrum of x-rays

Using the x-ray spectroscopy technique, a few attempts have been made in the past to measure the energy spectra of x-ray beams. The common detectors found in literature include High-purity Germanium (HPGe) [8], Thallium activated sodium iodide (NaI(Tl)) [13, 14], and silicon semiconductors, each coupled to a pulse pile-up rejector/restorer circuit. But none of these detectors can be used to measure a pristine energy spectrum of a kilovolt or megavolt x-ray beam, since the extremely high photon flux of a clinical x-ray beam causes signal pile-up, and saturation-induced dead times in the detector.

In the case of solid-state detectors, the thickness of the detector required to measure the energy of high energy photons (up to 20 MeV) needs to be very large in order to capture all the ionization induced by an x-ray photon. This makes the detector very costly and requires a sophisticated calibration. The direct measurement of the energy spectrum of an x-ray beam is therefore impractical to carry out on routine basis. Additionally, the measured x-ray spectra need to be corrected for the geometry in which the measurements were made in order to obtain the pristine x-ray spectra. This includes a tedious and time consuming calculation, often using Monte Carlo simulation.

4.2.2 Theoretical calculation of the energy spectrum

The method of determining energy spectrum of an x-ray beam from first principles is the most reliable and powerful method. The use of Monte Carlo techniques makes the calculation very efficient and accurate. This method simulates the direct transport of electrons into a target to generate x-rays and then transports the x-rays through various filters to determine x-ray energy spectra. Monte Carlo codes such

as National Research Council of Canada’s Electron Gamma Shower (EGSnrc) [50], Monte Carlo N-Particle (MCNP) [51], GEometry ANd Tracking (GEANT4) [52], and Integrated Tiger Series (ITS) [53] are common Monte Carlo codes that were used to calculate the energy spectra of various clinical x-ray beams [16–21].

To get an accurate energy spectrum of an x-ray beam, Monte Carlo simulation requires detailed information about the geometry of the x-ray machine. The required information includes the material, composition and physical dimensions of various components such as the target, flattening filter, shielding plates, collimators, etc. Due to their proprietary nature, it is often impossible to get this detailed information regarding the internal components of specific models of clinical x-ray machines. Even with detailed and accurate geometric specifications of a linac, large uncertainties in the most important parameters needed for the simulation such as the electron beam energy and intensity distributions can result to spurious and misleading x-ray spectra results [54]. Additionally, it is often very time consuming and difficult to repeat the calculation involved in a Monte Carlo simulation designed for one specific x-ray linac for other machines, since each model of x-ray linac has a unique geometry.

4.2.3 Method of using dose-depth data

The method of determining x-ray energy spectrum using dose-depth data, measured with an absorber of known composition in the beam, is more common for practical reasons. It is more convenient because it is easy to carry out in any x-ray machine and the dose-depth datasets required by the calculation can be measured in a relatively simple way. However, the accuracy of the spectrum derived from attenuation data depends on the accuracy of the measurement of the attenuation data. A small error introduced in the attenuation data can greatly affect the shape of the spectrum.

The intensity of a beam of monoenergetic x-rays (an ideal x-ray beam) with energy E after passing through an absorber of thickness x is given by: [2]

$$I(x) = s(E)e^{-\mu(E)x}, \quad (4.3)$$

where $s(E)$ is the intensity of the beam before attenuation through the absorber and $\mu(E)$ is the total mass attenuation coefficient for x-rays of energy E on the absorber material. The unit of $\mu(E)$ is chosen in such a way that the product $\mu(E)x$ is dimensionless. In equation (4.3), $I(x)$ represents the intensity of only the primary x-rays which do not experience any interaction while passing through the absorber and does not include any secondary x-rays produced during the interaction with absorber.

The intensity of a beam of multienergetic x-rays, a relatively more realistic situation, with N different energies, E_i , $i = 1, 2, \dots, N$, after passing through an absorber of thickness x is given by the sum of the intensities of x-rays with all energies:

$$I(x) = \sum_{j=1}^N s(E_j)e^{-\mu(E_j)x}, \quad (4.4)$$

where $s(E_j)$ is the intensity of x-rays with energy E_j before attenuation in the absorber and $\mu(E_j)$ is the total attenuation coefficient for x-rays of energy E_j on the absorber material.

In a real situation, a clinical x-ray beam consists of characteristic x-rays with few discrete energies corresponding to the absorption edges of the electron target and bremsstrahlung x-rays which can have any energy between some minimum energy E_{min} to the maximum energy (E_{max}). Considering a sufficiently large value of N , the intensity of an x-ray beam after attenuation through an absorber of thickness x can still be calculated using equation (4.4). However, it is more accurate to replace the

summation in equation (4.4) by an integral: [22]

$$I(x) = \int_{E_{min}}^{E_{max}} s(E)e^{-\mu(E)x}, \quad (4.5)$$

where $s(E)$ represents the spectral distribution.

The intensity of an attenuated x-ray beam can be measured by detectors such as ionization chambers and solid state detectors, and is often quantified in terms of exposure in air. A set of measurements $I(x_i)$, of an x-ray beam attenuated by absorber of different thicknesses, x_i , is called dose-depth dataset. Since the exposure measured behind an absorber of a given thickness is directly proportional to the intensity of x-ray beam attenuated by the absorber, the dose-depth dataset $(x_i, I(x_i))$ is related to the energy spectrum of the beam $(E_j, s(E_j))$ by the following equations:

$$\begin{aligned} I(x_1) &= s(E_1)e^{-\mu(E_1)x_1} + s(E_2)e^{-\mu(E_2)x_1} + \dots + s(E_N)e^{-\mu(E_N)x_1}, \\ I(x_2) &= s(E_1)e^{-\mu(E_1)x_2} + s(E_2)e^{-\mu(E_2)x_2} + \dots + s(E_N)e^{-\mu(E_N)x_2}, \\ &\dots \\ I(x_n) &= s(E_1)e^{-\mu(E_1)x_n} + s(E_2)e^{-\mu(E_2)x_n} + \dots + s(E_N)e^{-\mu(E_N)x_n}, \end{aligned} \quad (4.6)$$

or by the integral equation:

$$I(x) = \int_0^{E_{max}} s(E)e^{-\mu(E)x}dE, \quad (4.7)$$

In equation (4.6), n is the number of data points in the measured dose-depth dataset and N (chosen to be sufficiently large) is the number of bins spanning the x-ray energy spectrum. In equation (4.7), $I(x)$ is a function representing measured exposure as a function of the absorber thickness (x), and $s(E)$ is a function representing the initial intensity of the x-ray beam (before attenuation in the absorber) as a function of energy.

In other words, $s(E)$ represents the energy spectrum of the x-ray beam. Equations (4.6) or (4.7) are valid only if $I(x_i)$ or $I(x)$ represent(s) the intensity of only the primary x-rays that do not undergo any interaction while passing through absorber and exclude(s) the intensity of all the secondary x-rays produced due to the interaction of the primary x-rays with the absorber.

Direct numerical solution of equations (4.6) or (4.7) for the energy spectrum of an x-ray beam is not straightforward and it has always been considered as an ill-posed problem in the literature [22, 24, 37, 55]. A beam of x-rays contains bremsstrahlung x-rays with any energy between some minimum energy and the maximum energy, meaning that there can be infinitely different values of energy that photons can have. However, we can only have finite number of dose-depth data points measured in that beam. In other words, there are only a finite number of equations that relate the measured dose-depth dataset $(x_i, I(x_i))$ to the energy spectrum of an x-ray beam $(E_j, I_0(E_j))$. The solution of equations (4.6) or (4.7) is therefore not necessarily unique.

Different attempts can be found in the literature for solving either a discrete set of equations (4.6) or an integral equation (4.7) to obtain x-ray energy spectra. Three commonly used methods are: (i) the inverse Laplace transform method [22–25, 28–30, 32, 55–57], (ii) the matrix manipulation method, also called the direct matrix inversion method [35, 36, 58], and (iii) the computer iterative method based on expectation maximization or least square deconvolution [37–40, 58–65].

4.2.3.1 Inverse Laplace Transform

The integral equation (4.7) can be rewritten in the following form:

$$I(x) = \int_0^{\infty} s(E) e^{-\mu(E)x} dE, \quad (4.8)$$

If the absorber material is chosen in such a way that the mass attenuation coefficient for x-rays decreases monotonically with increasing energy, then a change of variable from photon energy (E) to mass attenuation coefficient can be made in equation (4.8) [25]:

$$I(x) = \int_0^{\infty} f(\mu) e^{-\mu x} d\mu, \quad (4.9)$$

where $f(\mu)$ is related to the the energy spectrum $s(E)$ by following relation:

$$f(\mu) d\mu = -s(E) dE, \quad (4.10)$$

where the negative sign represents the decrement of the mass attenuation coefficient with the increment of photon energy.

Equation (4.9) with (4.10) is an integral equation of first kind with $e^{-\mu x}$ as its kernel. By definition, $I(x)$ expressed in equation (4.8) is the Laplace transform of the function $f(\mu)$. Provided that an analytic function $g(x)$ represents a measured dose-depth dataset $(x_i, I(x_i))$, the energy spectrum of x-ray beam can be determined using the definition of inverse Laplace transform:

$$f(\mu) = \frac{1}{2\pi i} \lim_{\omega \rightarrow \infty} \int_{\gamma - i\omega}^{\gamma + i\omega} g(x) e^{\mu(E)x} dx, \quad (4.11)$$

and then using equation 4.10:

$$s(E) = -f(\mu) \left(\frac{d\mu}{dE} \right), \quad (4.12)$$

where $\frac{d\mu}{dE}$ represents the slope of the plot of mass attenuation coefficient as a function of photon energy.

To determine the energy spectrum of an x-ray beam using the inverse

Laplace transform method, the first step would be to find an appropriate function $g(x)$ that meets the following criteria:

- (i) $g(x)$ represents the measured dose-depth dataset $(x_i, I(x_i))$, i.e. $g(x) = I(x)$, for $x = x_i, i = 1, 2, \dots, n$.
- (ii) The inverse Laplace transform of $g(x)$, i.e. $f(\mu)$ exists and is a real function of μ .
- (iii) The shape of the energy spectrum derived from equation (4.12) is consistent with the common characteristics of published x-ray spectra.

Table 4.1 presents some of the special functions, $g(x)$, found in literature, each of which was found to satisfy the criteria mentioned above for a particular x-ray beam. The inverse Laplace transform calculated using equation (4.11) of the corresponding function $g(x)$ is presented in the second column of the table. The energy spectrum of x-ray beam is given by the product $f(\mu)$ and the slope $\left(-\frac{d\mu}{dE}\right)$ using equation (4.12).

An analytical function, $g(x)$, has to be chosen very carefully within the observed energy interval because an improper choice can give results without any physical sense [66]. In addition, there is no guarantee that the $g(x)$ used to represent one set of dose-depth data will correctly represent another dataset measured in a different x-ray beam with same or different nominal energy. An important assumption made in using Laplace transform pairs is that the mass attenuation coefficients ($\mu(E)$) decrease monotonically with increasing x-ray energy. This assumption is the main limitation of the inverse Laplace method because the mass attenuation coefficients of materials commonly used as absorbers first decrease monotonically and then start to increase at higher energies. For example, for copper and lead the mass attenuation coefficient has its minimum value at about 8 MeV and 4 MeV [44]. This causes the

Table 4.1: Analytical functions $g(x)$, used by various authors to represent measured dose-depth datasets and their inverse Laplace transforms. In the tabulated expressions, A , B , d , a_1 , a_2 , a_3 , b_1 , b_2 , b_3 , ν , A_k , and C_k ($k = 1, 2, \dots, N$) are the constants to be determined by fitting measured dose-depth datasets with $g(x)$; μ_0 is the mass attenuation coefficient on absorber for x-rays with maximum energy in an x-ray beam; E_k denote the energies of characteristic x-rays produced by electron target; and $I_{\nu-1/2}(\frac{(A-B)}{2}(\mu - \mu_0))$ is a modified Bessel function.

Authors	$g(x)$	Inverse Laplace transform of $g(x)$
Silberstein [23], Bell [29]	$e^{-Ax-B\sqrt{x}}$	$\frac{3\beta^{1/3}B}{2\sqrt{\pi}}\left(\frac{hc}{E^2}\right)(\mu - \alpha)^{2/3}(\mu - A)^{-3/2}e^{-\frac{B^2}{4(\mu-A)}}$
Jones [30]	$I_0 e^{-Ax-B(\sqrt{x+d}-\sqrt{d})}$	$\frac{I_0 B}{2\sqrt{\pi}}(\mu - A)^{-\frac{3}{2}}e^{-\frac{3}{2}(\mu-A)d+B\sqrt{d}-\frac{B^2}{4(\mu-A)}}$
Saylor [32]	$e^{-\mu_0 x} \left(a_1 e^{-b_1 \sqrt{x}} + a_2 e^{-b_2 \sqrt{x}} + a_3 e^{-b_3 \sqrt{x}} \right)$	$\frac{2}{\sqrt{\pi}}(\mu - \mu_0)^{-\frac{3}{2}} \left[a_1 b_1 e^{-\frac{b_1^2}{4(\mu-\mu_0)}} + a_2 b_2 e^{-\frac{b_2^2}{4(\mu-\mu_0)}} + a_3 b_3 e^{-\frac{b_3^2}{4(\mu-\mu_0)}} \right]$
Huang [55]	e^{-Ax+Bx^2}	$\frac{1}{2\sqrt{\pi}B}e^{-\frac{(\mu-A)^2}{4B}}$
Archer [24]	$\left(\frac{AB}{(x+A)(x+B)} \right)^{\nu} e^{-\mu_0 x}$	$\frac{\sqrt{\pi}(AB)^{\nu}}{\Gamma(\nu)} \left(\frac{\mu-\mu_0}{A-B} \right)^{\nu-\frac{1}{2}} e^{-\frac{(A+B)}{2}(\mu-\mu_0)} \times I_{\nu-\frac{1}{2}} \left[\frac{(A-B)}{2}(\mu - \mu_0) \right]$
Rubio [57]	$d \left(\frac{AB}{(x+A)(x+B)} \right)^{\nu} e^{-\mu_0 x} + C \sum_{k=1}^N A_k E_k \mu_a(E_k) e^{-\mu(E_k)x}$	$I_{\nu-\frac{1}{2}} \left(\frac{(A-B)}{2}(\mu - \mu_0) \right) e^{-\frac{(A+B)}{2}(\mu-\mu_0)} + \left[C \sum_{k=1}^N A_k E_k \mu_a(E) \delta(E - E_k) \right]$
Archer and Wagner [24]	$\alpha \left(\frac{AB}{(x+A)(x+B)} \right)^{\nu} e^{-\mu_0 x} + (1 - \alpha) \sum_{k=1}^N C_k \delta(E - E_k)$	$\frac{\alpha \sqrt{\pi}(AB)^{\nu}}{\Gamma(\nu)} \left(\frac{\mu-\mu_0}{A-B} \right)^{\nu-1/2} e^{-\frac{(A+B)}{2}(\mu-\mu_0)} \times I_{\nu-1/2} \left(\frac{(A-B)}{2}(\mu - \mu_0) \right)$

slope $\left(-\frac{d\mu}{dE} \right)$ to be zero at an x-ray energy, E' , at which $\mu(E)$ has its minimum value and hence the relative intensity at and above E' will either be zero or negative, resulting

a non-physical spectral shape. For this reason, the inverse Laplace transform method generally cannot be successfully used to determine the energy spectra of therapeutic x-ray beams.

4.2.3.2 Direct inversion of Matrix

The discrete sets of equations (4.6) can be represented as a matrix equation of the following form:

$$[I(x)]_{n \times 1} = [A]_{n \times N} \cdot S_{N \times 1}, \quad (4.13)$$

where $[I(x)]_{n \times 1}$ is a column vector of measured intensity of x-ray beams attenuated by absorber of varying thicknesses; $S_{N \times 1}$ is a column vector of the intensity of x-rays before attenuation through absorber and it represents the energy spectrum; and $[A]_{n \times N}$ is a matrix whose elements $(A_{i,j})$ are given by

$$A_{i,j} = e^{-\mu(E_j)x_i}. \quad (4.14)$$

The energy spectrum of an x-ray beam can be determined by finding the inverse of matrix $[A]_{n \times N}$ such that: [35, 36, 58]

$$S_{N \times 1} = [A]_{n \times N}^{-1} \cdot [I(x)]_{n \times 1}. \quad (4.15)$$

The matrix $[A]_{N \times N}$ is nearly singular as its determinant is very small and consequently not directly invertible. By using some indirect method of matrix inversion such as spectral vectorial algebra or singular value decomposition, the matrix $[A]_{N \times N}$ can be inverted [36, 67]. However, there is no guarantee that the elements of the inverted matrix, $[A]_{N \times N}^{-1}$, are necessarily all positive. This may lead to a spectrum containing negative values for the relative intensity of x-rays, a non-physical solution.

By using a non-negative least squares method, it is possible to restrict the solution to be positive while inverting the matrix $[A]_{N \times N}$.

4.2.3.3 Iterative perturbation method

The iterative perturbation method, originally proposed by Waggener [37], is the most common method of determining the energy spectra of x-ray beams found in the literature. This method is fairly simple to implement and probably provides the best approximate energy spectra of x-ray beams with nominal energies ranging from 25 kVp to 25 MVp [37].

The iterative perturbation method starts with an estimated energy spectrum, referred to hereafter as the guess spectrum, containing equally spaced energy bins between an estimated minimum photon energy and the maximum photon energy. In principle, the guess spectrum can have any shape, but should contain only positive and real values of x-ray intensity. The initial guess x-ray spectrum is used to calculate a dose-depth dataset for the absorber material that is then compared to the measured dose-depth dataset. Unless the guess spectrum happens to be very close to the actual energy spectrum of the beam, the calculated dose-depth dataset significantly differs from the measured dose-depth dataset. The relative intensity of x-rays in each energy bin is then iteratively perturbed, both positively and negatively, and the guess spectrum is updated to the one which leads the calculated dose-depth data to better agree with the measured data.

In comparison to the inverse Laplace transform and the direct inversion of matrix method, the iterative method has proven to successfully generate realistic energy spectra of both diagnostic and therapeutic x-ray beams [37, 63, 68–71]. However, this method also has some drawbacks such as: (i) the energy spectrum estimated

by this method contains unrealistic spectral features (i.e. peaks and valleys), (ii) the convergence of the calculation depends on the shape of the guess energy spectrum, and (iii) the shape of the estimated energy spectrum is affected by the choice of estimated minimum x-ray energy.

In this project, an algorithm based on Waggener's iterative perturbation method with some modification was used to estimate the energy spectra of therapeutic x-ray beams with different nominal energies. To overcome the first drawback listed above, a method of smoothing the estimated energy spectra, to eliminate non physical features in the spectrum was developed. This approach is described in greater detail in Chapter 5 and the method of smoothing the calculated x-ray spectra is described in Chapter 6. Similarly, the dependency of the estimated spectral shape on the shape of guess energy spectrum and estimated minimum photon energy were systematically studied.

Chapter 5

Algorithm for estimating x-ray energy spectra

5.1 Description of algorithm

An algorithm based on an iterative perturbation method was developed to estimate the energy spectrum of an x-ray beam using measured dose-depth data. This algorithm starts with an initial x-ray energy “guess” spectrum which is then iteratively improved until the dose-depth dataset calculated using the increasingly modified spectrum agrees with the measured dose-depth dataset within a predetermined limit. An x-ray energy spectrum estimated by this algorithm is then validated by calculating a dose-depth dataset for a different absorber material and comparing that with the dose-depth dataset measured for that different material.

This algorithm does not use information regarding the internal structure or geometry of the x-ray machine. Required inputs include the material composition of the absorber, the minimum photon energy, the maximum photon energy, and an estimated peak energy in the spectrum. The mass attenuation coefficients for x-rays as a function of energy between the estimated minimum energy and the maximum energy in the x-ray beam, for the absorber material are also required.

A dose-depth dataset required to estimate the energy spectrum of an x-ray beam is a set of exposures ($I_m(x_i)$) due the beam attenuated by absorber of varying thicknesses (x_i). The subscript m in $I_m(x_i)$ stands for “measured”. For a better accuracy of the estimated x-ray spectrum, the measured dose-depth data used in the algorithm must represent the attenuation of only the primary x-rays and should exclude all secondary x-rays such as those produced by Compton scattering. Each of the dose-depth datasets presented in Tables 7.2–7.4 was measured in a narrow beam geometry as described in Chapter 7.2, in order to meet this condition.

Interpolation was carried out on the measured dose-depth dataset in order to produce the same number of data points as the desired number of energy bins (N) in the energy spectrum of x-ray beam. The interpolation was done by fitting the measured dose-depth dataset with a polynomial of degree 3 of the form:

$$f(x) = a_0 + a_1x + a_2x^2 + a_3x^3, \quad (5.1)$$

where a_0 , a_1 , a_2 , and a_3 are constants whose values were found by a process of minimizing the sum of the squares of the errors:

$$err = \sum_{i=1}^n (f(x_i) - I_m(x_i))^2, \quad (5.2)$$

where n is the number of measured data points. Then the intensity of the beam ($I(x_i)$) behind the absorber of thickness x_i between x_1 and x_n was found by using equation 5.1.

By interpolating the measured dose-depth dataset, the exposure $I(x_i)$ due to the beam attenuated by the absorber of thickness x_i was obtained, for equal increments of $\Delta x = \frac{x_n - x_1}{N-1}$, where N is the desired number of energy bins in the spectrum.

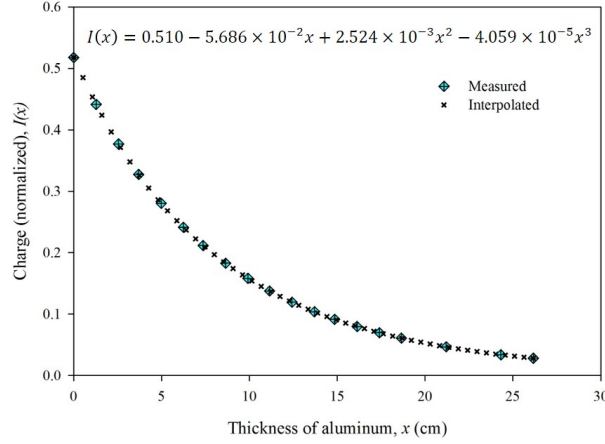


Figure 5.1: Interpolation of the measured dose-depth dataset using a polynomial of degree 3. The measured dose-depth dataset containing 19 data points has been interpolated to get 50 data points for equally spaced thicknesses of $\Delta x = 0.53$ cm.

Figure 5.1 shows an example of a dose-depth dataset before and after the interpolation. The measured dose-depth dataset was taken from table 7.2 which consists of 19 data points. It was interpolated by a polynomial of degree 3 into 50 data points for equally spaced thickness of $\Delta x = 0.53$ cm. The polynomial that was used to interpolate the measured dose-depth dataset is also shown in the same graph.

Figure 5.2 shows a block diagram illustrating the main steps for an estimation of an x-ray energy spectrum with the help of a measured dose-depth dataset. A part of the block diagram in Figure 5.2, labeled as “Box 1”, is shown in Figure 5.5.

First, the number of energy bins in the spectrum (N), minimum energy of x-rays in the beam (E_1), and the maximum energy of x-rays (E_N) are defined as shown in row (A) of the block diagram. The value of E_N is always chosen to be equal to the kinetic energy of the electrons beam accelerated by the linac and incident on the electron target. The value of N is chosen to be any arbitrary positive integer. The value of E_1 is chosen based on the following two facts: (i) the x-rays produced by an interaction of electrons with energy E_N with the electron target in an x-ray machine

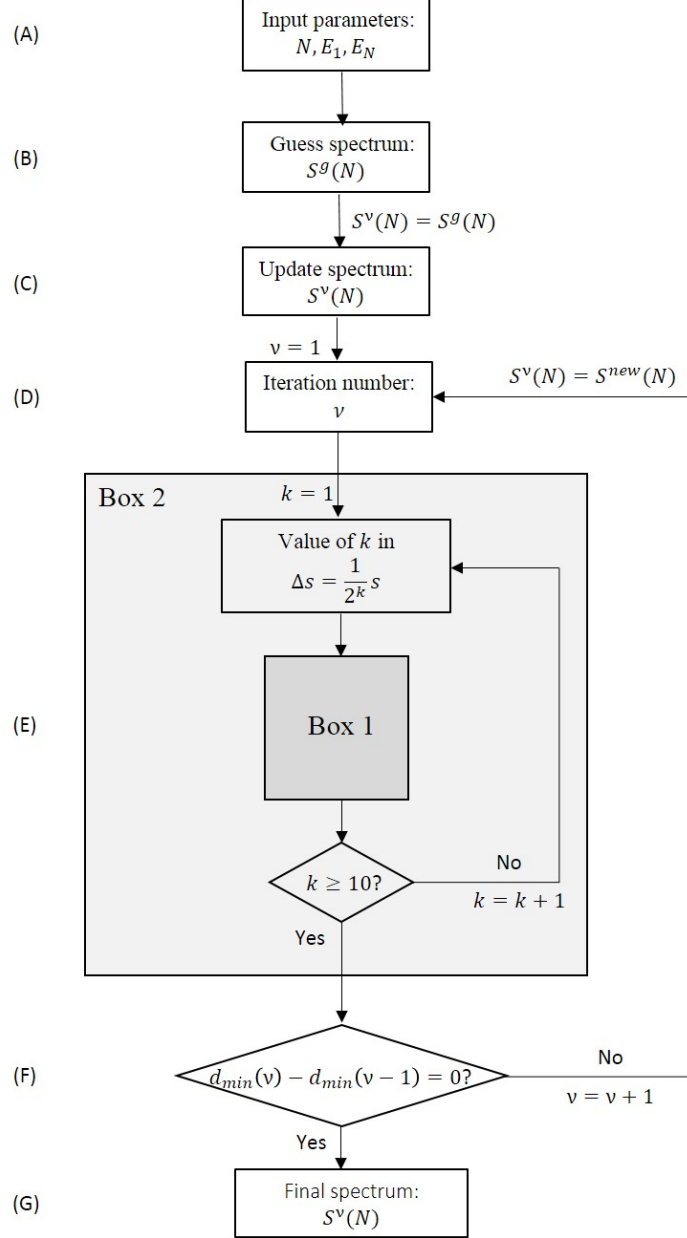


Figure 5.2: Block diagram illustrating the main steps for use in estimating the energy spectrum of an x-ray beam using a measured dose-depth dataset. The calculation inside the box labeled as “Box 1” is shown in Figure 5.5.

will have energy between 0 and E_N , and (ii) the low energy x-rays in the beam are often absorbed by inherent filtration that the x-ray beam encounters before exiting the gantry. This causes the minimum energy of x-rays to shift to a value greater than zero. Since we don’t know precisely the amount of filtration, the value of E_1 is chosen based on the estimated amount of filtration in the beam. The accuracy of this estimation is

often quite poor.

Based on the values of N , E_1 , and E_N , a guess spectrum $S^g(N)$ containing equally spaced energy bins, each of width $\Delta E = \frac{E_N - E_1}{N-1}$, is defined as shown in row (B) of Figure 5.2. A guess spectrum can be of any shape, but the following points should be considered when defining a guess spectrum:

- i) There can be no x-rays with energies less than E_1 and greater than E_N .
- ii) The intensities of photons of a given energy in an x-ray beam are always positive and real numbers including zero.
- iii) The x-rays in a therapeutic x-ray beam are mostly the result of bremsstrahlung interactions within the electron target and filtration in the beam. The intensity of characteristic x-rays produced by the processes of excitation and ionization caused by accelerated electrons within the electron target and filtration is negligibly small for MVp beams.
- iv) The relative intensity of x-rays changes continuously as a function of the photon energy and asymptotically approaches to zero at the maximum photon energy (E_N).
- v) Due to an effect of the inherent filtration that an x-ray beam experiences before exiting a linac, the average x-ray energy is approximately one-third of the maximum energy [2, 4].

A guess spectrum ($S^g(N)$) for use in estimating the x-ray energy spectrum of each of the therapeutic beams considered in this project, that satisfies the criteria mentioned above, is defined in terms of a modified lognormal distribution of the following form:

E_1	E_2	\dots	E_j	\dots	E_{N-1}	E_N
s_1^g	s_2^g	\dots	s_j^g	\dots	s_{N-1}^g	s_N^g

where, $E_j = E_1 + m \cdot \Delta E$; $m = 0, 1, \dots, N - 1$ represents the average photon energy in the j^{th} energy bin, $\Delta E = \frac{(E_N - E_1)}{(N-1)}$ is the width of each energy bin, and s_j^g denotes the “guess” relative intensity of x-rays of energy E_j calculated by,

$$s_j^g = \frac{1}{\sigma \sqrt{2\pi} E_j} e^{-\frac{(\ln E_j - \bar{E})^2}{2\sigma^2}}, j = 1, 2, \dots, N. \quad (5.3)$$

Here, \bar{E} and σ are the average and standard deviation of $\ln(E_j)$, $j = 1, 2, \dots, N$, respectively. Depending on the choice of minimum energy (E_1), the value of σ was modified to σ/C , where C is an arbitrary positive number, in order to get the peak of a guess spectrum approximately at $1/3^{rd}$ of the maximum photon energy. The algorithm was also tested with few different shapes of the guess spectra such as Gaussian, triangular, etc. The guess spectrum was normalized before implementing to the algorithm so that the area under the curve was 100.

Figure 5.3 shows an example of a guess energy spectrum for use in estimating a 6 MVp x-ray beam. It consists of 50 energy bins and the minimum photon energy of 0.1 MeV. The relative intensity in each energy bin with average photon energy E_j was calculated by using equation (5.3) with $\bar{E} = \frac{\sum_{j=1}^N \ln E_j}{N} \approx 0.84$ MeV and $\sigma \rightarrow \sigma(\ln E_j, j = 1, 2, \dots, N)/2.5 \approx 0.36$.

In the next step, shown in row (C) of Figure 5.2, an energy spectrum $S^\nu(N)$ is set to be equal to the guess spectrum $S^g(N)$, i.e.

$$s_j^\nu = s_j^g, j = 1, 2, \dots, N$$

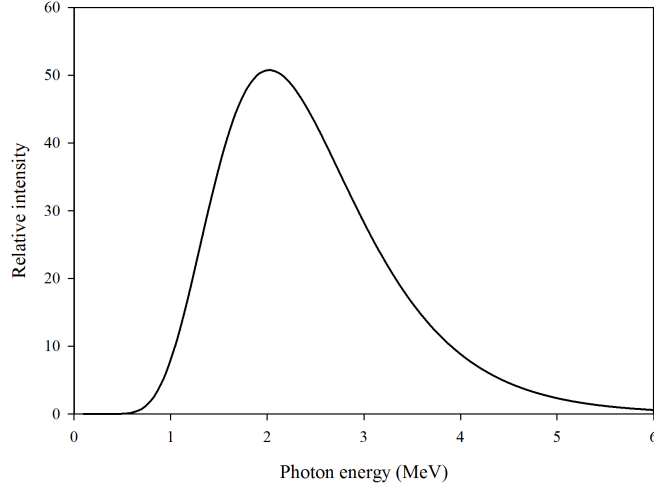


Figure 5.3: A guess spectrum containing 50 energy bins ($S^g(50)$) defined for use in estimating the energy spectrum of a 6 MVp x-ray beam. The minimum and the maximum photon energy are 0.1 MeV and 6 MeV respectively. The peak of the spectrum is at approximately 2.0 MeV.

where s_j^g is the estimated value for the relative intensity of x-rays with energy E_j , from equation 5.3. The superscript ν in $S^\nu(N)$ denotes that the spectrum is obtained at the end of the ν^{th} iteration. For the calculation with $S^\nu(N) = S^g(N)$, the value of ν is 0.

Based on the spectrum $S^\nu(N)$, the exposure $I_c^\nu(x_i)$, due to an x-ray beam attenuated by absorber of each thickness x_i is calculated:

$$I_c^\nu(x_i) = \sum_{j=1}^N s_j^\nu e^{-\mu(E_j)x_i}, i = 1, 2, \dots, N, \quad (5.4)$$

where $\mu(E_j)$ is the mass attenuation coefficient for x-rays with energy E_j on the absorber material and the suffix “c” in $I_c^\nu(x_i)$ stands for “calculated”. The mass attenuation coefficients for x-rays with energy ranging from the minimum x-ray energy to the maximum x-ray energy in the absorber material are taken from XCOM NIST database [44]. The units of attenuation coefficients are chosen based on the units of the thickness of absorber (x_i) such that the products $\mu(E_j) \cdot x_i$ (where $j = 1, 2, \dots, N$

and $i = 1, 2, \dots, N$) are dimensionless.

The set of N data points $(x_i, I_c^\nu(x_i))$ obtained from the calculation in equation (5.4) is referred to as the calculated dose-depth dataset. Prior to each iteration, the calculated dose-depth dataset $(x_i, I_c^\nu(x_i))$ is compared to the measured dose-depth dataset $(x_i, I(x_i))$ and the percent difference between the calculated and measured exposures due to the beam attenuated by an absorber of each thickness x_i is calculated:

$$d_i = \left| \frac{I_c^\nu(x_i) - I(x_i)}{I(x_i)} \right| \times 100\%$$

Then a total percent difference between the calculated and the measured dose-depth datasets is evaluated by summing d_{0i} calculated for each thickness x_i :

$$d = \frac{1}{N} \sum_{i=1}^N d_i = \frac{1}{N} \sum_{i=1}^N \left| \frac{I_c^\nu(x_i) - I(x_i)}{I(x_i)} \right| \times 100\%. \quad (5.5)$$

The sum is also normalized by the number of energy bins (N) in order to make d independent of N . Usually, the calculated values differ significantly from the measured dose-depth dataset unless the guess spectrum happens to be very close to the true spectrum and hence the initial value of d is large.

To minimize the percent difference between the calculated and measured dose-depth datasets, the relative intensity of x-rays in each energy bin of the spectrum is perturbed (one bin at a time) and tested to determine whether the perturbed spectrum produces a dose-depth dataset closer to the measured dose-depth dataset. The amount of perturbation applied in the relative intensity of x-rays (s_j^ν) in an energy bin with average photon energy of E_j in the ν^{th} iteration is determined according to the following equation [37]:

$$s_j^\nu \rightarrow s_j^{\nu\pm} = s_j^\nu \pm \frac{1}{2^k} s_j^\nu, \quad (5.6)$$

where k is an integer. A positive (negative) perturbation applied to s_j^ν for $k = 1$ increases (decreases) the initial value by 50%. Similarly a positive (negative) perturbation applied to s_j^ν for $k = 2$ increases (decreases) the initial value by 25%, and so on.

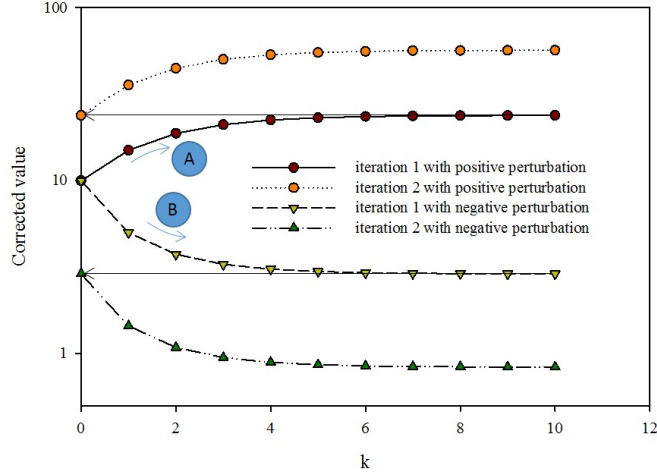


Figure 5.4: Illustration of the effect of an iterative perturbation applied to a number, 10, according to equation (5.6).

Figure 5.4 shows an effect of a positive perturbation applied to an arbitrary value of $s_j^\nu = 10$ recursively using equation (5.6) with $k = 1, 2, \dots, 10$. The first iteration performed with $k = 1$ to $k = 10$ changes the initial value of 10 to 23.8. The second iteration performed starting with 23.8 for the same values of k converges it to 56.7, and so on. Similarly, if a negative perturbation is applied to 10 recursively using equation (5.6) with $k = 1, 2, \dots, 10$, it would converge to some smaller number following path “B”.

Figure 5.5 shows the main steps of calculation in which the relative intensity of x-rays (s_j^ν) in each of the energy bin with average energy (E_j) of the spectrum $S^\nu(N)$ is tested by giving a positive perturbation and a negative perturbation. It represents the calculation inside the Box 1 of the block diagram shown in Figure 5.2.

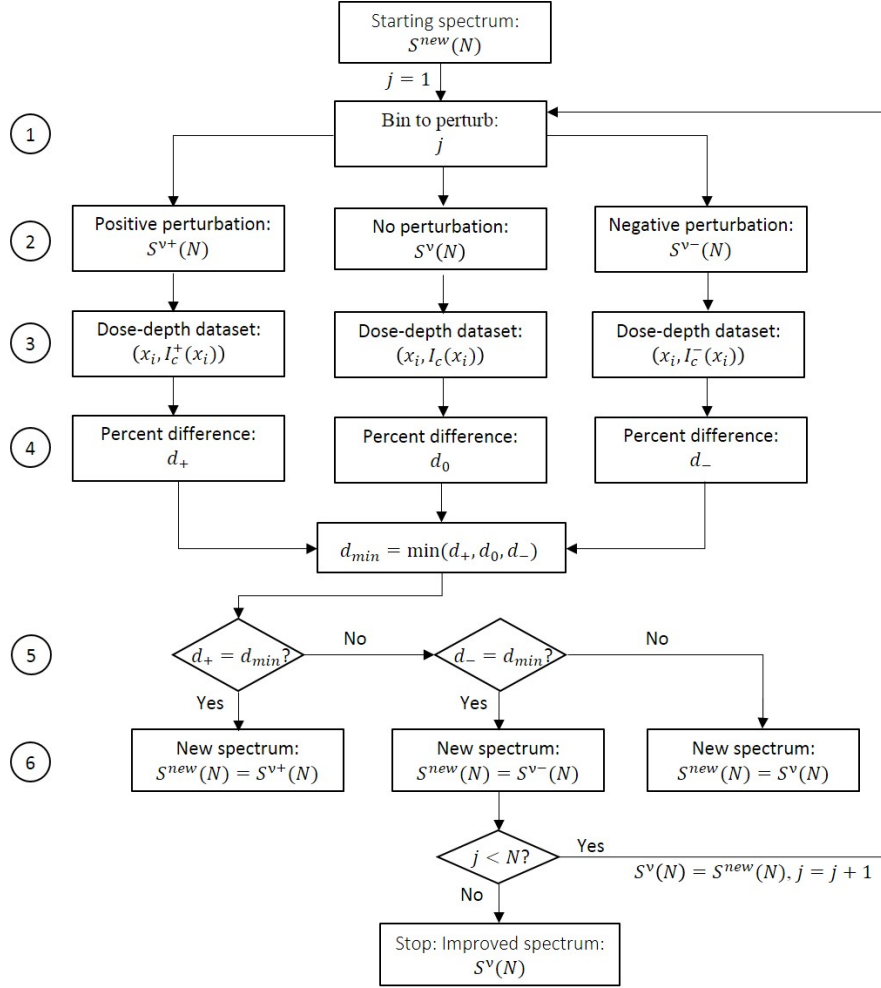


Figure 5.5: Block diagram showing the calculation in one iterative cycle shown in Box 1 of the block diagram in Figure 5.2.

If the new spectrum ($S^{new}(N)$) obtained by changing the relative intensity in an energy bin, either with a positive or a negative perturbation, produces the calculated dose-depth dataset closer to the measured dose-depth dataset, then the spectrum $S^v(N)$ is updated to $S^{new}(N)$ for the next step calculation. Otherwise, the spectrum $S^v(N)$ will be kept unchanged for the calculation in the following energy bin.

Initially, the intensity of x-rays in only the first energy bin of the spectrum $S^v(N)$ is increased by 50% of its initial value, as shown in the row (2) of the block diagram in Figure 5.5, i.e.

$$s_1^v \rightarrow s_1^{v+} = s_1^v + \frac{1}{2}s_1^v, \quad (5.7)$$

so that the spectrum $S^\nu(N)$ is changed to a different spectrum $S^{\nu+}(N)$ which has the following form:

E_1	E_2	\dots	E_j	\dots	E_{N-1}	E_N
$s_1^{\nu+}$	$s_2^{\nu+}$	\dots	$s_j^{\nu+}$	\dots	$s_{N-1}^{\nu+}$	$s_N^{\nu+}$

where the relative intensity of x-rays $s_j^{\nu+}$, in each energy bin with average x-ray energy E_j , is given by

$$s_j^{\nu+} = \begin{cases} s_1^\nu + \frac{1}{2}s_1^\nu, & \text{for } j = 1 \\ s_j^\nu, & \text{for } j = 2, 3, \dots, N. \end{cases}$$

The superscript “+” in $S^{\nu+}(N)$ represents a positive perturbation applied to the relative intensity of x-rays in one energy bin of the spectrum $S^\nu(N)$.

The intensity of x-rays in the first energy bin of the spectrum $S^\nu(N)$ (unperturbed) is decreased by 50% of its initial value, i.e.

$$s_1^\nu \rightarrow s_1^{\nu-} = s_1^\nu - \frac{1}{2}s_1^\nu, \quad (5.8)$$

so that the spectrum $S^\nu(N)$ is changed to a different spectrum $S^{\nu-}(N)$ which has the following form:

E_1	E_2	\dots	E_j	\dots	E_{N-1}	E_N
$s_1^{\nu-}$	$s_2^{\nu-}$	\dots	$s_j^{\nu-}$	\dots	$s_{N-1}^{\nu-}$	$s_N^{\nu-}$

where the relative intensity of x-rays $s_j^{\nu-}$, in each energy bin with average x-ray energy E_j , is given by

$$s_j^{\nu-} = \begin{cases} s_1^\nu - \frac{1}{2}s_1^\nu, & \text{for } j = 1 \\ s_j^\nu, & \text{for } j = 2, 3, \dots, N. \end{cases}$$

The superscript “-” in $S^{\nu-}(N)$ represents a negative perturbation applied to the relative intensity of x-rays in one energy bin of the spectrum $S^{\nu}(N)$.

In the next step, shown in row (3) of Figure 5.5, the exposure $I_c^{\nu+}(x_i)$ due to the beam attenuated by an absorber of each thickness x_i is calculated using the positively perturbed energy spectrum ($S^{\nu+}(N)$):

$$I_c^{\nu+}(x_i) = \sum_{j=1}^N s_j^{\nu+} e^{-\mu(E_j)x_i}, i = 1, 2, \dots, N. \quad (5.9)$$

The calculation in equation (5.9) yields a calculated dose-depth dataset $(x_i, I_c^{\nu+}(x_i))$.

The exposure $I_c^{\nu}(x_i)$ due to the beam attenuated by an absorber of each thickness x_i is calculated using the unperturbed energy spectrum ($S^{\nu}(N)$):

$$I_c^{\nu}(x_i) = \sum_{j=1}^N s_j^{\nu} e^{-\mu(E_j)x_i}, i = 1, 2, \dots, N. \quad (5.10)$$

The calculation in equation (5.4) yields a calculated dose-depth dataset $(x_i, I_c^{\nu}(x_i))$.

Similarly, the exposure $I_c^{\nu-}(x_i)$ due to the beam attenuated by an absorber of each thickness x_i is calculated using the negatively perturbed energy spectrum ($S^{\nu-}(N)$):

$$I_c^{\nu-}(x_i) = \sum_{j=1}^N s_j^{\nu-} e^{-\mu(E_j)x_i}, i = 1, 2, \dots, N. \quad (5.11)$$

The calculation in equation (5.11) yields a calculated dose-depth dataset $(x_i, I_c^{\nu-}(x_i))$.

As shown in the row (4) of the block diagram, the total percent difference between the calculated dose-depth dataset $(x_i, I_c^{\nu+}(x_i))$ and the measured dose-depth dataset $(x_i, I(x_i))$ is calculated:

$$d_+ = \frac{1}{N} \sum_{i=1}^N \left| \frac{I_c^{\nu+}(x_i) - I(x_i)}{I(x_i)} \right| \times 100\% \quad (5.12)$$

where the suffix “+” in d_+ represents the calculation with the dose-depth dataset calculated using the “positively” perturbed spectrum.

The total percent difference d_0 , between the calculated dose-depth dataset from equation (5.10), $(x_i, I_c(x_i))$, and the measured dose-depth dataset, $(x_i, I(x_i))$, is calculated:

$$d_0 = \frac{1}{N} \sum_{i=1}^N \left| \frac{I_c^\nu(x_i) - I(x_i)}{I(x_i)} \right| \times 100\% \quad (5.13)$$

where the suffix “0” in d_0 represents the calculation with the dose-depth dataset calculated using the “unperturbed” spectrum.

Similarly, the total percent difference between the calculated dose-depth dataset $(x_i, I_c^{\nu-}(x_i))$ and the measured dose-depth dataset $(x_i, I(x_i))$ is also calculated:

$$d_- = \frac{1}{N} \sum_{i=1}^N \left| \frac{I_c^{\nu-}(x_i) - I(x_i)}{I(x_i)} \right| \times 100\% \quad (5.14)$$

where the suffix “-” in d_- represents the calculation with the dose-depth dataset calculated using the “negatively” perturbed spectrum.

The values of d_+ , d_0 , and d_- calculated in equations (5.12), (5.13), and (5.14) respectively are different from each other as each of them is calculated from a differently perturbed energy spectrum. For the next step calculation, the energy spectrum $S^\nu(N)$ is either (i) updated to $S^{\nu+}(N)$ if d_+ is minimum, (ii) updated to $S^{\nu-}(N)$ if d_- is minimum, or (iii) unchanged, as shown in the rows (5) and (6) of Figure 5.5.

The calculation is repeated in the same way for each of the remaining energy bins (i.e. $j = 2, 3, \dots, N$). The perturbation applied to the intensity of x-rays in each energy bin of the spectrum $S^\nu(N)$ in this calculation loop is given by $s_j^\nu \rightarrow s_j^{\nu\pm} = s_j^\nu \pm \frac{1}{2}s_j^\nu$. This is equivalent to the calculation in “Box 1” of the block

diagram in Figure 5.2 with $k = 1$ in the generic expression of the perturbation equation, $s_j^\nu \rightarrow s_j^{\nu\pm} = s_j^\nu \pm \frac{1}{2^k} s_j^\nu$. The relative intensity of x-rays in each energy bin of the spectrum obtained at the end of the first calculation loop is either increased by 50%, decreased by 50%, or unchanged from the corresponding value in the starting spectrum.

The calculation in “Box 1”, of the block diagram shown in Figure 5.2 is repeated with $k = 2$ in the same way as described by the block diagram in Figure 5.5. In this loop of calculation, the relative intensity of x-rays in each energy bin is either increased by 25%, decreased by 25%, or unchanged from its value in the spectrum obtained from the previous calculation loop (with $k = 1$). In a similar way, the whole calculation shown in “Box 1” of Figure 5.2 is repeated with $k = 3, 4, \dots, 10$.

The calculation performed with $k = 1, 2, \dots, 10$, shown in Box 2 in Figure 5.2, represents one iteration cycle. The percent difference scored at the end of an iteration cycle is compared with that scored at the end of previous iteration cycle. The calculation is terminated when the percent difference between the calculated and the measured dose-depth datasets stops decreasing further, i.e. when $d_\nu - d_{\nu-1} = 0$, where d_ν is the percent difference at the end of ν^{th} iteration. Once this condition is met, the energy spectrum does not significantly improve any further.

Figure 5.6(left) shows an energy spectrum of a 6 MVp x-ray beam obtained by performing 38 iterations according to the procedures described above. In this calculation, the guess spectrum is shown in Figure 5.3 and used the dose-depth dataset measured with aluminum absorbers from Table 7.2. For iterations after the 38th, the spectrum no longer changed shape. The dose-depth dataset calculated using this spectrum agrees well with the measured dataset, as shown in Figure 5.6(right). The total percent difference between the calculated and the measured dose-depth datasets was found to be 0.08%.

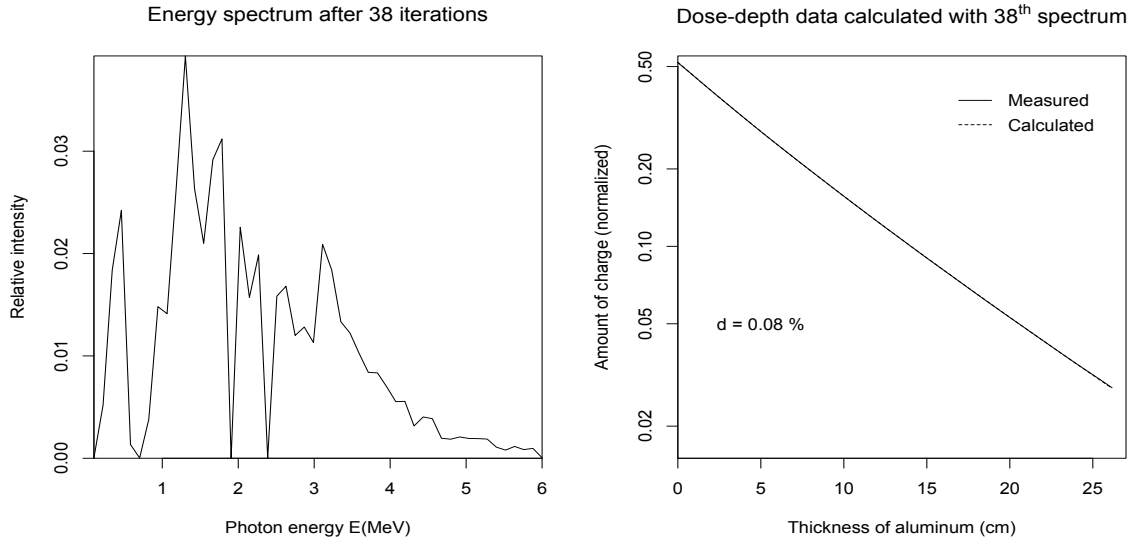


Figure 5.6: 6 MVp X-ray energy spectrum obtained at the end of 38th iteration. A comparison between the measured and calculated dose-depth datasets is shown on the right.

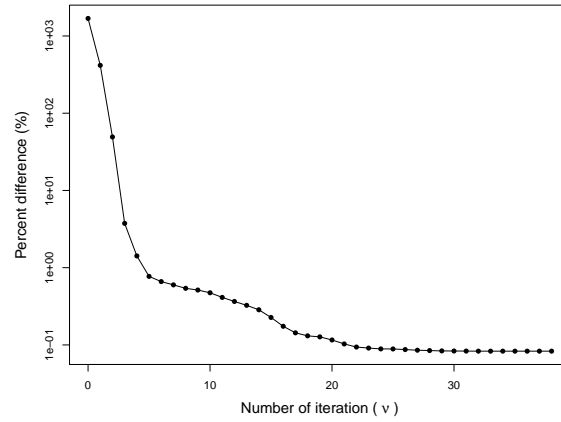


Figure 5.7: Plot showing the total percent difference between the calculated and the measured dose-depth datasets as a function of the number of iterations performed. In this example, the percent difference was found to stop decreasing beyond 38th iteration.

Figure 5.7 shows a plot of the total percent difference between the calculated and measured dose-depth datasets as a function of the number of iterations performed. The total percent difference corresponding to $\nu = 0$, 1686.51%, indicates the value calculated with the guess spectrum. The total percent difference reduces to

416.43% after performing the first iteration, then to 49.28% after the second iteration, and so on. The percent difference first decreases rapidly in the first few iterations and then decreases by a progressively smaller factor because of only subtle changes in the spectral shape following the first few iterations.

Chapter 6

Smoothing x-ray energy spectra

Although the energy spectrum of an x-ray beam estimated by the algorithm described above yields a dose-depth dataset which agrees well with the measured dose-depth dataset, the shape of the spectrum is not physically acceptable since it contains a number of unrealistic peaks and valleys in it that is proportional to the number of energy bins considered in the calculation, but which are in no way justified by our physical understanding of the problem. In other words, these peaks and valleys are artifacts of the iterative algorithm.

These peaks cannot correspond to characteristic x-rays since the characteristic x-rays produced by the electron targets commonly used in clinical linacs all have energies smaller than 100 keV, well below the energies where these peaks occur. At energies above 100 keV, primary x-rays in therapeutic x-ray beams are the result of bremsstrahlung and, as described in Chapter 4, we expect the bremsstrahlung spectrum to have a smooth continuous shape and possess only one peak and no valleys.

Unless the electron target has highly complex structure and/or is composed of different types of elements, the energy spectrum of the bremsstrahlung x-rays produced by a linac should not have peaks and valleys. Although, it is nearly impossible to get the information regarding the composition and the thickness of the electron target used inside a linac from the linac manufacturers, an electron target in a linac is designed to meet two main criteria: (i) the x-ray yield in the forward direction should

be large and (ii) the x-ray beam produced by the target should have sufficiently large penetration power or good depth-dose characteristics as required for therapeutic applications [72]. To meet these criteria, an electron target is usually homogeneous in structure and its optimal thickness is chosen to be approximately equal to the mean electron range in the target material so that the target yields x-ray beams that have near optimum depth dose characteristics and a good x-ray yield. [72, 73]

In most of the clinical linacs, a flattening filter is inserted in between the primary collimator and the monitor chamber in order to make the beam intensity laterally uniform across the field at the reference depth. This filter is primarily designed for flattening the forward peaked bremsstrahlung spectrum of the beam and absorbing the low energy x-rays to minimize the skin dose during the treatment. The flattening filter, used with a specific nominal energy of an x-ray beam, is usually made of lead or tungsten of appropriate thickness and is conical in shape so that it can differentially absorb the radiation towards the beam center. Because of its homogeneous structure, it should not produce an x-ray energy spectrum with multiple peaks and valleys. [74, 75]

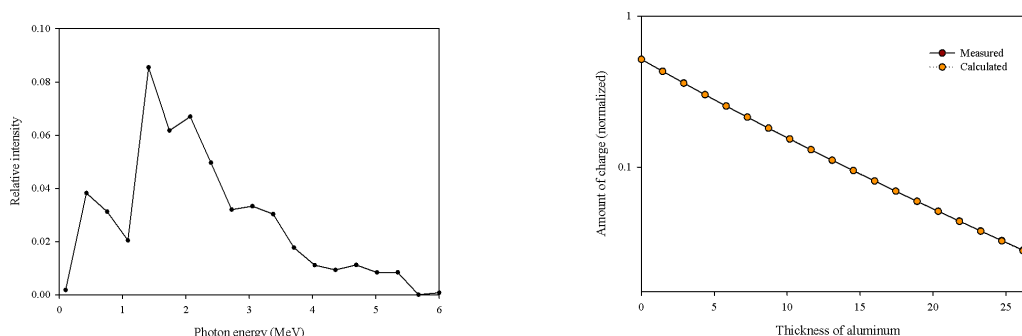


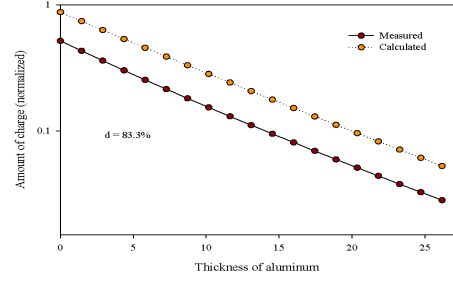
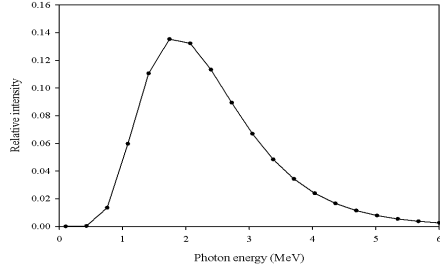
Figure 6.1: The energy spectrum (left) of a 6 MVp x-ray beam estimated using the dose-depth dataset measured using aluminum absorbers. On the right is a comparison between the dose-depth dataset calculated using the estimated spectrum and the measured dose-depth dataset.

Figure 6.1 (left) shows an estimated energy spectrum of a 6 MVp x-ray beam based on the measured dose-depth data with aluminum absorbers, from Table

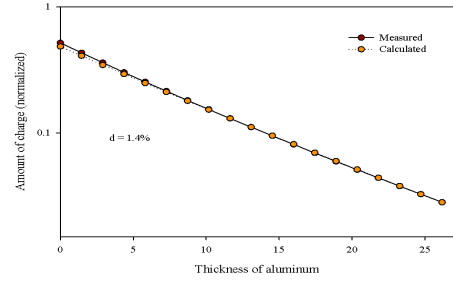
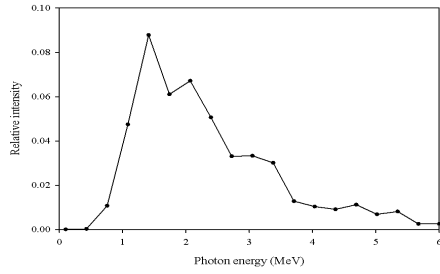
7.2. A guess spectrum with photon energy ranging from 0.1 to 6 MeV and containing 19 equally spaced energy bins was defined using the log normal distribution given by equation (5.3). The standard deviation (σ) of $\ln(E_j)$ was modified to $\sigma/2.5$ to get the peak of the guess spectrum at approximately $1/3^{\text{rd}}$ of the maximum x-ray energy. The number of energy bins was made to be equal to the number of data points in the measured dose-depth dataset in order to minimize the number of peaks and valleys in the estimated spectrum. A total of 37 iterations were carried out before the energy spectrum converged to stability. The dose-depth dataset calculated using the estimated energy spectrum is compared with the measured dataset in Figure 6.1(right). The total percent difference between the calculated and measured dose-depth datasets was found to be 0.2%. Note that the spectrum consists of unrealistic peaks at energies of 0.4, 1.4, 2.1, 3.1, 4.7, and 5.3 MeV.

To see when the peaks and valleys start to show up and how they evolve with the number of iterations performed, the energy spectra obtained at the end of the first four iterations are plotted in Figure 6.2. A comparison of the dose-depth dataset calculated using each of these spectra with the measured dose-depth dataset is shown in the right side of Figure 6.2. It can be noticed that some peaks and valleys already appear in the energy spectrum by the end of the second iteration ($S^2(19)$). The percent difference between the calculated dose-depth data using the spectrum obtained at the end of the second iteration and the measured dose-depth dataset is only 1.4%. The spectra obtained at the end of the third iteration ($S^3(19)$) and the fourth iteration ($S^4(19)$) are almost same and differ slightly from $S^2(19)$, most notably in the lower energy region. The total percent difference between the calculated and measured dose-depth datasets was reduced to 0.8% and 0.7% after performing third and fourth iterations, respectively.

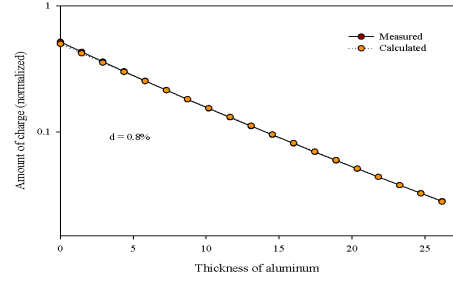
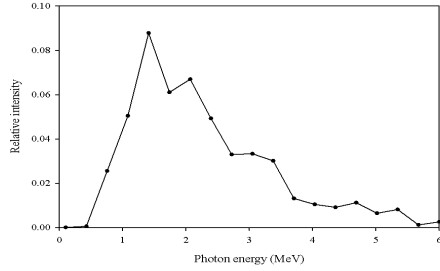
Since the spectrum was found to stop improving after 37 iterations, the



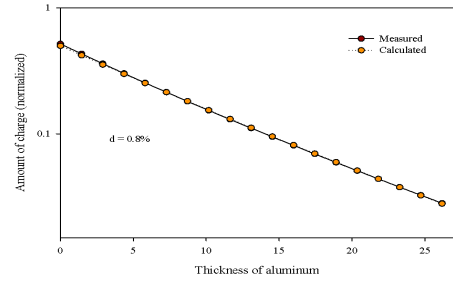
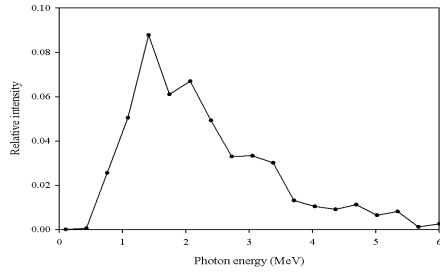
(a) Spectrum after first iteration, $S^1(19)$. (b) Dose-depth data calculated using $S^1(19)$.



(c) Spectrum after second iteration, $S^2(19)$ (d) Dose-depth data calculated using $S^2(19)$.



(e) Spectrum after third iteration, $S^3(19)$. (f) Dose-depth data calculated using $S^3(19)$.



(g) Spectrum after fourth iteration, $S^4(19)$. (h) Dose-depth data calculated using $S^4(19)$.

Figure 6.2: Energy spectra of a 6 MVp x-ray beam obtained at the end of the first four iterations. The dose-depth dataset calculated using each of the spectra on the left is compared with the measured dose-depth dataset and shown in the right side.

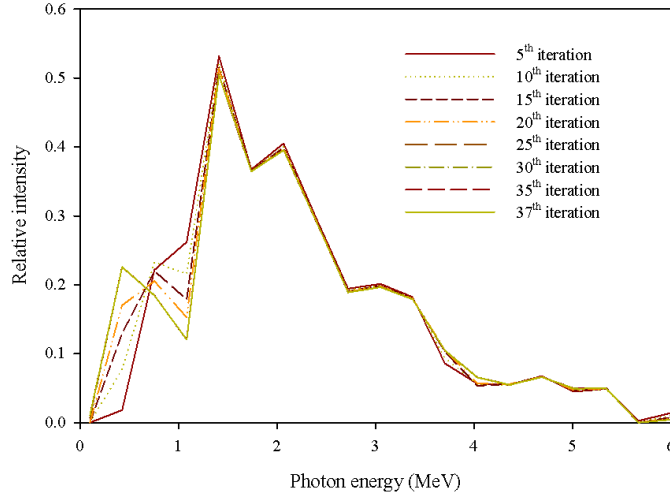


Figure 6.3: The energy spectrum of a 6 MVp x-ray beam obtained at the end of the first 5, 10, 15, 20, 25, 30, 35, and 37 iterations.

spectra obtained at the end of the 5th, 10th, 15th, 20th, 30th, 35th, and 37th iterations were also considered and these are compared with each other in Figure 6.3. All the spectra were normalized to the same area under the curve. It can be noticed from Figure 6.3 that by performing more number of iterations the shape of the spectrum does not change in the higher energy region, but changes slightly only in the lower energy region. Beyond 25th iteration, the total percent difference between the measured and the calculated dose-depth datasets was found to decrease beyond the 5th digit after decimal. By performing more iterations, there was only a slight increment in the relative intensity of lower energy x-rays, whereas the spectral shape was nearly constant in the higher energy region.

The dose-depth data used to estimate the energy spectrum of a 6 MVp x-ray beam was measured in linac with the flattening filter in place. Without knowing the exact details of the flattening filter design, it is difficult to estimate the amount of absorption of lower energy x-rays. However, the increase in the relative intensity of lower energy x-rays by performing additional iterations, especially without any significant improvement in the agreement of the calculated dose-depth data with the

measured data, has no physical justification.

6.1 Implementation of a polynomial fit for smoothing x-ray energy spectrum

The peaks and valleys observed in the calculated spectrum are artifacts of the algorithm introduced by discrete energy bins. In a physically acceptable solution, the spectrum should be continuous, smooth and contain only a single peak and no valleys, and should have a shape similar to that of the guess spectrum. One way to obtain a spectrum having these properties is to smooth the calculated x-ray energy spectrum produced by the iterative perturbation method described above. For the purpose of smoothing the energy spectra, a number of smoothing algorithms including the moving average/median method, spline smoothing, loess local regression, mixed-estimation method, multiple imputation, and double sampling for regression were considered. None of them was found to smooth a spectrum globally and produce a smooth spectrum having properties of the spectral shape of therapeutic x-ray beam described above.

The fitting of a straight line can be considered the most extreme form of smoothing. However, since the linear shape of the energy spectrum of an x-ray beam produced by a thick electron target is significantly changed due to inherent filtration of the beam the actual energy spectrum cannot be represented by a linear equation. A polynomial of degree 2 or more involves more fitting parameters than a straight line and a polynomial of degree 3 or greater was found to remove the unrealistic peaks and valleys in the calculated spectrum. By fitting a spectrum containing peaks and valleys with a polynomial, we not only get rid of peaks and valleys, but also get the simplest

single function representing the energy spectrum of an x-ray beam with theoretically infinite energy resolution. The smooth spectrum was found to meet all the criteria of a physically accepted spectral shape of an x-ray beam produced by a therapeutic linac. As will be shown below, this polynomial fit of the calculated x-ray energy spectrum was found to yield a calculated dose-depth dataset that possesses the same level of positive agreement with the measured dose-depth dataset as that found for the unsmoothed energy spectrum from the iterative perturbation method.

Mathematically, a polynomial of degree q has the following form:

$$I_0(E) = \sum_{r=0}^q A_r E^r, \quad (6.1)$$

where $I_0(E)$ is the relative intensity of primary x-rays with energy E , q is the degree of polynomial, and $A_r (r = 0, 1, 2, \dots, q)$ are the constants whose values are determined by minimizing the residual,

$$R^2 = \sum_{i=1}^N \left(s_j^\nu(E_i) - I_0(E_i) \right)^2 = \sum_{i=1}^N \left(s_j^\nu(E_i) - \sum_{r=0}^q A_r E_i^r \right)^2. \quad (6.2)$$

In equation 6.2, $s_j^\nu(E_i)$ is the relative intensity of x-rays with energy in the estimated energy spectrum obtained by performing ν iterations and N is the number of energy bins in the spectrum.

The degree of polynomial (q) is always chosen to be as small as possible such that (i) the polynomial fits the calculated spectrum with a good R^2 value and (ii) the shape of the energy spectrum represented by the polynomial agrees with the expected spectral shape of an x-ray beam. After finding the constants A_r , from equation 6.2, the intensity of x-rays in each energy bin is estimated and the final spectrum has the following form:

E_1	E_2	...	E_j	...	E_{N-1}	E_N
$I_0(E_1)$	$I_0(E_2)$...	$I_0(E_j)$...	$I_0(E_{N-1})$	$I_0(E_N)$

where the relative intensity of x-rays $I_0(E_j)$, in each energy bin with average x-ray energy E_j , is given by equation 6.1.

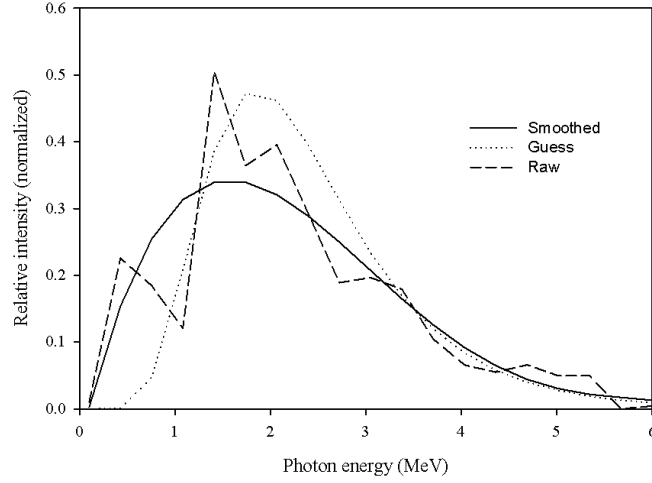


Figure 6.4: The energy spectrum of a 6 MVp x-ray beam (dashed line), estimated by using the iterative perturbation method, is smoothed by fitting the spectrum with a polynomial of degree 4. The energy spectrum represented by the fitted polynomial (solid line) is compared with the guess spectrum (dotted line). The area under each curve is made to be 1.

Figure 6.4 shows the energy spectrum from Figure 6.1(dashed line) after having been fit with a polynomial (solid line). It also shows the guess spectrum which was used in the calculation (dotted line). For comparison, the area under each curve was normalized to 1. In this example, the calculated energy spectrum containing peaks and valleys was fitted with a polynomial of degree 4:

$$I_0(E) = -9.34 \times 10^{-3} + 1.03 \times 10^{-2}E - 5.05 \times 10^{-2}E^2 + 8.51 \times 10^{-3}E^3 - 4.85 \times 10^{-4}E^4.$$

We can see that the spectrum after smoothing with a polynomial has only a single peak

and valleys. The relative intensity of x-rays first increases with a steep positive slope, reaches a maximum at the photon energy of ~ 1.4 - 1.8 MeV and then falls asymptotically to approximately zero at the maximum photon energy as expected.

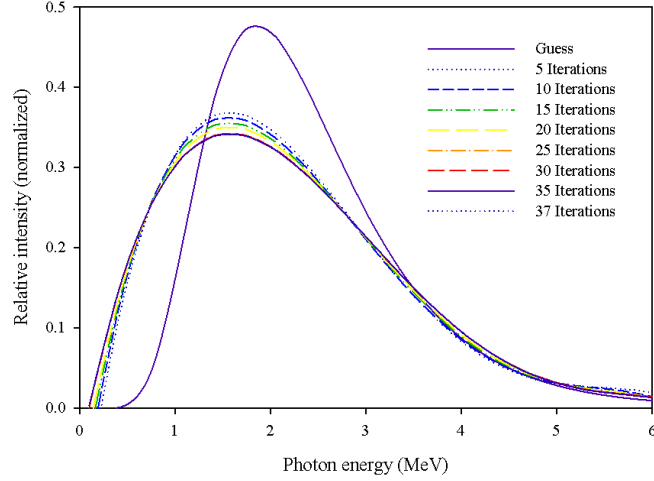


Figure 6.5: A comparison between all the spectra shown in Figure 6.3 after smoothing, by fitting a polynomial of 4th degree in each spectrum. The guess spectrum used in the calculation is also shown in the graph. Each spectrum is normalized in such a way that the area under the curve is 1.

Table 6.1: Coefficients of polynomials, A_r , $r = 0, 1, \dots, 4$, used to fit the spectra showing in Figure 6.3.

No. of itera- tions	A_4	A_3	A_2	A_1	A_0
5	-7.35×10^{-4}	1.22×10^{-2}	-6.91×10^{-2}	1.38×10^{-1}	-2.69×10^{-2}
10	-6.59×10^{-4}	1.12×10^{-2}	-6.42×10^{-2}	1.29×10^{-1}	-2.18×10^{-2}
15	-6.26×10^{-4}	1.06×10^{-2}	-6.05×10^{-2}	1.21×10^{-1}	-1.81×10^{-2}
20	-5.75×10^{-4}	9.82×10^{-3}	-5.69×10^{-2}	1.15×10^{-1}	-1.50×10^{-2}
25	-4.93×10^{-4}	8.63×10^{-3}	-5.10×10^{-2}	1.04×10^{-1}	-9.92×10^{-3}
30	-4.85×10^{-4}	8.51×10^{-3}	-5.05×10^{-2}	1.03×10^{-1}	-9.35×10^{-3}
35	-4.85×10^{-4}	8.51×10^{-3}	-5.05×10^{-2}	1.03×10^{-1}	-9.35×10^{-3}
37	-4.85×10^{-4}	8.51×10^{-3}	-5.05×10^{-2}	1.03×10^{-1}	-9.34×10^{-3}

Figure 6.5 shows a comparison of the calculated energy spectra from Figure 6.3, after smoothing with polynomials of degree 4, and the guess spectrum used in the calculation. Each spectrum was normalized such that the area under the spectrum is

equal to 1. Table 6.1 presents the coefficients of the polynomials (before normalization) that were found by minimizing the residual defined by equation 6.2. The peak of the spectrum does not shift with the number of iterations performed.

Chapter 7

Description of Equipment and Methods

7.1 Equipment

7.1.1 Linear Accelerator

A linear accelerator (linac) manufactured by Elekta (Model: Versa HDTM and Serial Number: 3858), made available by Oklahoma Cancer Specialists and Research Institute (OCSRI), Tulsa OK, was used in the measurement of dose-depth datasets. The Versa HD can deliver flattened x-ray beams and flattening filter-free (FFF) x-ray beams, as well as electron beams. Measured datasets were obtained for five different x-ray beams with the nominal energies of 6 MVp, 6 MVp FFF, 10 MVp, 10 MVp FFF, and 18 MVp. The flattening filter free beams have the same penetrating power as the equivalent energy of flattening filter beams but such beams have a reduced scattering, simplified beam modeling, and high dose rate.

The Versa HD linac utilizes a 160 leaf multi-leaf collimating system, which allows for precision shaping of the beam to the treatment area. The maximum field size of the beam that can be obtained from Versa HD is $40 \times 40 \text{ cm}^2$. The field size is controlled by a pair of sculpted diaphragms mounted orthogonal to the multi-leaf

collimator (MLC). While measuring dose-depth datasets with each beam, a field size of $10 \times 10 \text{ cm}^2$ at a distance of 100 cm from the source was used.

7.1.2 Detectors

Two identical pinpoint ionization chambers each of model number (TN) 31014, manufactured by PTW-Freiburg (Freiburg, Germany), were used as detectors to measure dose-depth datasets. One PTW TN-31014 ionization chamber with the serial number 000959 was placed in front of the absorbers and was used to monitor the beam by measuring the exposure in air before the beam gets attenuated through absorbers. This first ionization chamber was placed at a fixed distance of 147.0 cm from the source and slightly off axis, at a radial distance of 2.0 cm. The second PTW TN-31014 ionization chamber with the serial number 000958 was placed on the beam's axis at a fixed distance of 200 cm from the source and was used to measure the exposure in air of the beam following attenuation by absorbers of various thicknesses.



Figure 7.1: PTW TN31014 ionization chamber.

Figure 7.1 shows a diagram of the PTW TN-31014 ionization chamber. The PTW TN-31014 ionization chamber is a commercial ionization chamber that is used in absolute dosimetry on x-ray beams with nominal energies between Co-60 and 50 MVp.

This ionization chamber is suitable for the measurement of absorbed dose in small-sized x-ray beams and for relative dosimetry such as output factors, depth dose curves, and beam profiles. It has a vented cylindrical chamber with a radiation sensitive region 1 mm radius and a length of 5 mm. The volume is 0.015 cc and a reference point on the chamber axis is located at 3.4 mm from the chamber tip. The wall material of the ionization chamber is graphite with a protective acrylic (Polymethyl methacrylate or PMMA) buildup cap. The wall thickness of the buildup cap is 3 mm. The reference conditions at which this ionization chamber has 100% ion collection efficiency are (i) beam quality Co-60, (ii) temperature of 22°C, (iii) a pressure of 1013.2 hPa, (iv) biasing voltage of ± 400 V, and (v) a relative humidity of 50%. In order to achieve charged particle equilibrium in the chamber cavity, the buildup cap was used in each ionization chamber throughout the measurement.

7.1.3 Electrometer

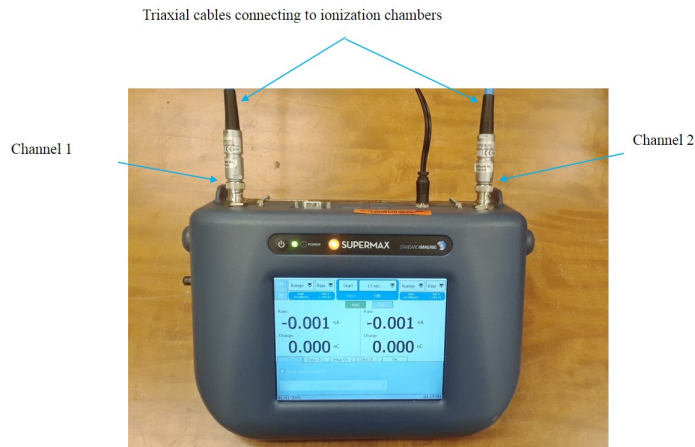


Figure 7.2: Photo of a SuperMAX electrometer.

A SuperMAX Electrometer manufactured by Standard Imaging, Inc., USA was used to record the amount of charge collected inside the radiation sensitive volume of each of the ionization chambers. Figure 7.2 shows an image of this electrometer. It

consists of two independent measurement channels each of which can display (i) charge ranging from 0.001 pC to 999.9 μ C (1 fC resolution) in the low range mode and from 0.001 nC to 999.9 μ C (1 pC resolution) in the high range mode and (ii) current ranging from 0.001 pA to 500.0 pA (1 fA resolution) in the low range mode and from 0.001 nA to 500.0 nA (1 pA resolution) in the high range mode. The SuperMAX electrometer can also provide a detector biasing voltage ranging from ± 100 to ± 1000 V (in 1 V increments). A biasing voltage of 400 V to each of the PTW TN-31014 ionization chambers was supplied through the electrometer.

7.1.4 Absorber material

The main criteria for an absorber material to be used for measuring attenuation datasets to estimate the energy spectra of x-ray beams is that the mass attenuation coefficient of the absorber material must decrease monotonically with increasing x-ray energy [37, 76]. In other words, each x-ray energy present in an x-ray beam must have a mass attenuation coefficient with a unique value.

Figure 7.3 shows the plots of the total mass attenuation coefficient as a function of the photon energy for five different materials: water, carbon, aluminum, copper, and lead. It can be noticed that for x-ray photons with energy ranging from few 10 keV to about 20 MeV, the mass attenuation coefficient, for both the low Z and high Z materials, does not meet above mentioned criteria strictly. For example, the mass attenuation coefficient for aluminum first decreases rapidly as the photon energy increases from 10 keV to 100 keV and then it still decreases but with larger slope when the photon energy increases. The mass attenuation coefficient for water and carbon has almost unique values in the selected range of the photon energy, but its values are almost the same at the higher energy end. For copper, the mass attenuation coefficient

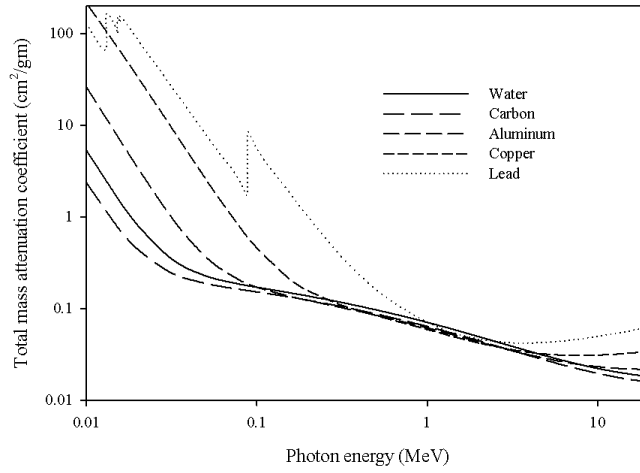


Figure 7.3: Total mass attenuation coefficient with coherent scattering as a function of photon's energy for water, carbon, aluminum, copper, and lead. [47]

has a minimum at about 8 MeV and then it starts to increase slightly with the increase of photon energy. For lead, the mass attenuation coefficient has multiple characteristic absorption peaks in the selected range of photon energy and then has a minimum at about 4 MeV. Based on the plots shown in Figure 7.3, carbon and water can be more suitable absorber materials in comparison to other materials. But, because of their smaller densities, the amount of absorber material required to obtain dose-depth datasets is significantly large and these are not practical for use in the clinical x-ray beams.

In this project, aluminum and copper were used as absorber materials in measuring the dose-depth datasets. Both of these materials have been traditionally used as absorber materials to obtain dose-depth datasets for use in estimating x-ray spectra [6, 7, 22, 24, 36, 37]. Aluminum is also a cheap and commonly available material. Although, copper is comparatively more expensive than aluminum, it is also a commonly available material. Two sets of dose-depth data were measured in each of the therapeutic beams considered in this project, one using aluminum absorbers

and the other using copper absorbers. Attenuation datasets measured with aluminum were used to determine the energy spectra of x-ray beams whereas those measured with copper were used to verify the accuracy of the estimated energy spectra of the corresponding x-ray beams.

7.1.4.1 Amount of absorber material for measuring attenuation datasets

To estimate the amount of absorber material needed in the measurement of each attenuation dataset, an estimated value for the average energy of each x-ray beam was taken into account and half value layer, second value layer, and third value layer were calculated. Using a rule of thumb which states that the average x-ray energy of a beam is approximately one-third of the maximum energy [4], the average energy of 6 MVp, 10 MVp, and 18 MVp were respectively considered to be 2 MeV, 3.33 MeV, and 6 MeV. The half value layer ($x_{1/2}$) is the thickness of absorber required to reduce the initial intensity of x-rays by 50% and is given by

$$x_{1/2} = \frac{\ln(2)}{\mu(E)},$$

where $\mu(E)$ is the mass attenuation coefficient for x-rays with energy E on the absorber. The second value layer ($x_{1/4}$) is the thickness of absorber required to reduce the initial intensity of x-rays by 75% and is given by

$$x_{1/4} = \frac{\ln(4)}{\mu(E)}.$$

Similarly, the third value layer ($x_{1/8}$) is the thickness of absorber required to reduce the initial intensity of x-rays by 87.5% and is given by

$$x_{1/8} = \frac{\ln(8)}{\mu(E)}.$$

Table 7.1: Calculation of the first, second and third value layers for the photons with energies equal to an estimated average energy of three different therapeutic x-ray beams.

Element	Maximum energy (MeV)	Average energy (MeV)	μ (cm ² /g) [47]	$x_{1/2}$ (cm)	$x_{1/4}$ (cm)	$x_{1/8}$ (cm)
Aluminum	6	2	4.32×10^{-2}	5.9	11.9	17.8
	10	3.33	3.37×10^{-2}	7.6	15.2	22.9
	18	6	2.66×10^{-2}	9.7	19.3	29.0
Copper	6	2	4.21×10^{-2}	1.8	3.7	5.5
	10	3.33	3.48×10^{-2}	2.2	4.4	6.7
	18	6	3.11×10^{-2}	2.5	5.0	7.5

Table 7.1 shows calculations of the first, second, and third value layers for 6 MVp, 10 MVp, and 18 MVp x-ray beams. Based on these calculations the maximum thickness of absorbers used in the measurement of dose-depth datasets were 26.2 cm of aluminum and 7.4 cm of copper.

7.1.5 Collimators

In order to minimize the number of secondary x-rays detected behind each absorber thickness, two collimators were designed, built and characterized for use in measuring dose-depth datasets under a narrow beam attenuation geometry. The first collimator, called the primary collimator, was built using four different materials: 10.0 cm of lead, 7.0 cm of tin, 1.5 mm of copper and 1.5 mm of aluminum, assembled in that respective order. The primary collimator had a rectangular aperture at its center with the dimensions of 1.5 cm \times 3.0 cm. The cross-sectional size of the primary collimator was made to be 15.0 cm \times 15.0 cm. The primary collimator was fabricated by the Oklahoma State University (OSU) Physics and Chemistry Instrument Shop. Figure 7.4a shows the primary collimator in its fully assembled form. To improve alignment, all the layers of collimator's materials were placed on an aluminum tray. Two knobs on the aluminum tray were tightened and all the layers were taped together as shown

in Figure 7.4a.

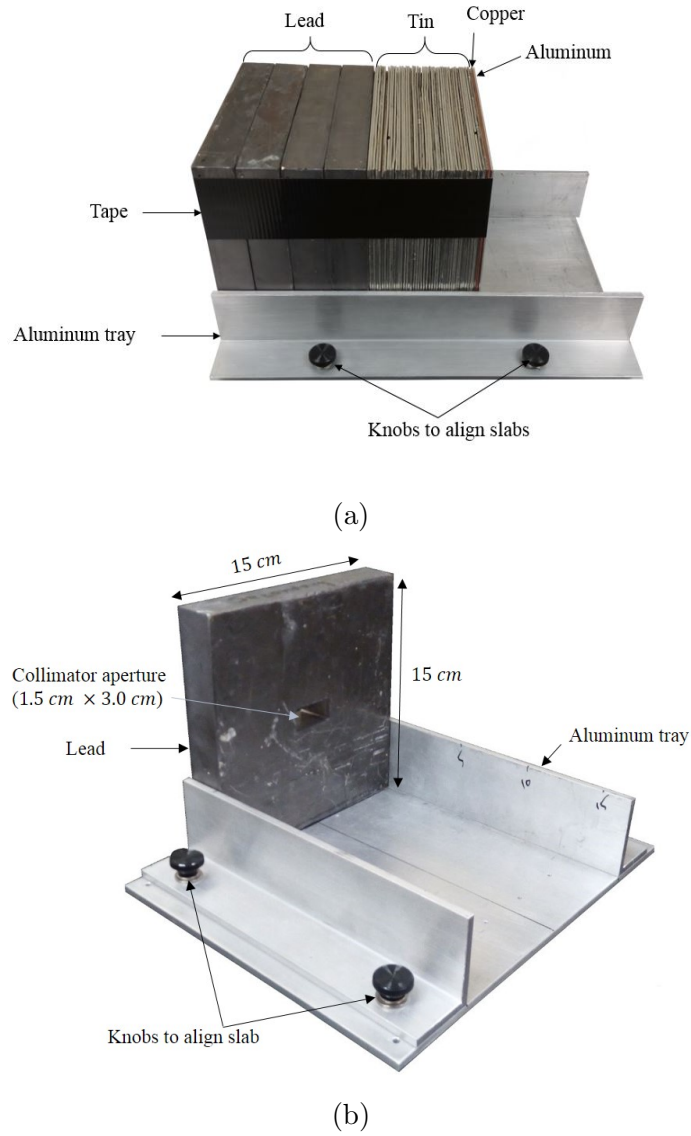


Figure 7.4: (a) Primary collimator in its assembled form. (b) Secondary collimator in its assembled form.

The other collimator, called the secondary collimator, was composed of 2.5 cm of lead and this was also placed on an aluminum tray. The cross-sectional size of the secondary collimator and the dimensions of its aperture were also made to be 15.0 cm \times 15.0 cm and 1.5 cm \times 3.0 cm respectively. This collimator was also fabricated by OSU Physics and Chemistry Instrument Shop. Figure 7.4b shows the secondary

collimator in its assembled form.

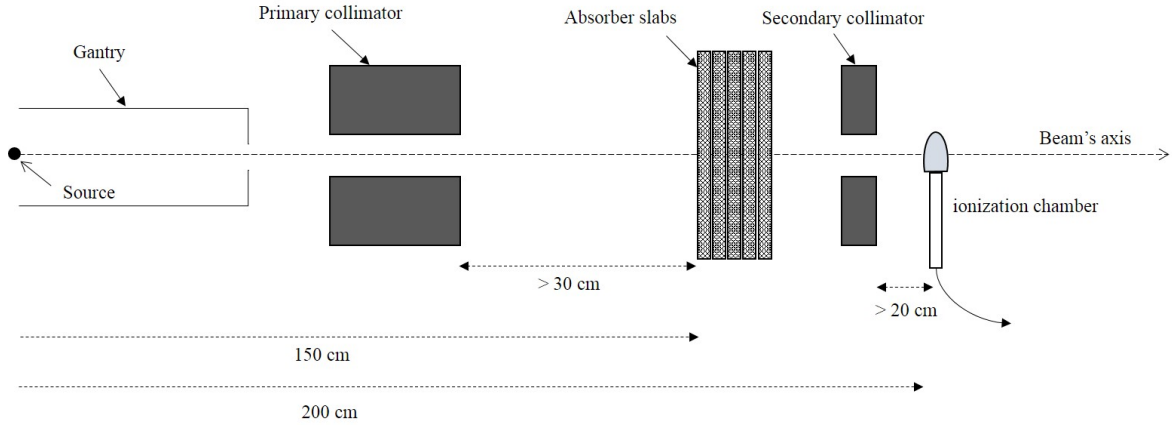


Figure 7.5: A schematic diagram showing a setup for use in measuring attenuation datasets in therapeutic x-ray beams.

The role of the primary collimator, was to (i) reduce the intensity of the scattered (secondary) x-rays from the medium present in between the source and the absorber, (ii) to reduce the field size of the beam into the desired size, (iii) minimize or eliminate intensity of the beam outside the region circumscribed by the collimator, and (iv) minimize the characteristic x-rays produced by the inner surface of the collimator's aperture. Similarly, the main role of the secondary collimator was to minimize the secondaries produced in the primary collimator, the absorber, and in the air.

Both the collimators were tested and studied various features using a setup similar to Figure 7.5. The primary collimator was found to serve its purpose when placed at least 30 cm upstream of the absorbers. Similarly the secondary collimator was found to minimize the secondaries when placed at least 20 cm upstream of the ionization chamber. When measuring dose-depth datasets in this project, the primary collimator was placed at a distance of 70.4 cm upstream of the absorber. The secondary collimator was placed at a distance of 20 cm upstream of the ionization chamber.

7.2 Experimental setup

The gantry of the linac, out of which the x-ray beam emerges, was set at 90° relative to a vertical axis so that the axis of an x-ray beam was horizontal. The primary collimator was placed on the patient couch and the table was moved so that the primary collimator was as close as possible to the gantry. The table and the primary collimator were adjusted in such a way that the axis of the beam passed through the collimator's aperture and the axis was 0.75 cm from each side as shown in Figure 7.6. In that position, the distance from the source to the back surface of the primary collimator was measured to be 79.6 cm.

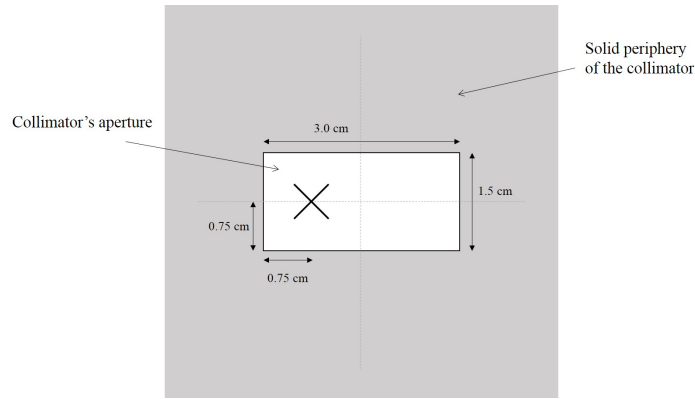


Figure 7.6: Schematic diagram showing the position of the beam's axis in the primary collimator's aperture. The axis of the beam has been denoted by a \times sign.

The secondary collimator was placed so that its aperture was aligned with the aperture of the primary collimator. The alignment was checked with the help of optical distance indicator (ODI) and laser beams available in the treatment room. The distance from the source to the back surface of the secondary collimator was 180 cm.

The PTW TN-31014 ionization chamber with serial number 000958 was placed at a distance of 200 cm from the source. The radiation sensitive area of the ionization chamber was positioned to be on the axis of the beam as shown in Figure

7.7. In that position, the distance between the ionization chamber to the back surface of the secondary collimator was 20 cm.

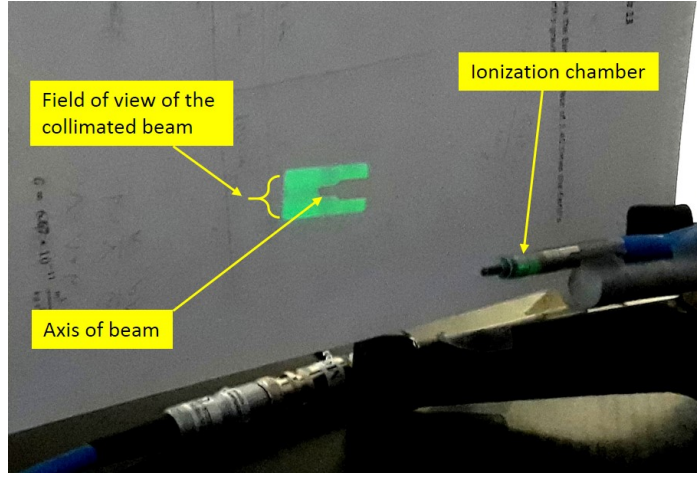


Figure 7.7: Position of the second ionization chamber on the beam's axis and behind the secondary collimator. The buildup cap was taken off while positioning and was put back throughout the measurements.

The PTW TN-31014 ionization chamber with SN-000959, was placed at a distance of 147 cm from the source so that its radiation sensitive area was at a distance of about 2 cm from the beam's axis. Figure 7.8 shows the position of monitoring ionization chamber with respect to the beam axis and the field of view of collimated beam produced by the primary collimator.

The ionization chambers were connected to the two channels of the Super-MAX electrometer via two separate triaxial cables. A biasing voltage of $+400\text{ V}$ was supplied to each ionization chamber via the electrometer. The buildup caps were used on both ionization chambers while taking measurements.

Figure 7.9 shows the final setup for measuring the dose-depth datasets inside treatment room. The absorbers of different thicknesses were placed in between the monitoring ionization chamber and the secondary collimator. While taking the measurements with absorbers, the distance from the source to the front surface of the

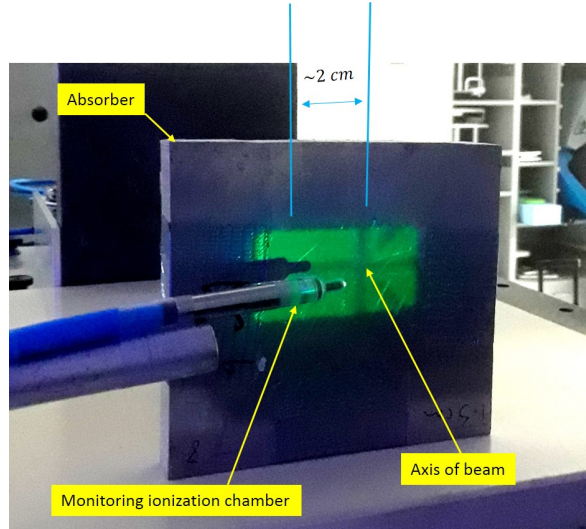


Figure 7.8: Diagram showing the position of the PTW TN-31014 (SN-000958) ionization chamber in front of absorber with respect to the beam's axis. The buildup cap was taken off while positioning and was put back throughout the measurements.

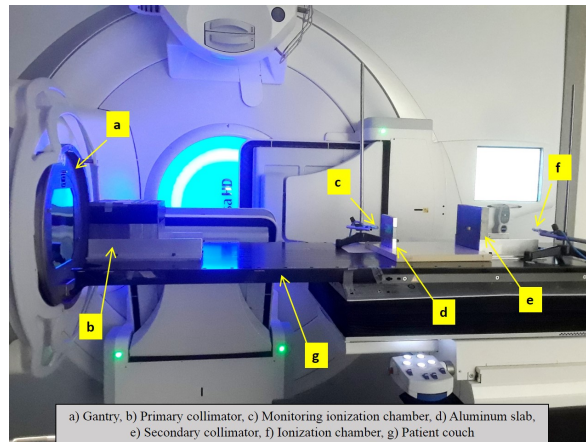


Figure 7.9: Experimental setup for measuring attenuation data in Versa HD linear accelerator.

absorber was always maintained at 150 cm so that the monitoring ionization chamber was always 3 cm from the surface of the absorber.

7.3 Measurement of dose-depth datasets

7.3.1 Aluminum absorbers

Using the experimental setup shown in Figure 7.9, dose-depth data sets were measured using aluminum absorbers of varying thickness. The first data point was measured with a field size of $10 \times 10 \text{ cm}^2$ at a distance of 100 cm from the source in the absence of any absorber. The dose per irradiation was nominally 200 MU and was delivered by the linac in about 24 seconds, at a rate of $\sim 600 \text{ MU/min}$. The amount of charge collected in each ionization chamber was recorded from the electrometer. Then measurements were taken with aluminum absorbers with eighteen different thicknesses from 1.28 cm to 26.16 cm. The field size and dose per irradiation in the measurement with each thickness of the absorbers were kept the same.

Table 7.2 lists the normalized charge collected by the second ionization chamber normalized to the charge of the first ionization chamber as a function of aluminum absorber thickness. In the last two columns of table 7.2, the average and standard deviation of the normalized charges Q_i/Q_{0i} at each thickness of aluminum absorber x_i are presented.

Dose-depth datasets for 6 MVp FFF, 10 MVp, 10 MVp FFF, and 18 MVp x-ray beams were measured in the same way. Table 7.3 presents the dose-depth data measured with aluminum absorbers of varying thickness for the four other x-ray beams.

Table 7.2: Dose-depth dataset measured in 6 MVp beam using aluminum absorbers of various thicknesses.

Thickness of aluminum, x_i (cm)	Reading 2 (Q_1/Q_{01})	Reading 1 (Q_2/Q_{02})	Average (Q/Q_0)	Std. Dev
0	0.5183	0.5171	0.5177	0.0008
1.28	0.4414	0.4415	0.4414	0.0001
2.55	0.3769	0.3769	0.3769	0.0000
3.7	0.3273	0.3274	0.3273	0.0001
4.98	0.2800	0.2804	0.2802	0.0003
6.25	0.2412	0.2412	0.2412	0.0000
7.37	0.2117	0.2117	0.2117	0.0001
8.65	0.1829	0.1827	0.1828	0.0001
9.92	0.1581	0.1580	0.1581	0.0000
11.15	0.1376	0.1377	0.1376	0.0001
12.43	0.1194	0.1193	0.1193	0.0001
13.7	0.1038	0.1039	0.1038	0.0001
14.85	0.0916	0.0914	0.0915	0.0001
16.13	0.0799	0.0798	0.0798	0.0001
17.4	0.0696	0.0696	0.0696	0.0000
18.65	0.0610	0.0609	0.0609	0.0001
21.2	0.0467	0.0468	0.0467	0.0001
24.32	0.0339	0.0339	0.0339	0.0000
26.16	0.0281	0.0282	0.0282	0.0001

Table 7.3: Dose-depth datasets measured in 6 MVp FFF, 10 MVp, 10 MVp FFF, and 18 MVp x-ray beams with aluminum absorbers of various thicknesses.

x (cm)	6 MVp FFF		10 MVp		10 MVp FFF		18 MVp	
	Q/Q_0	SD	Q/Q_0	SD	Q/Q_0	SD	Q/Q_0	SD
0	0.5314	0.0002	0.5047	0.0018	0.5363	0.0006	0.5065	0.0002
1.28	0.4478	0.0002	0.4360	0.0066	0.4592	0.0002	0.4508	0.0010
2.55	0.3781	0.0000	0.3850	0.0003	0.3933	0.0001	0.3999	0.0002
3.7	0.3249	0.0001	0.3398	0.0000	0.3423	0.0004	0.3589	0.0005
4.98	0.2763	0.0001	0.2966	0.0001	0.2945	0.0003	0.3177	0.0000
6.25	0.2363	0.0001	0.2607	0.0004	0.2556	0.0002	0.2835	0.0000
7.37	0.2061	0.0001	0.2322	0.0003	0.2254	0.0001	0.2568	0.0001
8.65	0.1769	0.0000	0.2033	0.0001	0.1958	0.0002	0.2280	0.0002
9.92	0.1524	0.0001	0.1789	0.0001	0.1710	0.0001	0.2041	0.0000
11.15	0.1319	0.0001	0.1584	0.0001	0.1500	0.0000	0.1831	0.0003
12.43	0.1141	0.0001	0.1390	0.0004	0.1312	0.0001	0.1634	0.0002
13.7	0.0989	0.0001	0.1231	0.0001	0.1153	0.0000	0.1464	0.0002
14.85	0.0869	0.0001	0.1100	0.0001	0.1026	0.0001	0.1329	0.0001
16.13	0.0757	0.0000	0.0974	0.0000	0.0903	0.0002	0.1192	0.0001
17.4	0.0661	0.0001	0.0862	0.0001	0.0798	0.0000	0.1072	0.0001
18.65	0.0576	0.0000	0.0764	0.0001	0.0706	0.0000	0.0963	0.0001
21.2	0.0441	0.0000	0.0601	0.0000	0.0554	0.0000	0.0781	0.0001
24.32	0.0321	0.0000	0.0451	0.0000	0.0415	0.0001	0.0607	0.0001
26.16	0.0267	0.0000	0.0383	0.0001	0.0352	0.0001	0.0524	0.0001

7.3.2 Copper absorbers

Table 7.4: Dose-depth datasets measured with copper absorbers in five different beams from Elekta Versa-HD linac using copper absorbers.

Thickness of copper, x (cm)	6 MVp			6 MVp FFF			10 MVp			10 MVp FFF			18 MVp		
	Q/Q_0	SD	Q/Q_0	Q/Q_0	SD	SD	Q/Q_0	SD	SD	Q/Q_0	SD	SD	Q/Q_0	SD	SD
0.00	0.5211	0.0000	0.5355	0.0000	0.0000	0.0000	0.5087	0.0000	0.0000	0.5408	0.0000	0.0000	0.5104	0.0000	0.0000
0.17	0.4848	0.0008	0.4946	0.0001	0.0001	0.0006	0.4767	0.0006	0.0004	0.5025	0.0004	0.0004	0.4798	0.0003	0.0003
0.32	0.4560	0.0002	0.4622	0.0000	0.0000	0.0004	0.4504	0.0004	0.0003	0.4714	0.0003	0.0003	0.4550	0.0000	0.0000
0.64	0.3976	0.0004	0.3997	0.0001	0.0001	0.0010	0.3994	0.0010	0.0003	0.4112	0.0003	0.0003	0.4054	0.0000	0.0000
0.96	0.3486	0.0000	0.3481	0.0001	0.0001	0.0002	0.3547	0.0002	0.0002	0.3605	0.0002	0.0002	0.3637	0.0002	0.0002
1.78	0.2498	0.0000	0.2449	0.0001	0.0001	0.0001	0.2621	0.0001	0.0001	0.2585	0.0005	0.0005	0.2742	0.0002	0.0002
5.11	0.0708	0.0001	0.0667	0.0000	0.0000	0.0001	0.0819	0.0001	0.0001	0.0760	0.0000	0.0000	0.0923	0.0001	0.0001
7.38	0.0313	0.0001	0.0293	0.0000	0.0000	0.0001	0.0382	0.0001	0.0001	0.0350	0.0001	0.0001	0.0452	0.0000	0.0000

After taking measurements with aluminum absorbers, the measurements

were repeated with Copper as absorber, using the same experimental setup as shown in Figure 7.9 and using the same beam specifications as mentioned above with each beam. Eight different thicknesses of copper absorbers were used in the measurement with each beam.

7.4 Validity of the estimated spectrum

Unless there is an efficient detector with very high resolution that can be used to measure directly the energy spectrum of an x-ray beam having very large flux, estimated energy spectra cannot be validated experimentally. The accuracy of the estimated energy spectra of x-ray beams should therefore be validated by calculating some quantities which depend on the energy spectra that also can be measured in a reproducible way. The energy spectra derived from the measured dose-depth datasets using various methods found in literature are found to be validated either (i) by comparing with the energy spectra derived from Monte Carlo simulation, or (ii) by comparing the calculated dose-depth dataset with the measured dose-depth dataset with other absorber materials.

Due to inadequate information regarding the internal geometry of the linacs used in this project, the energy spectra of x-ray beams could not be simulated using a Monte Carlo method. The energy spectra for all x-ray beams that are used by treatment planning software associated with the linacs were also not provided by the facility, Oklahoma Cancer Specialists and Research Institute (OCSRI) where the measurements were obtained.

In this project, the energy spectrum of an x-ray beam was estimated by using the dose-depth dataset measured by one absorber material and then the spectrum

was validated by comparing a calculated dose-depth dataset for a different absorber material with the measured dose-depth dataset. As described in Section 7.3, two sets of dose-depth data were measured in each beam. One dataset was used to estimate the energy spectrum of x-ray beam and the other dataset was used to validate the estimated energy spectrum.

Chapter 8

Results and Discussion

8.1 Energy spectrum of a 6 MVp x-ray beam

The energy spectrum of a 6 MVp x-ray beam, produced by Elekta's Versa-HD linac, was estimated by using the dose-depth dataset measured with aluminum absorbers. A guess spectrum required for the calculation was defined by using equation (5.3), with σ modified to $\sigma/2.5$, and is shown in Figure 8.1(left). The minimum and the maximum photon energy in the beam were considered to be 0.15 MeV and 6 MeV respectively. The choice of the minimum photon energy was only an estimation whereas the maximum photon energy was chosen to be equal to the initial kinetic energy of the electrons that would be incident on an electron target to produce a 6 MVp x-ray beam. The effect of choosing different values of the minimum photon energy in the shape of an estimated energy spectrum is discussed in a different section below. The guess spectrum was defined by considering 19 energy bins so that the number of energy bins was equal to the number of data points in the measured dose-depth dataset.

Figure 8.1(right) shows a plot of the amount of charge (normalized) created inside the sensitive volume of an ionization chamber due to the beam attenuated by the absorber of various thicknesses, presented in Table 7.2. The measured data was interpolated to get the exposures behind absorbers of thicknesses with equal increments of $\Delta x = 1.45$ cm.

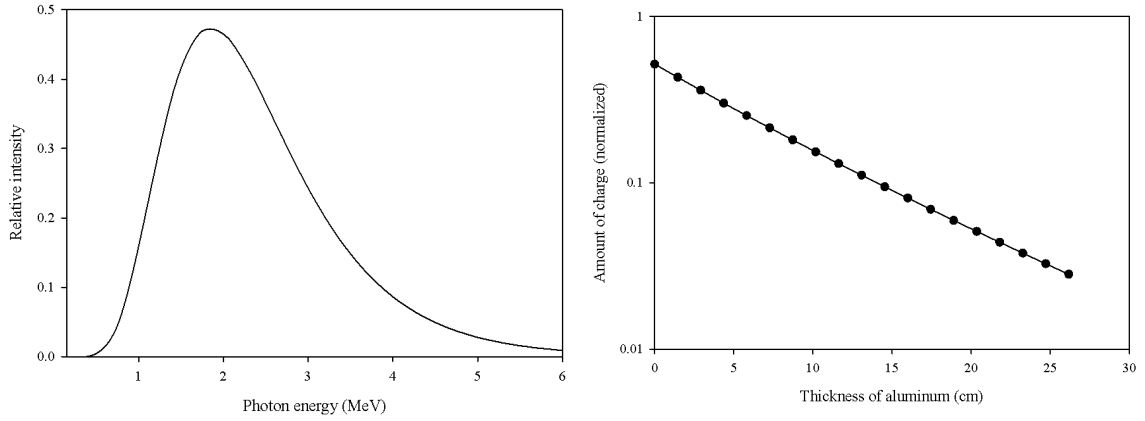


Figure 8.1: Plot of a guess energy-spectrum (left) containing 19 energy bins with photon energy ranging from 0.1 MeV to 6 MeV and a plot of the dose-depth data (right) measured with aluminum in a 6 MVp x-ray beam.

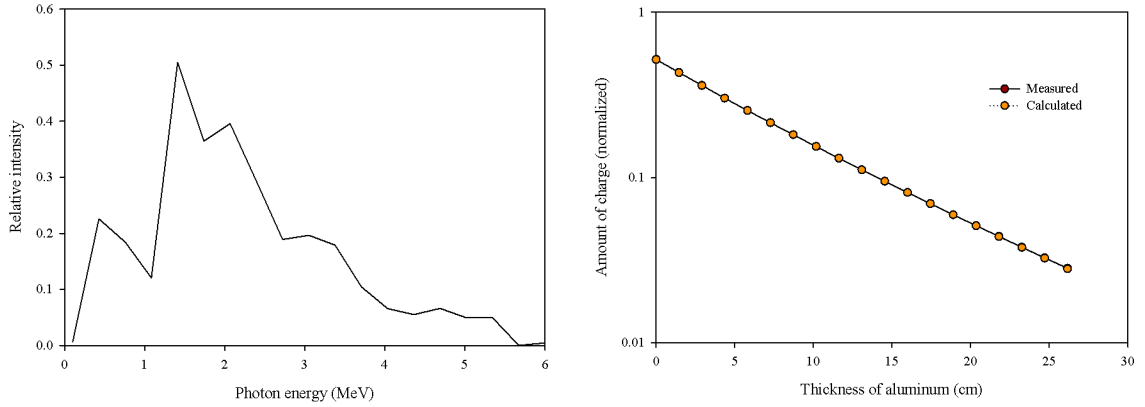


Figure 8.2: A plot of an improved energy spectrum (left) obtained by performing 25 iterations on the guess spectrum shown in Figure 8.1. The right in the right side is a comparison between the dose-depth data calculated using the improved spectrum and corresponding the measured dose-depth data with aluminum absorbers.

Figure 8.2(left) shows a plot of the energy spectrum obtained by iteratively improving the guess spectrum shown in Figure 8.1 until the calculated dose-depth dataset matched the measured dose-depth dataset. A total of 25 iterations were performed before the spectral shape stopped changing significantly. The dose-depth dataset calculated using the improved spectrum is compared with the measured dose-depth dataset in the right side of Figure 8.2. The total percent difference between these two datasets was found to be 0.18%.

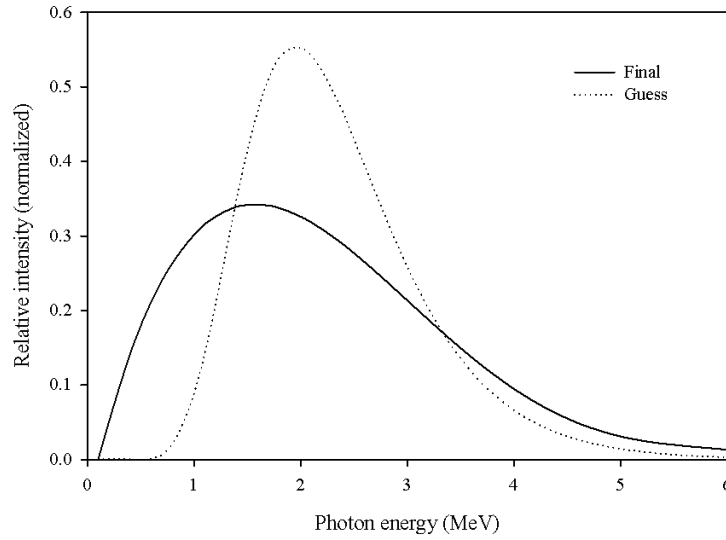


Figure 8.3: An estimated energy spectrum of a 6 MVp x-ray beam produced by Elekta's Versa-HD linac. The guess spectrum used in the calculation is shown dotted line.

The spectrum obtained at the end of 25th iteration, shown in Figure 8.2, contains unphysical peaks and valleys. It was smoothed by fitting a polynomial of degree 4:

$$I(E) = -4.931 \times 10^{-4} E^4 + 8.628 \times 10^{-3} E^3 - 5.104 \times 10^{-2} E^2 + 1.042 \times 10^{-1} E - 9.917 \times 10^{-3}, \quad (8.1)$$

where $I(E)$ represents the relative intensity of x-ray photons with energy E . Figure 8.3 shows the energy spectrum after smoothing. The guess spectrum used in the calculation is also plotted in the same figure. Both the guess and the final spectrum were normalized in such a way that the area under each curve is equal to 1.

It can be noticed from Figure 8.3 that the relative intensity of x-rays is zero at 0.15 MeV, the estimated minimum photon energy. The intensity of x-rays increases rapidly as the photon energy increases and has a peak approximately at 1.6 MeV and then decreases as the photon energy decreases. The intensity approaches

almost exponentially to 0 at the maximum photon energy. The intensity of x-rays at the maximum photon energy is not exactly 0 as expected theoretically but decreases by 96% from its maximum value. The peak of the spectrum was found to shift from 2 MeV in the guess spectrum to about 1.6 MeV in the final spectrum.

8.1.1 Validation of the estimated spectrum of 6 MVp x-ray beam

The validity of the energy spectrum of a 6 MVp x-ray beam produced by an Elekta Versa HD linac, estimated from the measured dose-depth dataset with aluminum absorbers, was assessed by calculating the dose-depth datasets for aluminum and copper absorbers and comparing them with the corresponding measured datasets.

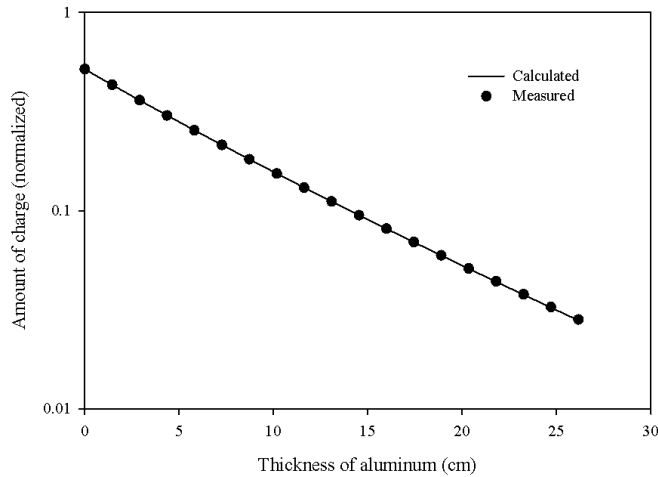


Figure 8.4: A comparison of the dose-depth dataset, calculated for aluminum absorbers using the estimated energy spectrum (Figure 8.3) of a 6 MVp x-ray beam, and the measured dose-depth dataset from Table 7.4.

Figure 8.4 shows plots of the calculated and the measured dose-depth dataset for aluminum absorbers. The energy spectrum estimated by using the dose-depth data measured for aluminum absorber was used to calculate the dose-depth

dataset. The total percent difference between the two datasets was found to be 0.22%, which is comparable to the value calculated using the estimated energy spectrum before smoothing in Figure 8.2.

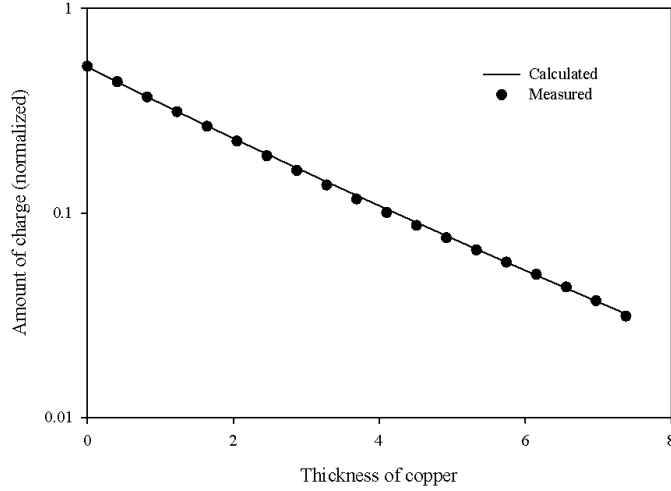


Figure 8.5: A comparison of the dose-depth dataset, calculated for copper absorbers using the estimated energy spectrum (Figure 8.3) of a 6 MVp x-ray beam, and the measured dose-depth dataset from Table 7.4.

Figure 8.5 shows plots of the calculated and the measured dose-depth dataset for copper absorbers. The calculated dose-depth data was obtained by using the estimated energy spectrum of a 6 MVp x-ray beam, shown in Figure 8.3 and the measured dose-depth data was taken from Table 7.4. The total percent difference between these two datasets was found to be 1.71%. Since the estimated energy spectrum of a 6 MVp x-ray beam, shown in Figure 8.3, produced dose-depth datasets for two different absorber materials agree well with the corresponding measured dose-depth datasets, the estimated energy spectrum is likely close to the true energy spectrum of the beam. It is unlikely that a spectrum with smaller uncertainty is possible given the available information regarding the beam.

8.2 Energy spectrum of a 10 MVp x-ray beam

The energy spectrum of a 10 MVp x-ray beam, produced by an Elekta Versa HD linac, was estimated by using the dose-depth dataset measured with aluminum absorbers. Figure 8.6(left) shows a guess spectrum containing 19 discrete energy bins that was used in the calculation. It is a log normal distribution defined by equation (5.3). The parameter σ in equation (5.3) was replaced by $\sigma/2.5$ so that the peak of the guess spectrum was approximately at 3.33 MeV, i.e. at $1/3^{\text{rd}}$ of the maximum photon energy. The minimum photon energy in the guess spectrum was estimated to be 0.1 MeV and the maximum photon energy was chosen to be 10 MeV.

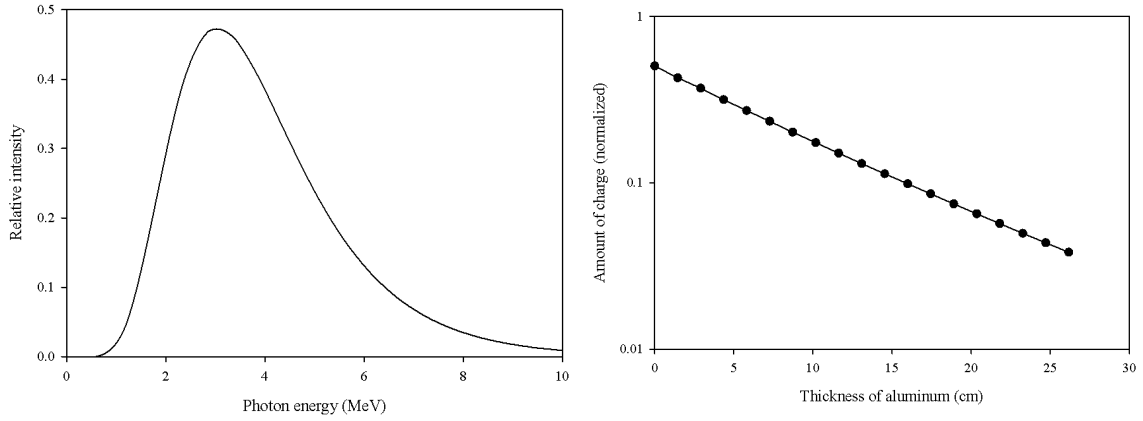


Figure 8.6: Plot of a guess energy-spectrum (left) containing 19 energy bins with photon energy ranging from 0.1 MeV to 10 MeV and a plot of the dose-depth data (right) measured with aluminum absorbers in a 10 MVp x-ray beam.

Figure 8.6(right) shows a plot of the dose-depth dataset, measured with aluminum absorbers in the 10 MVp x-ray beam, from Table 7.3. In this plot, the data were interpolated to get the exposures behind absorbers of thickness with equal increments of $\Delta x = 1.45$ cm.

Figure 8.7 shows the improved energy spectrum, obtained by performing 6 iterations on the guess spectrum shown in Figure 8.6. The spectrum was found

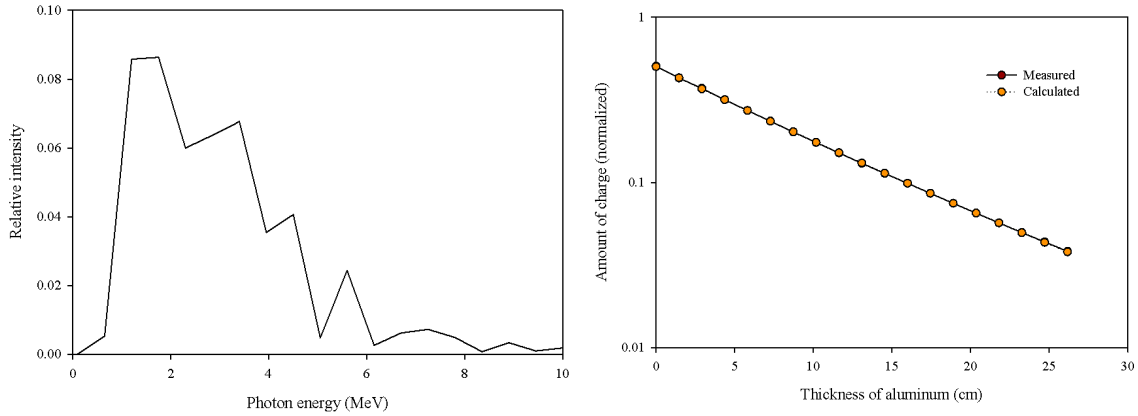


Figure 8.7: A plot of the energy spectrum (left) obtained by improving the guess spectrum shown in Figure 8.1. On the right is a comparison between the measured dose-depth data and the dose-depth data calculated using the improved spectrum.

to completely stop improving beyond 31 iterations. However, there was insignificant change in the spectral shape beyond 6th iteration. Figure 8.7 also shows the dose-depth dataset calculated by using the spectrum corresponding to the 6th spectrum and the measured dose-depth dataset. The total percent difference between these two datasets was found to be 0.28%.

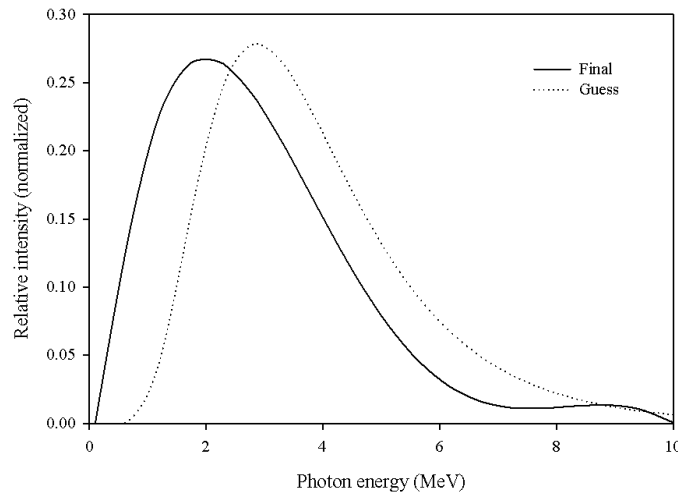


Figure 8.8: An estimated energy spectrum of a 10 MVp x-ray beam produced by Elekta Versa-HD linac. The guess spectrum used in the calculation is shown dotted line.

The energy spectrum shown in Figure 8.7 was smoothed by fitting a polynomial of degree 5:

$$I(E) = 1.287 \times 10^{-5}E^5 - 5.247 \times 10^{-4}E^4 + 7.736 \times 10^{-3}E^3 - 4.967 \times 10^{-2}E^2 + 1.215 \times 10^{-1}E - 2.270 \times 10^{-2}, \quad (8.2)$$

where $I(E)$ represents the relative intensity of x-ray photons with energy E . Figure 8.8 shows a plot of the energy spectrum of 10 MVp x-ray beam after smoothing. It also shows the guess spectrum used in the calculation. Both the guess and the final spectrum were normalized such that the area under each plot is equal to 1. The final energy spectrum shows that the intensity of x-rays is 0 at the estimated minimum photon energy of 0.1 MeV. Then the intensity increases rapidly with the increase of photon energy and has a peak at about 2.0 MeV. Above 2.0 MeV, the intensity of x-rays decreases gradually with the increase of photon energy and approaches to 0 at the maximum photon energy of 10 MeV.

It can be noticed from Figure 8.8 that the relative intensity of x-rays with energy from 7 to 9 MeV is almost constant and is about 3.7% of its maximum value. The plateau region at the higher energy end of the estimated energy spectrum cannot be explained based on the information used to estimate the spectrum. The improved energy spectrum, shown in Figure 8.7, was also tested to smooth by fitting polynomials of degree less than or greater than 5. Polynomials of degree other than 5 were not found to produce better shape of the spectrum which satisfies all the criteria of spectral shape. The plateau region could be due to a poor estimation of the minimum photon energy or be an artifact introduced by the choice of the function used to smooth out the improved spectrum.

8.2.1 Validation of the estimated spectrum of 10 MVp x-ray beam

The validity of the energy spectrum of a 10 MVp x-ray beam produced by Elekta Versa-HD linac (Figure 8.8), estimated from the dose-depth dataset measured with aluminum absorber, was assessed by calculating the dose-depth datasets for aluminum and copper absorbers and comparing them with the corresponding measured datasets.

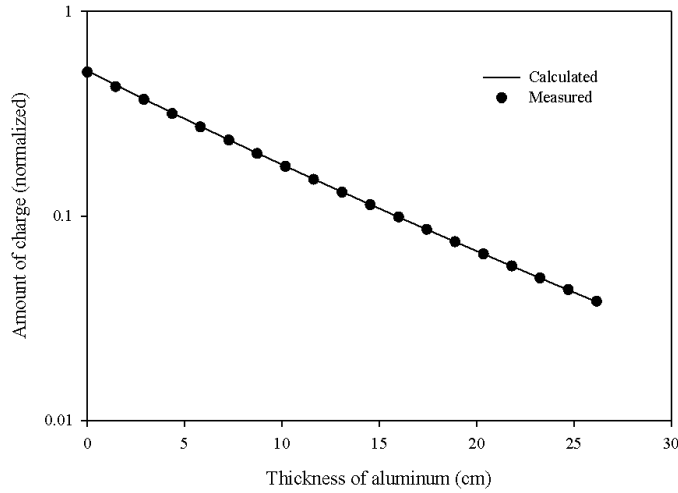


Figure 8.9: A comparison between the dose-depth dataset, calculated for aluminum absorbers using the estimated energy spectrum (Figure 8.3) of a 10 MVp x-ray beam, and the measured dose-depth dataset.

Figure 8.9 shows a plot of the dose-depth data calculated for aluminum using the estimated energy spectrum of a 10 MVp x-ray beam compared with the measured dose-depth data. The total percent difference between these two datasets was found to be 0.51%.

Figure 8.10 shows a comparison between the dose-depth dataset calculated using the estimated energy spectrum of a 10 MVp x-ray beam, shown in Figure 8.8,

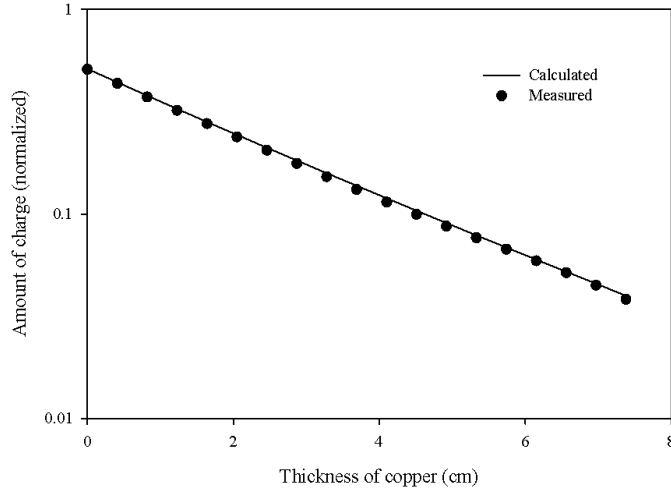


Figure 8.10: A comparison between the dose-depth dataset, calculated for copper absorbers using the estimated energy spectrum (Figure 8.3) of a 10 MVp x-ray beam, and the measured dose-depth dataset.

and the corresponding measured dose-depth data. The total percent difference between these two datasets was found to be 2.69%. From the agreement between the calculated and the measured dose-depth datasets for two different absorbers as shown in Figure 8.9 and 8.10, it can be concluded that the estimated energy spectrum of a 10 MVp x-ray beam is very close to the true energy spectrum of the beam.

8.3 Energy spectrum of a 6 MVp filter-free x-ray beam

The energy spectrum of a 6MVp x-ray beam, produced by Elekta Versa-HD in the absence of a flattening filter, was estimated by using the dose-depth dataset measured with aluminum absorbers. A guess spectrum containing 19 equally spaced energy bins was defined by using equation (5.3), with σ modified to $\sigma/3.0$, and it is shown in Figure 8.1(left). The minimum and the maximum photon energy in the beam

were considered to be 0.01 MeV and 6 MeV respectively. The minimum photon energy was chosen smaller than the value chosen in the estimation of the energy spectrum of a 6 MVp x-ray beam with flattening filter.

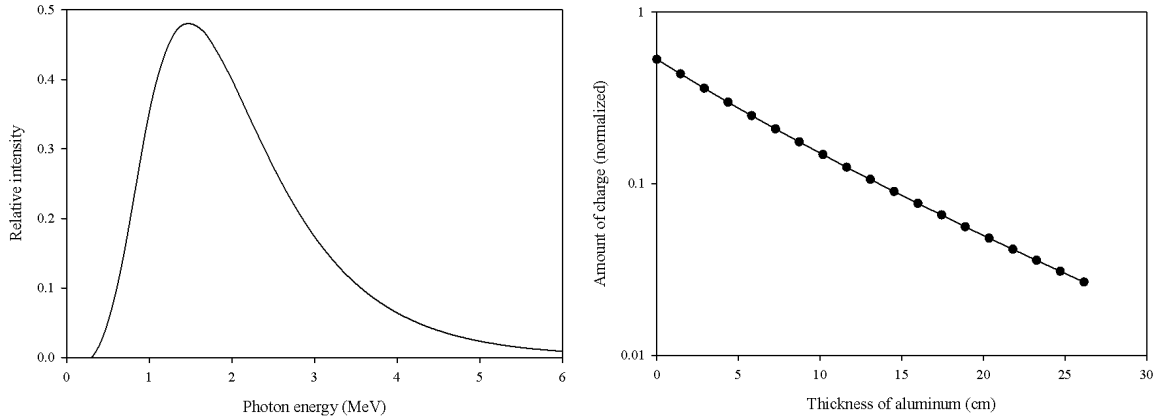


Figure 8.11: Plot of a guess energy-spectrum (left) containing 19 energy bins with photon energy ranging from 0.01 MeV to 6 MeV and a plot of the dose-depth data (right) measured with aluminum absorbers in a 6 MVp x-ray beam in the absence of flattening filter.

Figure 8.11(right) shows a plot of the dose-depth dataset, measured with aluminum absorbers in the 6 MVp filter-free x-ray beam, from Table 7.3. In this plot, the data were interpolated to get the exposures behind absorbers of thickness with equal increments of $\Delta x = 1.45$ cm.

The guess spectrum shown in Figure 8.11 was iteratively improved until the total percent difference between the measured and calculated dose-depth datasets was reduced to 0.28%. Figure 8.12 shows the energy-spectrum of a 6 MVP filter free beam obtained at the end of 12th iteration. A comparison between the dose-depth dataset calculated using the improved spectrum and the measured dose-depth data is shown in the right side of Figure 8.12.

The energy spectrum shown in Figure 8.12 was smoothed by fitting a poly-

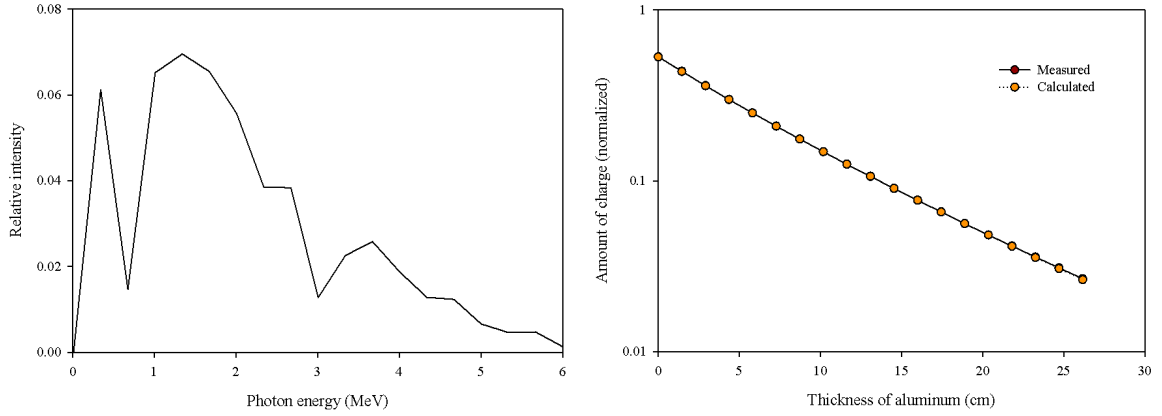


Figure 8.12: A plot of the energy spectrum (left) obtained by improving the guess spectrum shown in Figure 8.1. On the right is a comparison between the measured dose-depth data and the dose-depth data calculated using the improved spectrum.

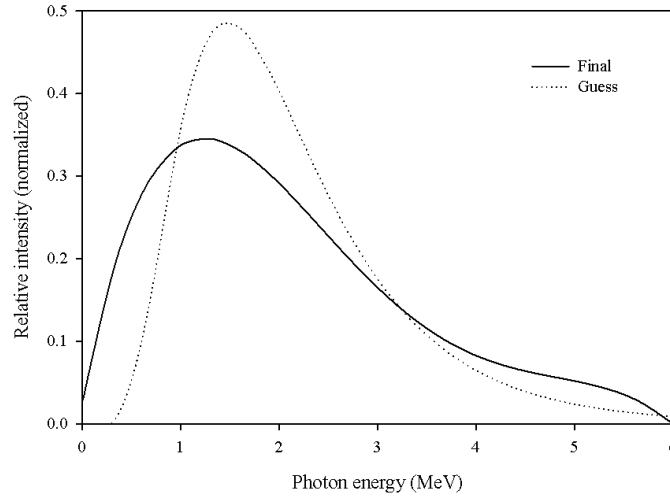


Figure 8.13: An estimated energy spectrum of a 6 MVp FFF x-ray beam produced by Elekta Versa-HD linac. The guess spectrum used in the calculation is shown dotted line.

nomial of degree 5:

$$I(E) = 5.430 \times 10^{-5} E^5 - 1.681 \times 10^{-3} E^4 + 1.697 \times 10^{-2} E^3 - 7.185 \times 10^{-2} E^2 + 1.122 \times 10^{-1} E - 4.041 \times 10^{-3}, \quad (8.3)$$

where $I(E)$ is the relative intensity of x-rays with energy E . The energy spectrum after smoothing with a polynomial of degree 5 is shown in Figure 8.13. In the same Figure, the guess spectrum used in the calculation is also shown. It can be noticed

that the relative intensity of x-rays with estimated minimum photon-energy is non-zero and is approximately 1% of its maximum value. The intensity increases rapidly with the increase of photon energy from 0.01 MeV. The peak of the final spectrum is at the photon energy of approximately 1.25 MeV which is smaller than the assumed value of the peak energy. The intensity of x-rays decreases beyond the peak energy and asymptotically approaches to zero at the maximum photon energy.

8.3.1 Validation of the estimated spectrum of 6 MVp FFF x-ray beam

The estimated energy spectrum of a 6 MVp filter-free beam, shown in Figure 8.13, was used to calculate a dose-depth dataset for aluminum absorbers. The calculated dose-depth data was compared with the corresponding measured dose-depth data as shown in Figure 8.14. The total percent difference between these two datasets was found to be 0.34%.

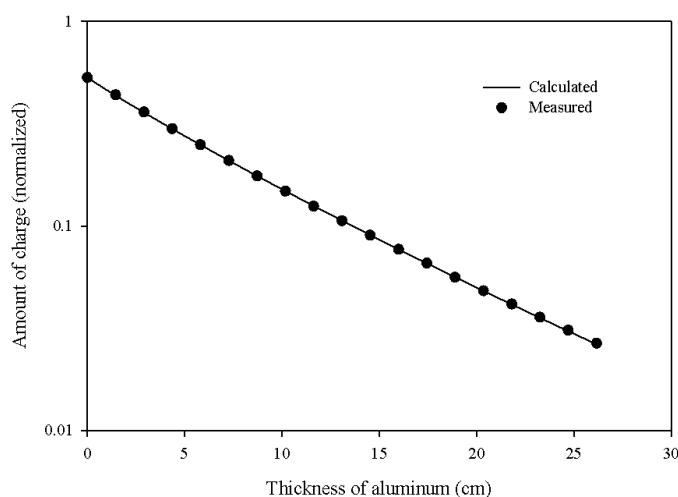


Figure 8.14: A comparison between the dose-depth dataset, calculated for aluminum absorbers using the estimated energy spectrum (Figure 8.3) of a 10 MVp x-ray beam, and the measured dose-depth dataset.

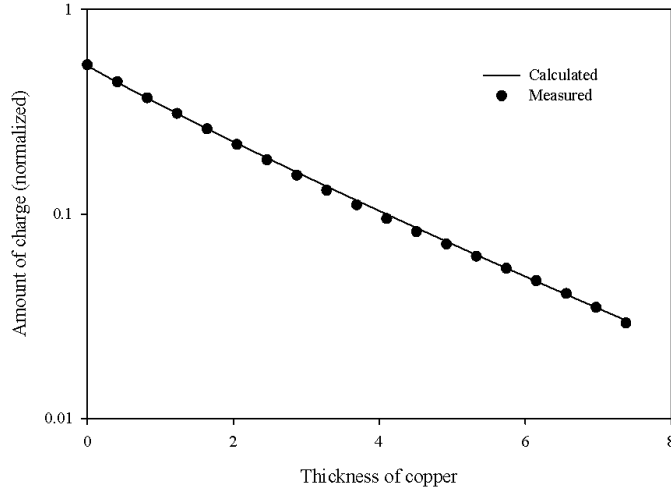


Figure 8.15: A comparison between the dose-depth dataset, calculated for aluminum absorbers using the estimated energy spectrum (Figure 8.3) of a 10 MVp x-ray beam, and the measured dose-depth dataset.

The estimated energy spectrum of a 6 MVp filter-free beam, shown in Figure 8.13, was also used to calculate a dose-depth dataset for copper absorbers. Figure 8.15 shows a comparison between the calculated and the measured dose-depth datasets for copper. It can be noticed that the calculated dose-depth dataset is in very good agreement with the measured dataset. The total percent difference between these two datasets was found to be 2.03%.

8.4 Energy spectrum of a 10 MVp filter-free x-ray beam

The energy spectrum of a 10 MVp filter-free x-ray beam, produced by Elekta Versa-HD, was estimated by using the dose-depth dataset measured with aluminum absorbers. A guess spectrum containing 19 equally spaced energy bins and photon energy ranging from 0.01 to 10 MeV was defined by using equation (5.3), with

σ modified to $\sigma/2.5$. The measured dose-depth data from Table 7.3 was interpolated to have the exposures behind absorbers of thicknesses with equal increments. Figure 8.16 shows the plots of the guess spectrum and measured dose-depth dataset used in the estimation of the energy spectrum of 10 MVp filter-free beam.

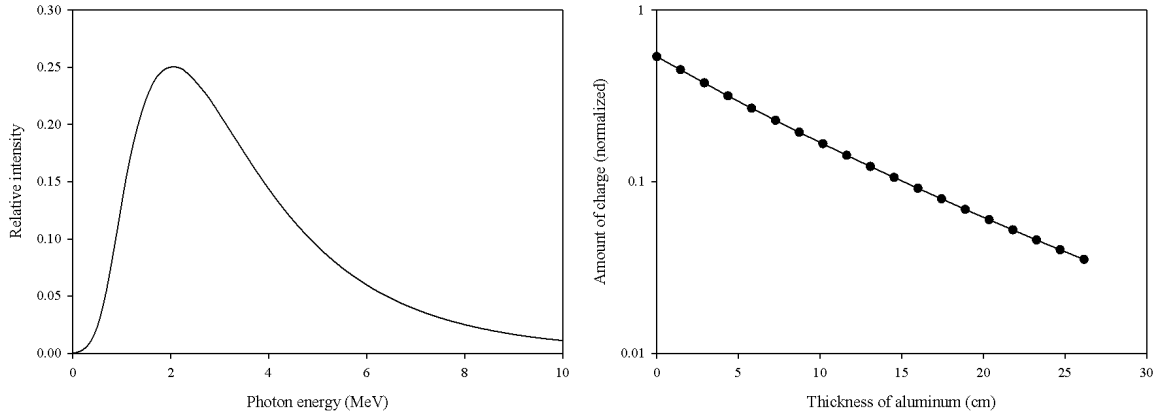


Figure 8.16: Plot of a guess energy-spectrum (left) containing 19 energy bins with photon energy ranging from 0.01 MeV to 10 MeV and a plot of the dose-depth data (right) measured with aluminum absorbers in a 10 MVp filter free x-ray beam.

The guess spectrum was iteratively improved until the calculated dose-depth data matched the corresponding measured dose-depth data. Although the spectrum was found to completely change its shape after performing 39 iterations, the change in the spectral shape beyond 4th iteration was negligibly small. Figure 8.17(left) shows an improved energy spectrum obtained at the end of 4th iteration. A comparison between the dose-depth data, calculated with the improved spectrum, and the measured dose-depth data. The total percent difference between these two datasets was found to be 0.58%.

The energy spectrum shown in Figure 8.17 was smoothed, in order to get rid of unrealistic peaks and valleys, by fitting a polynomial of degree 5:

$$I(E) = -8.091 \times 10^{-6}E^5 + 3.086 \times 10^{-4}E^5 - 4.647 \times 10^{-3}E^4 + 3.462 \times 10^{-2}E^3 - 1.286 \times 10^{-1}E^2 + 1.952 \times 10^{-1}E - 9.059 \times 10^{-3}, \quad (8.4)$$

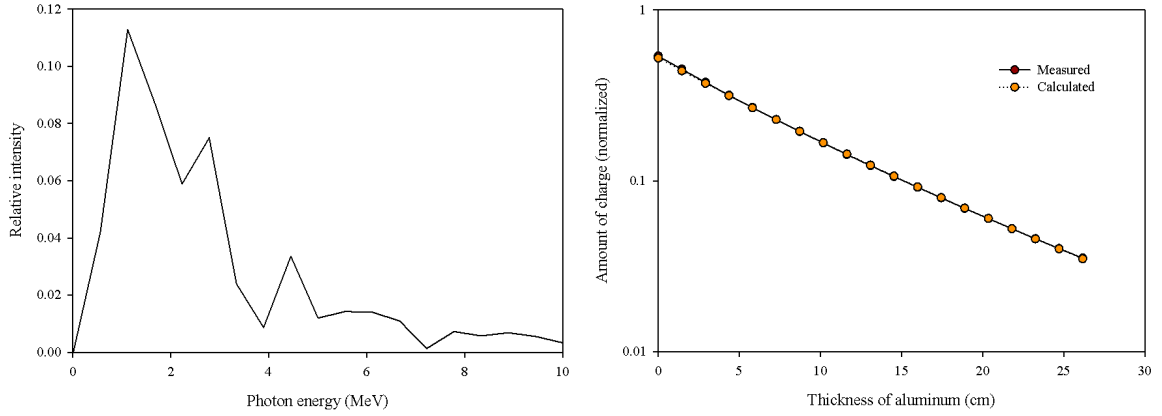


Figure 8.17: A plot of the energy spectrum (left) obtained by improving the guess spectrum shown in Figure 8.1. On the right is a comparison between the measured dose-depth data and the dose-depth data calculated using the improved spectrum.

where $I(E)$ is the relative intensity of x-rays with energy E . The energy spectrum after smoothing with a polynomial of degree 6 is shown in Figure 8.18. Figure 8.18 also shows the guess spectrum used in the calculation. Both spectra were normalized so that the area under each curve is equal to 1.

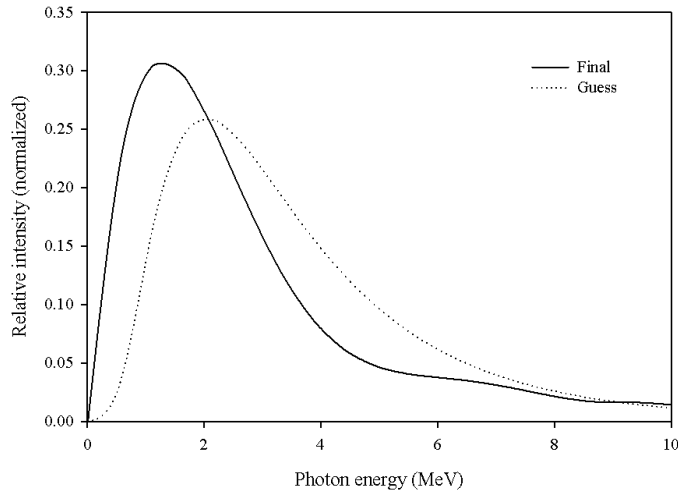


Figure 8.18: An estimated energy spectrum of a 10 MVp FFF x-ray beam produced by Elekta Versa-HD linac. The guess spectrum used in the calculation is shown dotted line.

8.4.1 Validation of the estimated spectrum of 10 MVp filter-free x-ray beam

The estimated energy-spectrum of a 10 MVp filter-free x-ray beam, shown in Figure 8.18, was used to calculate a dose-depth dataset for aluminum absorbers and compared with the measured dose-depth dataset. Figure 8.19 shows a comparison between the calculated and the measured dose-depth datasets for aluminum. The total percent difference between these two datasets was found to be 0.35%.

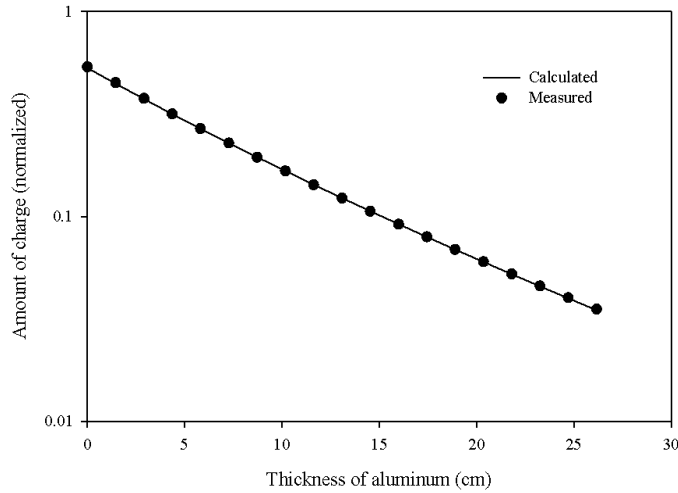


Figure 8.19: A comparison between the dose-depth dataset, calculated for aluminum absorbers using the estimated energy spectrum (Figure 8.3) of a 10 MVp filter-free x-ray beam, and the measured dose-depth dataset.

Figure 8.20 shows a plot of a dose-depth dataset, calculated using the estimated energy spectrum shown in Figure 8.18, and the measured dose-depth dataset with copper absorbers. It can be noticed from graph that the calculated data is in good agreement with the measured data at the thicknesses from 0 to 2.5 cm and from 5.0 to 7.4 cm. At thicknesses between 2.5 and 5.0 cm, the calculated values are slightly greater than the measured values. The total percent difference between these two datasets was found to be 2.15%.

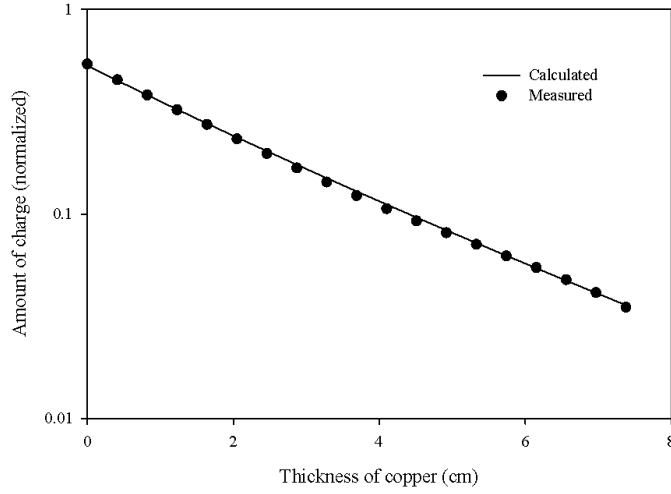


Figure 8.20: A comparison between the dose-depth dataset, calculated for copper absorbers using the estimated energy spectrum (Figure 8.3) of a 10 MVp filter-free x-ray beam, and the measured dose-depth dataset.

8.5 Energy spectrum of a 18 MVp x-ray beam

The energy spectrum of a 18 MVp x-ray beam, produced by Elekta VersaHD, was estimated by using the dose-depth dataset measured with aluminum absorbers. A guess spectrum containing 19 equally-spaced energy bins, defined by equation 5.3, was used in the calculation. The parameter σ was modified to $\sigma/2.5$ in order to have the peak of the guess spectrum in about $1/3^{\text{th}}$ of the maximum photon energy (18 MeV). The minimum photon energy was estimated to be 0.1 MeV. The measured dose-depth dataset was interpolated to have the exposures due to the attenuated x-ray beams by absorbers of thicknesses with equal increments of 1.45 cm. Figure XXX shows the plots of the guess spectrum (left) and measured dose-depth dataset (right) that were used to estimate the energy spectrum of 18 MVp x-ray beam.

Figure 8.22 shows an energy spectrum obtained by iteratively improving the guess spectrum shown in Figure 8.21. The spectrum was stopped after performing 5

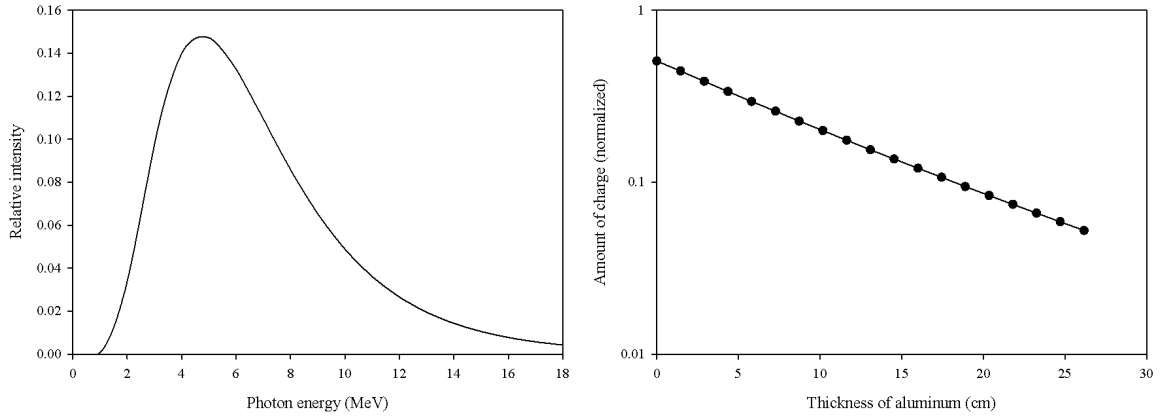


Figure 8.21: Plot of a guess energy-spectrum (left) containing 19 energy bins with photon energy ranging from 0.1 MeV to 18 MeV and a plot of the dose-depth data (right) measured with aluminum absorbers in a 18 MVp x-ray beam.

iterations. Beyond 5th, negligibly small changes in the spectral shape were found. The dose-depth dataset calculated with the improved energy spectrum is compared with the measured dose-depth dataset in Figure 8.22(right). The total percent difference between these two datasets was found to be 0.56%.

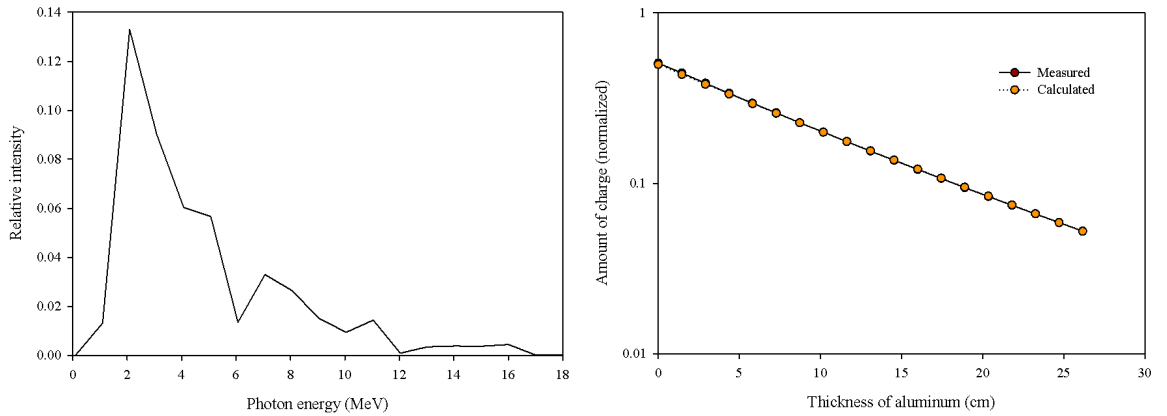


Figure 8.22: A plot of the energy spectrum (left) obtained by improving the guess spectrum shown in Figure 8.21. On the right is a comparison between the measured dose-depth data and the dose-depth data calculated using the improved spectrum.

The energy spectrum shown in Figure 8.22 that contains unrealistic peaks

and valleys was smoothed by fitting a polynomial of degree 6:

$$I(E) = -2.480 \times 10^{-7} E^6 + 1.704 \times 10^{-5} E^5 - 4.628 \times 10^{-4} E^4 + 6.240 \times 10^{-3} E^3 - 4.223 \times 10^{-2} E^2 + 1.192 \times 10^{-1} E - 2.563 \times 10^{-2}, \quad (8.5)$$

where $I(E)$ is the relative intensity of x-ray photons with energy E .

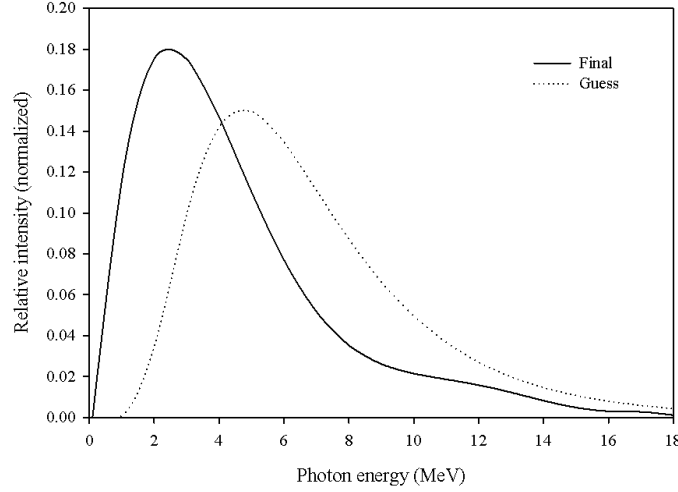


Figure 8.23: An estimated energy spectrum of a 18 MVp x-ray beam produced by Elekta Versa-HD linac. The guess spectrum used in the calculation is shown dotted line.

Figure 8.23 shows the estimated spectrum of the 18 MVp x-ray beam produced by Elekta Versa-HD linac. The guess spectrum used in the calculation is also shown in the same graph for a comparison. Each spectrum in Figure 8.23 is normalized so that the area under the spectrum is equal to 1. It can be noticed from the plots that the relative intensity of x-rays is zero at the minimum photon energy, then increases rapidly and has a maximum value at photon energy of about 2.5 MeV. Beyond the peak energy, the intensity falls off rapidly upto the photon energy of 8 MeV, then it decreases slowly and approaches 0 at the maximum photon energy.

8.5.1 Validation of the estimated spectrum of 18 MVp x-ray beam

The validity of the estimated energy spectrum of a 18 MVp x-ray beam, shown in Figure 8.23, was assessed by calculating the dose-depth datasets for aluminum and copper absorbers and comparing them with the corresponding measured datasets.

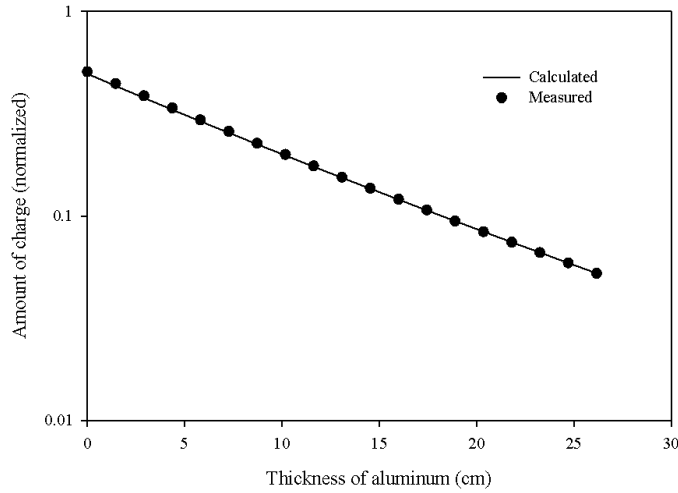


Figure 8.24: A comparison between the dose-depth dataset, calculated for aluminum absorbers using the estimated energy spectrum (Figure 8.3) of a 18 MVp x-ray beam, and the measured dose-depth dataset.

Figure 8.24 shows the plots of the dose-depth dataset calculated for aluminum absorbers using the estimated energy spectrum and the measured dose-depth dataset. The total percent difference between these two datasets was found to be 0.88%.

Figure 8.25 shows the plots of the dose-depth dataset calculated for copper absorbers using the estimated energy spectrum and the measured dose-depth dataset. The total percent difference between these two datasets was found to be 2.54%.

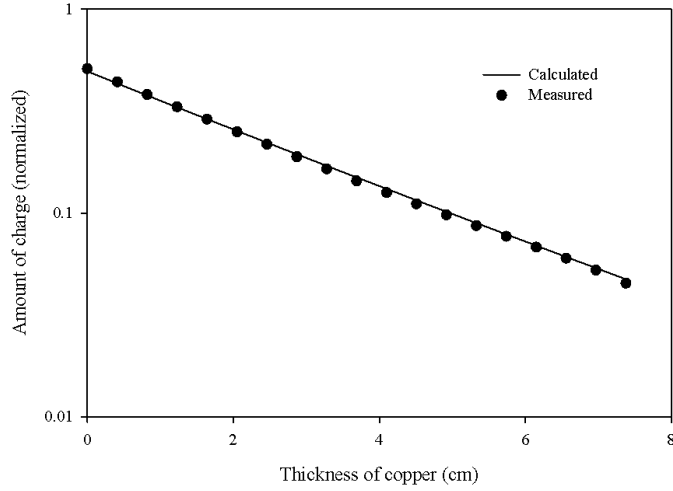


Figure 8.25: A comparison between the dose-depth dataset, calculated for copper absorbers using the estimated energy spectrum (Figure 8.3) of a 10 MVp filter-free x-ray beam, and the measured dose-depth dataset.

8.6 Sensitivity analysis of the spectrum estimating algorithm

8.6.1 Choice of the minimum photon energy

The minimum photon energy of an x-ray beam produced by a clinical linac depends on the amount of inherent filtration that the beam encounters before exiting the gantry. The filtration of x-ray beam occurs due to various components such as the electron target itself, flattening filter, backing plates of the electron target and flattening filter, wedge filter, etc. The physical details regarding the filtration inside the Elekta Versa-HD linac that was used to obtain dose-depth datasets in this project, such as the thickness and composite materials of the electron target, flattening filters, scattering foils, and backing plates, were not available. Based on the published x-ray energy and the geometries used to simulate therapeutic x-ray beams found in the

literature, the minimum photon energy of a megavolt x-ray beams was found to vary between 100 keV to 500 keV. In this project, dose-depth datasets were measured in 6 and 10 MVp x-ray beams with and without flattening filters. While estimating the energy spectra of filter free x-ray beams the minimum photon energy was estimated to be 10 keV and for all other x-ray beams produced by linac with flattening filters, the minimum photon energy was estimated to be 100 keV.

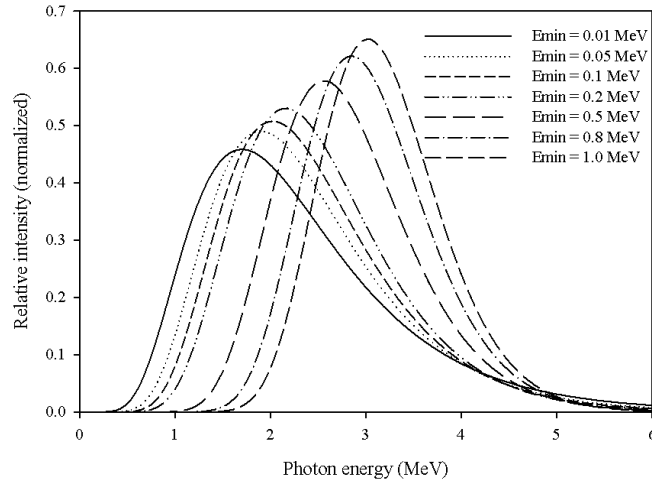


Figure 8.26: Guess spectra with different values of minimum photon energy (E_{min}). Each guess spectrum was defined by a modified log normal distribution given in equation (5.3).

As described in Chapter 5, the minimum photon energy (E_{min}) is one of the required input parameters to estimate the energy spectrum of an x-ray beam using the dose-depth datasets. To see effect of the choice of minimum photon energy in the shape of an estimated energy spectrum, the spectrum of a 6 MVp x-ray beam was estimated considering six different values of E_{min} . Figure 8.26 shows the guess spectra with different values of E_{min} . Each of these guess spectra was defined by using equation (5.3) by keeping all other parameters same except the minimum photon energy. Each guess spectrum contains 50 equally spaced energy bins.

Each guess spectrum shown in Figure 8.26 was iteratively recalculated until

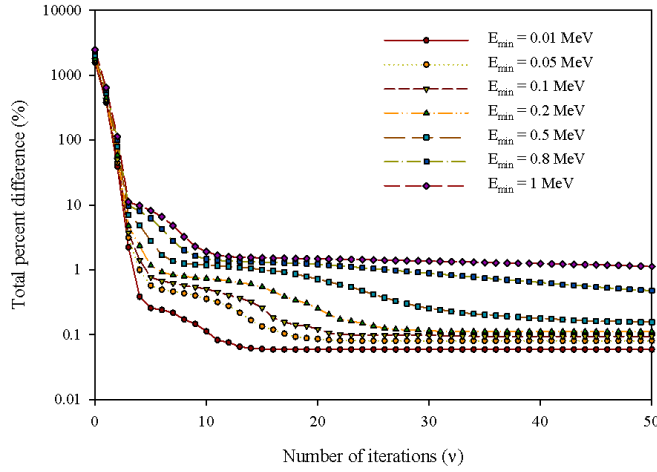


Figure 8.27: The total percent difference (d) between calculated and measured dose-depth datasets plotted as a function of the number of iterations performed. Different curves represent the calculation performed by considering different values of the minimum photon energy (E_{min}) in the spectrum.

the dose-depth dataset matched the corresponding measured dataset. Figure 8.27 shows the plots of the total percent differences between the measured and calculated dose-depth datasets (d) as a function of number of iterations (ν) performed for all calculations. The value of d at $\nu = 0$ denotes the total percent difference calculated using the guess spectrum. Table 8.1 lists out the values of the minimum percent difference between the measured and calculated dose-depth datasets beyond which the energy spectrum was found to stop significantly changing.

It can be noticed from Figure 8.27 and Table 8.1 that the calculation converges fast with the minimum photon energy of 0.01 MeV. With a spectrum that has higher values of E_{min} , a larger number of iterations were required for convergence. With a choice of larger minimum photon energy, the calculated dose-depth dataset was found to be poorer agreement with the measured dataset.

Figure 8.28 shows the iteratively improved energy spectra of a 6 MVp x-ray

Table 8.1: Total number of iterations performed before the spectrum stopped improving significantly and total percent difference between the measured dose-depth datasets and the dose-depth datasets calculated with energy spectra having different minimum photon energy.

E_{min} (MeV)	Number of iterations (ν)	Percent difference, d(%)
0.01	15	0.06
0.05	20	0.09
0.1	21	0.11
0.2	30	0.11
0.5	50	0.16
0.8	118	0.26

beam, each of which was calculated using the guess spectrum with a different minimum photon energy shown in Figure 8.26. A different number of iterations were performed to achieve the minimum difference between the calculated and measured dose-depth dataset as listed in Table 8.1. It can be noticed from Figure 8.28 that the improved energy spectra are significantly different from each other, especially at lower energy.

Table 8.2: Coefficients, A_r , of the polynomials $I(E) = \sum_{r=0}^q A_r E^r$ that were used to fit the spectra having different minimum photon energies shown in Figure 8.28, where, q denotes the degree of the polynomial.

E_{min} (MeV)	A_4	A_3	A_2	A_1	A_0
0.01	-2.05×10^{-4}	3.35×10^{-3}	-1.88×10^{-2}	3.67×10^{-2}	-1.97×10^{-3}
0.05	-1.27×10^{-4}	2.39×10^{-3}	-1.50×10^{-2}	3.19×10^{-2}	-9.78×10^{-4}
0.1	-1.21×10^{-4}	2.33×10^{-3}	-1.49×10^{-2}	3.20×10^{-2}	-1.30×10^{-3}
0.2	-5.20×10^{-5}	1.43×10^{-3}	-1.11×10^{-2}	2.61×10^{-2}	9.39×10^{-4}
0.5		5.14×10^{-4}	-5.39×10^{-3}	1.21×10^{-2}	1.13×10^{-2}
0.8		-6.23×10^{-4}	6.93×10^{-3}	-2.82×10^{-2}	4.90×10^{-2}

All the spectra shown in Figure 8.28 have nonphysical peaks and valleys and each of these spectra was smoothed by fitting a polynomial. The spectra with the minimum photon energies of 0.01, 0.05, 0.1, and 0.2 MeV were smoothed by polynomi-

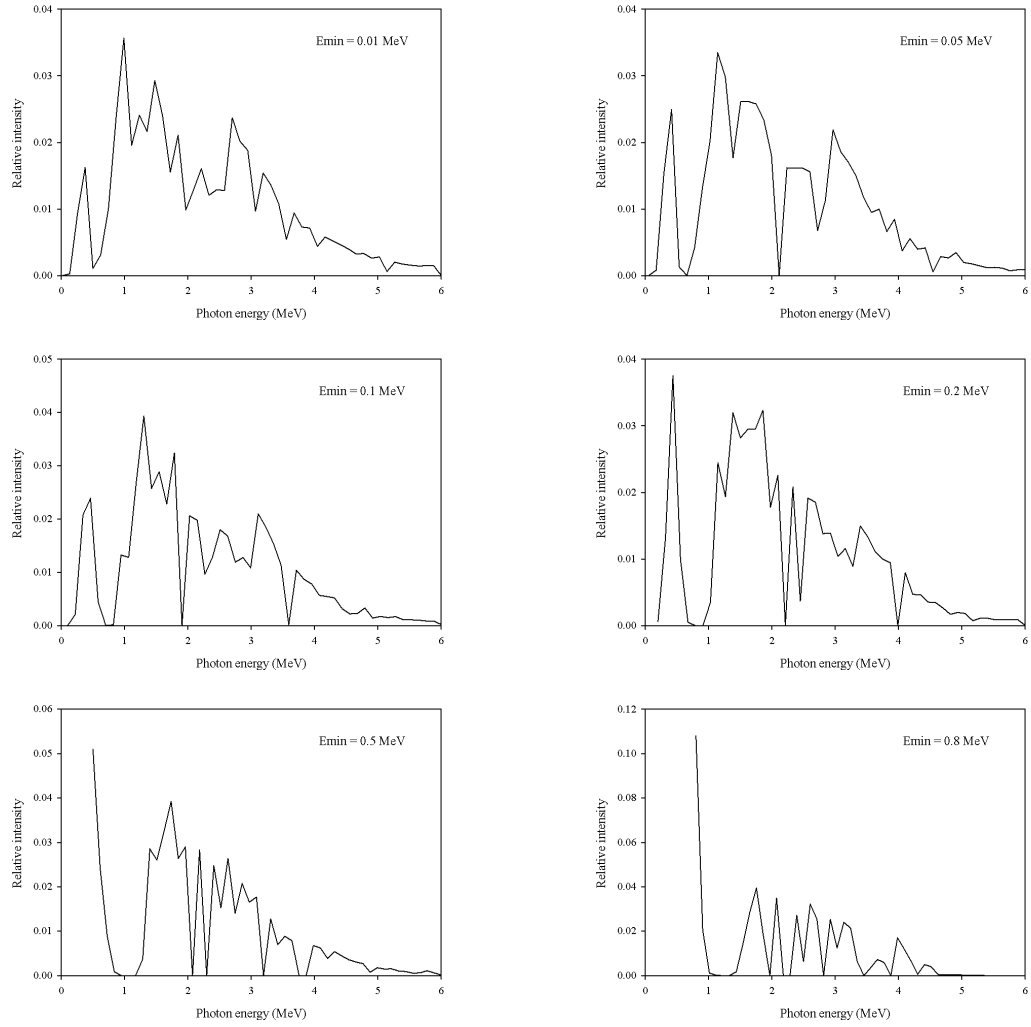


Figure 8.28: Energy spectra of a 6 MVp x-ray beam obtained by iteratively improving the corresponding guess spectra shown in Figure 8.26.

als of degree 4. However, a polynomial of degree 4 was found to poorly fit the spectra with minimum photon energies of 0.5 and 0.8 MeV and these were smoothed by using 3th degree polynomials. Table 8.2 lists out all the coefficients of the polynomials, $I(E) = \sum_{r=0}^q A_r E^r$, that were used to smooth the spectra in Figure 8.28.

Figure 8.29 shows the plots of smoothed energy spectra of a 6 MVp x-ray beam, estimated by considering different values of the minimum photon energy. The spectra with minimum photo energies of 0.01 to 0.2 MeV look very similar to each other. The spectra with the minimum photon energies of 0.5 and 0.8 MeV are

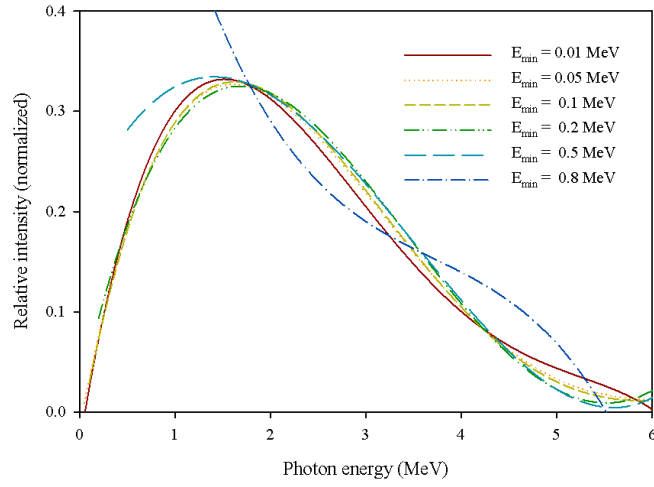


Figure 8.29: Energy spectra of a 6 MVp x-ray beam, estimated by considering different values of the minimum photon energy of the beam.

significantly different from rest of the spectra, especially at the lower energy region. Additionally, the spectrum with $E_{min} = 0.8$ MeV does not agree with the expected shape of the spectrum. Based on this calculation, it can be said that the minimum photon energy of the 6 MVp x-ray beam, in which the dose-depth dataset was obtained, is less than 0.2 MeV but cannot be specified.

Chapter 9

Conclusion

The energy spectra of high intense x-ray beams obtained by implementing the algorithm based on an iterative perturbation method were found to contain unrealistic spectral features, i.e. peaks and valleys. As described in Chapter 4, the energy spectrum of a megavolt x-ray beam should be continuous, smooth, and contain only a single peak but no valleys. A method of smoothing the x-ray energy spectra by means of polynomials of lowest possible degrees, to eliminate non physical features in the spectra, was developed.

The x-ray beam produced by an electron linac has extremely high flux which makes a direct measurement of the energy spectrum impossible. Any detector that is placed in a primary x-ray beam is saturated due to signal pile-up and saturation-induced dead times. It is not possible to reduce the photon flux in the therapeutic x-ray beams to a level that can be measured by a detector by direct means such as reducing the beam current without changing the spectral distribution, and the distances available in a treatment room, to make use of the inverse square law, are limited.

The theoretical calculation of the spectrum using Monte Carlo simulation involves a direct transport of electrons into an electron target to generate x-rays and then transports the generated x-rays through various filters to determine x-ray energy spectra. For this purpose, a detailed information about the geometry of the x-ray

machine is required. But it is often impossible to get the required information about the internal geometry of all the clinical x-ray machines. Even if the required information for one machine is obtained, it is often very time consuming and difficult to reproduce the calculation involved in Monte Carlo simulation to other machines as each x-ray machine has a unique geometry.

The determination of x-ray energy spectra using dose-depth datasets, measured by absorbers of suitable composition under the conditions of narrow beam attenuation, is probably the best approach as it does not require detailed information regarding the internal structure or geometry of the x-ray machine. The measurement of dose-depth dataset required in the calculation can be carried out in relatively simple way and to a high degree of accuracy. Developing a method of measuring dose-depth datasets routinely in an x-ray machine and applying the iterative perturbation method via a computer program will allow the x-ray energy spectrum to be determined on a routine basis.

The problem of estimating an x-ray energy spectrum using the dose-depth datasets has always been considered as an ill-posed problem since the system of equations that relates the dose-depth dataset to the x-ray spectrum is under-determined. Various indirect approaches of solving such ill-posed problems, such as the inverse Laplace transform, matrix inversion, and iterative perturbation methods were studied. Among these methods, the iterative perturbation method proposed by Waggner [37] was found to be the most successful when applied to both diagnostic and therapeutic x-ray beams. However, the iterative perturbation method yields x-ray energy spectra with non physical features.

To eliminate nonphysical features in the spectra, a number of smoothing algorithms including the moving average method, spline smoothing, loess local regression, mixed-estimation method, and double sampling for regression were considered.

But none of them was found to smooth a spectrum globally and produce a smooth spectrum having expected features of the spectral shape.

A method of smoothing the x-ray energy spectrum, calculated by using iterative perturbation method, was developed in this project. This approach uses a polynomial of lowest possible degree to fit the calculated bremsstrahlung x-ray spectra containing non physical features and yields an energy spectrum containing only one peak but no valleys. Fitting a polynomial to an energy spectrum estimated by considering a certain number of discrete energy bins gives a single function that represents the energy spectrum of infinite energy resolution. An x-ray energy spectrum obtained from a polynomial fit was found to yield a calculated dose-depth dataset that possesses the same level of positive agreement with the measured dose-depth dataset as that found for the unsmoothed spectrum obtained by the iterative perturbation method.

The method of smoothing a nonphysical x-ray spectrum using a polynomial fit does not guarantee the uniqueness of the spectrum. However, it produces a fairly stable x-ray spectrum which makes the spectrum to be better than the ones obtained from all other existing methods. This method can be used as a research tool to further investigate the spectral properties of x-ray beams used in diagnostic and radiotherapeutic medicine. The spectrum to be smoothed need not be generated by the algorithm based on an iterative perturbation method. Spectra obtained from other techniques including the inverse Laplace transform method [24–27, 56], the direct matrix-inversion method [34, 67], and theoretical calculation using Monte Carlo simulation [18–20, 77, 78], that contains nonphysical peaks and valleys, can be smoothed using a polynomial fit to get a physically acceptable x-ray energy spectrum.

An analysis of the spectral shape dependency on the estimated value of minimum x-ray energy in Section 8.6.1, shows that spectra calculated with different

values of the minimum x-ray energy are practically identical to one another. The relative intensity of x-rays at higher photon energy remains nearly constant and the spectral peak occurs at the same photon energy no matter what minimum photon energy is considered in the calculation. However, the amplitude of the peak energy is inversely proportional to the minimum x-ray energy considered in the calculation. It was also observed that the spectrum converges faster at the higher photon energies while a larger number of iterations is required for convergence of the spectrum at lower x-ray energies. Additional detailed analysis of the spectral properties as a function of x-ray energy would likely yield valuable results.

While measuring dose-depth datasets with aluminum or copper absorbers for therapeutic x-ray beams, the lower energy x-rays are highly attenuated by small amounts of absorber. A careful measurement of dose-depth datasets using thinner absorbers, especially at low values of total absorber thickness might be useful to investigate the spectral shape of the lower energy region.

The absorber materials used to measure dose-depth datasets were chosen according to the variation of mass attenuation coefficient as a function of x-ray energy. Absorbers composed of lower Z materials than aluminum, such as water, polyethylene, and carbon (graphite), could be used in the future to obtain dose-depth datasets for use in determining x-ray energy spectra. Multiple dose-depth datasets measured by absorbers of different compositions can be used to validate calculated x-ray energy spectra more accurately.

Ideally, all the existing methods of determining x-ray energy spectra from dose-depth datasets require the secondary x-rays that reach the detector be completely eliminated. Although secondary x-rays can be minimized to some extent, they can never be completely eliminated. In therapeutic x-ray beams, secondary x-rays are mainly the result of Compton scattering. Including the Compton scattered x-rays

in the calculation of x-ray spectra of therapeutic x-ray beams can be one aspect for additional study in the future.

Minimizing the dose deposited at the shallow depth, i.e. the healthy tissues upstream of a tumor, is one of the most crucial requirements when using x-rays for radiotherapy. The lower energy x-rays present in a beam are responsible for skin and shallow dose deposition. In general, x-ray beams with larger nominal energies are used to treat the tumors at deeper sites within a patient assuming that higher energy x-rays present in such beams have greater penetrating power. However, the spectral results obtained for 6, 10, and 18 MVp x-ray beams in this study show that the beams with higher nominal energies tend to have a significant fraction of total fluence at low energy and comparatively much smaller intensities of the higher energy x-rays. It means the use of x-ray beams with larger nominal energies may not be as effective as we thought although these beams have greater penetrating power. A further study is required to investigate whether the use of x-ray beams with larger nominal energies (such as 18 MVp) are effective.

Given the information we have regarding an x-ray beam produced by a clinical x-ray machine, i.e. the minimum x-ray energy, the maximum x-ray energy, and dose-depth datasets measured in the beam, it is unlikely that we could theoretically obtain spectra with greater confidence. None of the existing methods of determining x-ray spectra have yielded a unique solution for an x-ray energy spectrum. It is also possible that the unique energy spectrum of an x-ray beam may not exist in reality. The smoothing technique developed in this project was found to obtain more physical and better x-ray energy spectra than those obtained from other existing methods.

REFERENCES

- [1] R. B. Leighton, *Principles of modern physics*. McGraw-Hill New York, 1959, vol. 795.
- [2] H. E. Johns, *Physics of radiology*. Charles River Media, 1983.
- [3] J. T. Bushberg and J. M. Boone, *The essential physics of medical imaging*. Lippincott Williams & Wilkins, 2011.
- [4] F. M. Khan and J. P. Gibbons, *Khan's the physics of radiation therapy*. Lippincott Williams & Wilkins, 2014.
- [5] L. Baird, "X-ray spectra vs attenuation data: A theoretical analysis," *Medical physics*, vol. 8, no. 3, pp. 319–323, 1981.
- [6] E. D. Trout, J. Kelley, and A. Lucas, "Determination of half-value layer." *The American journal of roentgenology, radium therapy, and nuclear medicine*, vol. 84, pp. 729–740, 1960.
- [7] E. Trout, J. Kelley, and A. Lucas, "The second half-value layer and the homogeneity coefficient." *The American journal of roentgenology, radium therapy, and nuclear medicine*, vol. 87, p. 574, 1962.
- [8] T. R. Fewell and R. E. Shuping, *Handbook of mammographic x-ray spectra*. Department of Health, Education, and Welfare, Public Health Service, Food and Drug Administration, Bureau of Radiological Health, Division of Electronic Products, 1978.

- [9] C. S. Chen, C. Vyborny, H.-P. Chan, G. Holje *et al.*, “Monte carlo simulation studies of detectors used in the measurement of diagnostic x-ray spectra,” *Medical physics*, vol. 7, no. 6, pp. 627–635, 1980.
- [10] A. D. Maidment, R. Fahrig, and M. J. Yaffe, “Dynamic range requirements in digital mammography,” *Medical physics*, vol. 20, no. 6, pp. 1621–1633, 1993.
- [11] I. A. Elbakri and J. A. Fessler, “Statistical image reconstruction for polyenergetic x-ray computed tomography,” *IEEE transactions on medical imaging*, vol. 21, no. 2, pp. 89–99, 2002.
- [12] L. Zhang, G. Zhang, Z. Chen, and Y. Xing, “An approximate reconstruction method for dual energy computed tomography,” in *Proceedings of the 9th International Meeting on Fully Three Dimensional Image Reconstruction in Radiology and Nuclear Medicine*, 2007, pp. 317–320.
- [13] K. Jessen, “Measurements of primary spectra from a kilocurie 60co unit and a 6 mev linear accelerator,” *Acta radiologica: therapy, physics, biology*, vol. 12, no. 6, pp. 561–568, 1973.
- [14] L. B. Levy, R. G. Waggener, W. D. McDavid, and W. H. Payne, “Experimental and calculated bremsstrahlung spectra from a 25-mev linear accelerator and a 19-mev betatron,” *Medical physics*, vol. 1, no. 2, pp. 62–67, 1974.
- [15] W. T. Jalbout and N. M. Spyrou, “Spectral reconstruction by scatter analysis for a linear accelerator photon beam,” *Physics in Medicine & Biology*, vol. 51, no. 9, p. 2211, 2006.
- [16] R. Mohan, C. Chui, and L. Lidofsky, “Energy and angular distributions of photons from medical linear accelerators,” *Medical physics*, vol. 12, no. 5, pp. 592–597, 1985.

- [17] M. Bhat, J. Pattison, G. Bibbo, and M. Caon, “Off-axis x-ray spectra: A comparison of monte carlo simulated and computed x-ray spectra with measured spectra,” *Medical physics*, vol. 26, no. 2, pp. 303–309, 1999.
- [18] M. Ay, M. Shahriari, S. Sarkar, M. Adib, and H. Zaidi, “Monte carlo simulation of x-ray spectra in diagnostic radiology and mammography using mcnp4c,” *Physics in Medicine & Biology*, vol. 49, no. 21, p. 4897, 2004.
- [19] F. Verhaegen, A. Nahum, S. Van De Putte, and Y. Namito, “Monte carlo modelling of radiotherapy kv x-ray units,” *Physics in Medicine & Biology*, vol. 44, no. 7, p. 1767, 1999.
- [20] J. Mercier, D. Kopp, W. McDavid, S. Dove, J. Lancaster, and D. Tucker, “Modification and benchmarking of mcnp for low-energy tungsten spectra,” *Medical physics*, vol. 27, no. 12, pp. 2680–2687, 2000.
- [21] K. Ng, C. Kwok, and F. Tang, “Monte carlo simulation of x-ray spectra in mammography,” *Physics in Medicine & Biology*, vol. 45, no. 5, p. 1309, 2000.
- [22] L. Silberstein, “Determination of the spectral composition of x-ray radiation from filtration data,” *JOSA*, vol. 22, no. 5, pp. 265–280, 1932.
- [23] ———, “Xxxiv. spectral composition of an x-ray radiation determined from its filtration curve,” *The London, Edinburgh, and Dublin Philosophical Magazine and Journal of Science*, vol. 15, no. 98, pp. 375–394, 1933.
- [24] B. R. Archer and L. K. Wagner, “A laplace transform pair model for spectral reconstruction,” *Medical physics*, vol. 9, no. 6, pp. 844–847, 1982.
- [25] B. R. Archer, “Laplace transform pair model to determine bremsstrahlung spectra from attenuation data,” Texas Univ., Houston (USA). School of Public Health, Tech. Rep., 1984.

- [26] B. R. Archer, L. K. Wagner, D. A. Johnston, P. Almond, and S. Bushong, "Analysis of errors in spectral reconstruction with a laplace transform pair model," *Physics in Medicine & Biology*, vol. 30, no. 5, p. 411, 1985.
- [27] B. R. Archer and L. K. Wagner, "Determination of diagnostic x-ray spectra with characteristic radiation using attenuation analysis," *Medical physics*, vol. 15, no. 4, pp. 637–641, 1988.
- [28] —, "A modified x-ray spectra reconstruction technique," *Physics in medicine and biology*, vol. 33, no. 12, p. 1399, 1988.
- [29] G. Bell, "Spectral distribution in the continuous x-ray spectrum and the specification of x-ray quality," *The British Journal of Radiology*, vol. 9, no. 106, pp. 680–688, 1936.
- [30] D. Jones, "The determination from absorption data of the distribution of x-ray intensity in the continuous x-ray spectrum," *The British Journal of Radiology*, vol. 13, no. 147, pp. 95–101, 1940.
- [31] J. Greening, "The determination of x-ray energy distributions by the absorption method," *The British journal of radiology*, vol. 20, no. 230, pp. 71–78, 1947.
- [32] W. Saylor, "The x-ray spectrum from a 2 mvp alternating potential generator," *Physics in medicine and biology*, vol. 14, no. 1, p. 87, 1969.
- [33] P.-H. Huang, T.-S. Chen, and K. R. Kase, "Reconstruction of diagnostic x-ray spectra by numerical analysis of transmission data," *Medical physics*, vol. 13, no. 5, pp. 707–710, 1986.
- [34] P. Francois, A. Catala, and C. Scouarnec, "Simulation of x-ray spectral reconstruction from transmission data by direct resolution of the numeric system af=t," *Medical physics*, vol. 20, no. 6, pp. 1695–1703, 1993.

- [35] P. Francois, F. Coste, J. Bonnet, and O. Caselles, "Validation of reconstructed bremsstrahlung spectra between 6 mv and 25 mv from measured transmission data," *Medical physics*, vol. 24, no. 5, pp. 769–773, 1997.
- [36] A. Catala, P. Francois, J. Bonnet, and C. Scouarnec, "Reconstruction of 12 mv bremsstrahlung spectra from measured transmission data by direct resolution of the numeric system $af = t$," *Medical physics*, vol. 22, no. 1, pp. 3–10, 1995.
- [37] R. G. Waggener, M. M. Blough, J. A. Terry, D. Chen, N. E. Lee, S. Zhang, and W. D. McDavid, "X-ray spectra estimation using attenuation measurements from 25 kvp to 18 mv," *Medical physics*, vol. 26, no. 7, pp. 1269–1278, 1999.
- [38] E. Y. Sidky, L. Yu, X. Pan, Y. Zou, and M. Vannier, "A robust method of x-ray source spectrum estimation from transmission measurements: Demonstrated on computer simulated, scatter-free transmission data," *Journal of applied physics*, vol. 97, no. 12, p. 124701, 2005.
- [39] L. Zhang, G. Zhang, Z. Chen, Y. Xing, J. Cheng, and Y. Xiao, "X-ray spectrum estimation from transmission measurements using the expectation maximization method," in *Nuclear Science Symposium Conference Record, 2007. NSS'07. IEEE*, vol. 4. IEEE, 2007, pp. 3089–3093.
- [40] P.-H. Huang, T.-S. Chen, and K. R. Kase, "Reconstruction of diagnostic x-ray spectra by numerical analysis of transmission data," *Medical physics*, vol. 13, no. 5, pp. 707–710, 1986.
- [41] J. Boone, "X-ray spectral reconstruction from attenuation data using neural networks," *Medical physics*, vol. 17, no. 4, pp. 647–654, 1990.
- [42] B. Soole, "A method of x-ray attenuation analysis for approximating the intensity distribution at its point of origin of bremsstrahlung excited in a thick target by

- incident electrons of constant medium energy,” *Physics in Medicine & Biology*, vol. 21, no. 3, p. 369, 1976.
- [43] R. D. Evans and A. Noyau, “The atomic nucleus,” 1955.
- [44] M. J. Berger, J. Hubbell, S. Seltzer, J. Chang, J. Coursey, R. Sukumar, D. Zucker, and K. Olsen, “Xcom: Photon cross sections database,” *NIST Standard reference database*, vol. 8, no. 1, pp. 3587–3597, 1998.
- [45] F. H. Attix, *Introduction to radiological physics and radiation dosimetry*. John Wiley & Sons, 2008.
- [46] W. R. Hendee and E. R. Ritenour, *Medical imaging physics*. John Wiley & Sons, 2003.
- [47] M. Berger and S. Seltzer, “Xcom photon cross sections,” *Version 3.1, NISTIR*, 1999.
- [48] H. Kulenkampff, “Untersuchungen der kontinuierlichen röntgenstrahlung dünner aluminiumfolien,” *Annalen der Physik*, vol. 392, no. 21, pp. 597–637, 1928.
- [49] M. Aydinol, R. Hippler, I. McGregor, and H. Kleinpoppen, “Angular distribution of x-radiation following electron bombardment of free atoms,” *Journal of Physics B: Atomic and Molecular Physics*, vol. 13, no. 5, p. 989, 1980.
- [50] I. Kawrakow and D. Rogers, “The egsnrc code system: Monte carlo simulation of electron and photon transport,” 2000.
- [51] J. F. Briesmeister *et al.*, *MCNP—A general Monte Carlo code for neutron and photon transport*. Los Alamos National Laboratory Los Alamos, 1986.
- [52] S. Agostinelli, J. Allison, K. a. Amako, J. Apostolakis, H. Araujo, P. Arce, M. Asai, D. Axen, S. Banerjee, G. . Barrand *et al.*, “Geant4a simulation toolkit,” *Nuclear*

- instruments and methods in physics research section A: Accelerators, Spectrometers, Detectors and Associated Equipment*, vol. 506, no. 3, pp. 250–303, 2003.
- [53] J. Halbleib and T. Mehlhorn, “Its: The integrated tiger series of coupled electron/photon monte carlo transport codes,” Sandia National Labs., Albuquerque, NM (USA), Tech. Rep., 1984.
 - [54] D. Sheikh-Bagheri and D. Rogers, “Sensitivity of megavoltage photon beam monte carlo simulations to electron beam and other parameters,” *Medical physics*, vol. 29, no. 3, pp. 379–390, 2002.
 - [55] P.-H. Huang, K. R. Kase, and B. E. Bjärngard, “Spectral characterization of 4 mv bremsstrahlung by attenuation analysis,” *Medical physics*, vol. 8, no. 3, pp. 368–374, 1981.
 - [56] B. R. Archer, P. R. Almond, and L. K. Wagner, “Application of a laplace transform pair model for high-energy x-ray spectral reconstruction,” *Medical physics*, vol. 12, no. 5, pp. 630–633, 1985.
 - [57] M. Rubio and R. Mainardi, “Determination of x-ray spectra including characteristic line intensities from attenuation data,” *Physics in Medicine and Biology*, vol. 29, no. 11, p. 1371, 1984.
 - [58] S. Tominaga, “A singular-value decomposition approach to x-ray spectral estimation from attenuation data,” *Nuclear Instruments and Methods in Physics Research Section A: Accelerators, Spectrometers, Detectors and Associated Equipment*, vol. 243, no. 2, pp. 530–538, 1986.
 - [59] J. Twidell, “The determination of x-ray spectra using attenuation measurements and a computer program,” *Physics in medicine and biology*, vol. 15, no. 3, p. 529, 1970.

- [60] P.-H. Huang, K. R. Kase, and B. E. Bjärngard, "Reconstruction of 4-mv bremsstrahlung spectra from measured transmission data," *Medical physics*, vol. 10, no. 6, pp. 778–785, 1983.
- [61] A. Ahnesjo and P. Andreo, "Determination of effective bremsstrahlung spectra and electron contamination for photon dose calculations," *Physics in medicine and biology*, vol. 34, no. 10, p. 1451, 1989.
- [62] A. Nisbet, H. Weatherburn, J. Fenwick, and G. McVey, "Spectral reconstruction of clinical megavoltage photon beams and the implications of spectral determination on the dosimetry of such beams," *Physics in medicine and biology*, vol. 43, no. 6, p. 1507, 1998.
- [63] A. Iwasaki, H. Matsutani, M. Kubota, A. Fujimori, K. Suzaki, and Y. Abe, "A practical method for estimating high-energy x-ray spectra using the iterative perturbation principle proposed by waggener," *Radiation Physics and chemistry*, vol. 67, no. 2, pp. 81–91, 2003.
- [64] T. Shimosato, K. Tabushi, S. Kitoh, Y. Shiota, C. Hirayama, and S. Suzuki, "Calculation of 10 mv x-ray spectra emitted by a medical linear accelerator using the bfgs quasi-newton method," *Physics in medicine and biology*, vol. 52, no. 2, p. 515, 2006.
- [65] M. Manciu, F. S. Manciu, T. Vulcan, E. Nes, and R. G. Waggener, "Robust megavoltage x-ray spectra estimation from transmission measurements," *Journal of X-ray Science and Technology*, vol. 17, no. 1, pp. 85–99, 2009.
- [66] M. Krmar, J. Slivka, I. Bikit, M. Vesković, and L. Čonkić, "Evaluation of bremsstrahlung spectra generated by a 4-mev linear accelerator," *Medical physics*, vol. 23, no. 5, pp. 651–654, 1996.

- [67] M. Stampanoni, M. Fix, P. Francois, and P. Rüeggsegger, “Computer algebra for x-ray spectral reconstruction between 6 and 25 mv,” *Medical physics*, vol. 28, no. 3, pp. 325–327, 2001.
- [68] M. Ay, S. Sarkar, M. Shahriari, D. Sardari, and H. Zaidi, “Assessment of different computational models for generation of x-ray spectra in diagnostic radiology and mammography,” *Medical physics*, vol. 32, no. 6Part1, pp. 1660–1675, 2005.
- [69] A. Iwasaki, S. Kimura, K. Sutoh, K. Kamimura, M. Sasamori, M. Seino, F. Ko-
mai, S. Terashima, M. Kubota, Y. Narita *et al.*, “Reconsideration of the iwasaki–
waggener iterative perturbation method for reconstructing high-energy x-ray spec-
tra,” *Radiological physics and technology*, vol. 5, no. 2, pp. 248–269, 2012.
- [70] A. Iwasaki, M. Kubota, A. Fujimori, K. Suzaki, Y. Abe, H. Ono, K. Nishimura,
and H. Yokoyama, “Formulation of spectra-based attenuation coefficients in water
as a function of depth and off-axis distance for 4, 10 and 15 mv x-ray beams,”
Radiation Physics and Chemistry, vol. 72, no. 6, pp. 657–661, 2005.
- [71] E. Y. Sidky, L. Yu, and X. Pan, “Application of expectation maximization to x-ray
spectrum estimation for medical accelerators from transmission data,” in *Medical
Imaging 2004: Physics of Medical Imaging*, vol. 5368. International Society for
Optics and Photonics, 2004, pp. 856–861.
- [72] E. Podgorsak, J. Rawlinson, and H. Johns, “X-ray depth doses from linear acceler-
ators in the energy range from 10 to 32 mev,” *American Journal of Roentgenology*,
vol. 123, no. 1, pp. 182–191, 1975.
- [73] E. Podgorsak, J. Rawlinson, M. Glavinovic, and H. Johns, “Design of x-ray tar-
gets for high energy linear accelerators in radiotherapy,” *American Journal of
Roentgenology*, vol. 121, no. 4, pp. 873–882, 1974.

- [74] D. Greene and P. C. Williams, *Linear accelerators for radiation therapy*. CRC Press, 1997.
- [75] C. Karzmark and R. J. Morton, *A Primer on Theory and Operation of Linear Accelerators in Radiation Therapy: CJ Karzmark & Robert J. Morton*. Medical Physics, 1998.
- [76] E. Ali and D. Rogers, “An improved physics-based approach for unfolding megavoltage bremsstrahlung spectra using transmission analysis,” *Medical physics*, vol. 39, no. 3, pp. 1663–1675, 2012.
- [77] K. E. Sixel and B. A. Faddegon, “Calculation of x-ray spectra for radiosurgical beams,” *Medical physics*, vol. 22, no. 10, pp. 1657–1661, 1995.
- [78] D. A. Bonifácio, H. M. Murata, M. Morales *et al.*, “Monte carlo simulation of x-ray spectra in diagnostic radiology and mammography using geant4,” in *2005 International Nuclear Atlantic Conference-INAC*. Citeseer, 2005.

VITA

Rajesh Panthi

Candidate for the Degree of

Doctor of Philosophy

Thesis: DETERMINATION OF THE ENERGY SPECTRA OF CLINICAL X-RAY
BEAMS USING DOSE-DEPTH DATASETS

Major Field: Physics

Biographical:

Education:

Completed the requirements for the Doctor of Philosophy in Physics at
Oklahoma State University, Stillwater, Oklahoma in May, 2018.

Completed the requirements for the Master of Science in Medical Physics
at Oklahoma State University, Stillwater, Oklahoma in December, 2017.

Completed the requirements for the Master of Science in Physics at Trib-
huvan University, Kathmandu, Nepal in July 2009.

Completed the requirements for the Bachelor of Science in Physics, Math-
ematics, and Statistics at Tri-Chandra Campus, Kathmandu, Nepal in
November 2004.

Experience:

Teaching and Research Assistant 08/2011-05/2018
Oklahoma State University
Stillwater, OK

Lecturer of Physics 08/2009-06/2011
St. Xavier's College
Kathmandu, Nepal

Publications:

Polf JC, **Panthi R**, Mackin DS, McCleskey M, Saastamoinen A, Roeder
BT, Beddar S. Measurement of characteristic prompt gamma rays emitted
from oxygen and carbon in tissue-equivalent samples during proton beam
irradiation. Physics in Medicine & Biology. 2013 Aug 6;58(17):5821.

Professional Memberships:

American Association of Physicists in Medicine (AAPM)
American Physical Society (APS)